Seismic Collapse Resilience of Buildings with Steel Moment Resisting Frames

by

Tung-Yu Wu

A dissertation submitted in partial fulfillment
of the requirements for the degree of
Doctor of Philosophy
(Civil Engineering)
in the University of Michigan
2019

Doctoral Committee:

Professor Sherif El-Tawil, Co-Chair
Associate Professor Jason P. McCormick, Co-Chair
Professor John Shaw
Assistant Professor Seymour M.J. Spence

Tung-Yu Wu

tungyuwu@umich.edu

ORCID iD: 0000-0002-2981-1910

© Tung-Yu Wu 2019

DEDICATION

To my parents and my wife

ACKNOWLEDGMENTS

Numerous people have helped me to complete the doctoral research presented in this dissertation. First, I would like to express my sincere gratitude to my advisors, Prof. Sherif El-Tawil and Prof. Jason McCormick, for their continuous guidance and support of my PhD study over the past few years. I would not have become a researcher and educator without their inspirational instruction and unwearied patience. I would like to especially thank Prof. El-Tawil for his research enthusiasm that inspires me to strive for excellence in every professional aspect. I would also like to thank my other committee members, Prof. Shaw and Prof. Spence, for their valuable and insightful advice to make this work more complete and accurate.

My sincere thanks also go to the members in Prof. El-Tawil's research group (Andrew, Julie, Omar, Szu-Yun, and Yunsu) and friends I have made in CEE (Arthriya, Bo, Christian, Jason, Malcolm, Ning, and Wei-Chu) for sharing their knowledge and life experiences. I would also like to thank many friends that I have made in Ann Arbor (A-Pao & Ting, Angel & Scott, Erin & Ben, Matt & Christy, Mia, Oscar, PJ, Su-Yang, TuG, Winn & Joy, and people in Teatime and Mahjong groups) for providing stress relief through making music, traveling, exercising, and all other non-academic activities. It is my fortune to have them with whom I can share my laughs and tears.

Finally, I would like to thank my wife, Yun-Chu, for her constant love and support since we met at NTU. I would not have been able to finish my PhD without her. I am extremely grateful.

TABLE OF CONTENTS

LIST OF TABLES

LIST OF FIGURES

ABSTRACT

The use of deep steel columns, with a depth of 24 inches or greater, has been prevalent in special moment frames (SMFs) built since the late 1990s. The large depth, high in-plane flexural stiffness and strength make such sections an attractive choice for engineers seeking to satisfy current panel zone, drift and strong-column/weak-beam seismic design criteria. However, deep columns have potential vulnerabilities to local and global structural instabilities that are not yet fully understood. This dissertation presents an experimental and computational investigation designed to seek insight into the behavior of deep steel columns, buildings using them, and the seismic resilience of communities that contain such buildings.

Nineteen half-scale T-section steel specimens, carefully proportioned and loaded to emulate the demands placed on deep columns under cyclic loading, are experimentally tested to investigate the effect of element slenderness ratios on cyclic flange local buckling and post-buckling response. The results show that column flanges that satisfy current highly ductile limits can suffer from significant strength degradation. A parallel computational study is used to expand the parameter space and further investigate the observations from the tests.

The effects of slenderness ratios and initial axial load on the collapse capacity of first-story deep columns are studied using detailed computational models. The loading protocols and boundary conditions are selected to represent the demands associated with seismic-induced building collapse. Design-oriented expressions integrating all key variables are proposed to compute the compressive

capacity of deep columns that meet the highly ductile criteria provided in the AISC seismic provisions.

At the system level, two prototype frames and their variants are used to study the effect of deep columns on the collapse behavior of special moment frames. Collapse fragility curves of each frame are computed using incremental dynamic analysis. The curves suggest the need to brace beam-column connections at both beam flanges, regardless of the column-beam moment ratio. The simulations also show that slenderness ratios can be influential on system level response, and the level of column axial load should be limited to prevent an undesired collapse mechanism.

The effect of design code evolution on the risks associated with using SMFs is investigated. Three code eras spanning the past half century are considered. High-fidelity models capable of explicitly capturing instabilities and fracture are employed to determine the effect of the differences in the designs. Retrofit strategies are proposed to improve the seismic resilience of communities with steel buildings. Overall, the findings provide the previously missing components to understanding of the influence of deep columns on the performance of buildings during an earthquake through experimental testing and detailed modeling at a full range of scales.

CHAPTER 1

INTRODUCTION

1.1 General Introduction, Scope, and Motivation

Seismic design requirements have evolved as researchers and engineers have sought to improve the structural resilience of buildings in an earthquake. Prior to the 1994 Northridge earthquake, steel moment resisting frames were considered to be among the most reliable and resilient structural systems for use in high seismic zones. However, both the 1994 Northridge and 1995 Kobe earthquakes shocked the faith of the structural engineering community in this type of construction as well as in the then-existing provisions governing the design of these systems. Steel moment frames suffered unexpected, wide spread brittle fractures at the welded beam-to-column moment connections. The fractures not only occurred in older construction, but also in frames built according to the most modern specifications at the time.

The unexpected damage raised concerns among the structural engineering community. It led to the launch of the SAC Steel Project, which was aimed at investigating the reasons for the observed damage. SAC was a joint venture between the Structural Engineering Association of California (SEAOC), the Applied Technology Council (ATC) and the Consortium of Universities for Research in Earthquake Engineering (CUREE). The SAC Steel Project identified several major reasons for the damage that occurred. Among the most prominent reasons were connection geometry, over-strength in the base material, and low toughness of the welding material.

To address the issues that were identified and ensure highly resilient frame design, the SAC Project recommended new and more stringent seismic design requirements, including stricter drift, strong-column/weak-beam and panel zone design criteria. These challenging requirements discouraged structural engineers from using shallow, stocky wide flange columns, such as W14 sections, which were commonly used pre-Northridge. Instead, the new criteria promoted the use of deep, wide flange steel columns with a depth of 24 inches or more. Deep columns have a substantially larger in-plane flexural stiffness and strength than W14 sections of the same weight and are therefore better able to meet the new requirements.

The use of deep columns raised new concerns due to their inherent vulnerability, particularly to lateral torsional buckling. While these concerns were initially shown to be generally unfounded (Zhang and Ricles 2006; Chi and Uang 2002; Shen et al. 2002), the effect of axial loads on column behavior was not fully considered. This shortcoming led to a number of studies on the behavior of deep columns under combined axial and lateral loading through experimental testing or simulations of individual columns or moment frames (Reyes-Salazar et al. 2014; Fogarty and El-Tawil 2015; Elkady and Lignos 2015a; Ozkula et al. 2017). While these studies provided deeper insight into deep columns, they did neither fully reflect the seismic conditions of columns in a moment frame nor consider the full range of structural instabilities in deep columns. As a result, the inelastic behavior of deep columns and how that behavior affects collapse capacity of special steel moment frames are still not fully understood.

The engineering practice of using deep steel columns is a reflection of many evolutionary changes in seismic design over the past century. In addition to the 1994 Northridge earthquake, the 1971 San Fernando, 1979 Imperial Valley, 1985 Mexico City, and 1987 Whittier Narrows earthquakes all resulted in substantial changes to the then-existing seismic design codes. Among the major

changes in design provisions prompted by these earthquakes are new site condition considerations, spectral shape modification for design purposes, changes in axial strength of steel columns, and the specification of ductile detailing for steel moment frames (SEAOC Seismology Committee 2006). With the constraints imposed by design codes, engineering practice also evolved accordingly to minimize construction costs and optimize architectural design. These changes led to the use of high strength materials, perimeter moment frames, and the widespread use of deep columns.

With the above changes, which were considered improvements at the time they were implemented, it was natural to expect that newer steel buildings would have better seismic performance and lower collapse risk than older ones. Nevertheless, the effect of these changes on seismic risk associated with steel moment frames has not yet been thoroughly examined and quantified. Another important point is that buildings in a large city or community were built at different times to different codes and therefore large communities face a seismic risk that is a function of their building inventory. Analysis of this risk is therefore needed so that planners can better assess the risk posed to existing communities and better prepare them to face future seismic events.

1.2 Objectives

The overall objective of this research is to investigate the collapse resistance of steel moment frames, specifically those with deep columns. A key aim is to propose design guidelines that can reduce the collapse risk of steel moment frames with deep columns. These objectives are achieved through a comprehensive experimental and computational research program. The computational models used are of high fidelity and can explicitly model structural instabilities, fracture and the entire collapse process. Specific objectives are as follows:

(1) Use experiments to understand how element slenderness ratios affect axial strength degradation of flanges in beams and columns under reversed cyclic loading. Synthesize the information to evaluate the adequacy of element slenderness limits in current AISC seismic provisions (AISC 2016b).

(2) Using high fidelity computational models, identify and assess the effect of key variables on the collapse capacity of first-story deep steel columns in special moment frames subjected to seismic demands. Use the insight gained to propose new highly ductile limits for deep columns if the current AISC limits are not adequate.

(3) Using detailed computational models, investigate the seismic collapse behavior of steel special moment frames with deep columns and identify collapse modes. Recommend new provisions to improve the collapse capacity of the frames based on the findings.

(4) Study how seismic design specifications for steel frames have evolved over the past half century. Compare the computed seismic performance of a set of steel moment frames, with various heights, designed according to codes from different eras and propose strategy to improve seismic resilience of communities.

1.3 Structure of the Dissertation

A brief description of the six chapters comprising this dissertation is provided below.

Chapter 1: Introduction. General information underlying the motivation and objectives of this research is presented. The scope of this research and an introduction to the other chapters is also provided.

Chapter 2: Cyclic Flange Local Buckling in Structural Members. This chapter presents an experimental study aimed at investigating flange local buckling and post-buckling behavior under reversed cyclic loading. The axial demands on flanges in beams and columns under symmetric cyclic loading are studied. Nineteen T-section specimens, designed to represent key portions of steel beams and columns, are axially loaded to evaluate the current AISC highly ductile slenderness limits and assess their adequacy. A parametric computational study of the T-sections is performed to expand the parameter space and evaluate the effect of element slenderness ratios on column compression capacity under cyclic loading.

Chapter 3: Collapse Resistance of Deep Steel Columns in Special Moment Frames. This chapter describes a computational study of the collapse resistance of deep columns under combined axial and drift loading. Loading protocols and boundary conditions, carefully calibrated to realistically represent the seismic demands on first-story columns at large drifts, are used to assess the effect of key variables on the capacity of deep columns. The simulation results are used to propose slenderness limits that incorporate key variables identified in the research to permit deep columns to achieve highly ductile behavior.

Chapter 4: Collapse Resistance of Steel Special Moment Frames with Deep Columns. In this chapter, a computational study of the effect of deep columns on system level responses is presented. A set of steel special moment frames are employed to study the key factors that affect collapse potential of the frames. The frame models are capable of capturing the full range of instabilities and major collapse behaviors. Based on the developed collapse fragility curves, design recommendations are proposed to improve the seismic collapse resistance of special moment frames with deep columns.

***Chapter 5: Effect of Seismic Design Evolution on Resilience of Steel Moment Frames*.** This chapter reviews the evolution of seismic design provisions and practices over the past half century. A set of steel moment frames, with different heights, are designed using seismic design codes from three distinct code eras. The developed models are highly refined and can explicitly capture fracture and instabilities as part of the complete collapse behavior. Retrofit strategies are proposed to improve the seismic resilience of communities based on the resilience assessment of the frames.

***Chapter 6: Summary and Conclusions*.** This chapter summarizes the key findings and contributions that can be extracted from this research. Recommendations for future research related to the collapse resistance and resilience of steel moment frames are also included.

1.4 Journal Publication from this Dissertation

Journal articles from research presented in Chapter 2 and Chapter 5 are in preparation and will soon be submitted for publication. Chapter 3 and Chapter 4 have been published in journal papers. Details are listed below:

Wu, T.-Y, El-Tawil, S., and McCormick, J. "Effect of Cyclic Flange Local Buckling on the Capacity of Steel Members." In preparation. **(Chapter 2)**

Wu, T.-Y, El-Tawil, S., and McCormick, J. (2018). "Highly ductile limits for deep steel columns." *J. of Structural Engineering*, 10.1061/(ASCE)ST.1943-541X.0002002. **(Chapter 3)**

Wu, T.-Y, El-Tawil, S., and McCormick, J. (2018). "Seismic Collapse Response of Steel Moment Frames with Deep Columns." *J. of Structural Engineering*, 10.1061/(ASCE)ST.1943-541X.0002150. **(Chapter 4)**

Wu, T.-Y, El-Tawil, S., and McCormick, J. "Influence of Seismic Design Evolution on Resilience of Communities with Steel Buildings." In preparation. **(Chapter 5)**

CHAPTER 2

CYCLIC FLANGE LOCAL BUCKLING IN STRUCTURAL MEMBERS

2.1 General

This chapter presents an experimental study of nineteen axially loaded half-scale T-section specimens to address the paucity of information on the effect of flange local buckling (FLB) on the cyclic response of steel wide flange sections. Detailed finite element analysis is performed to develop the test configuration and axial loading protocols that can replicate the seismic demands imposed on beam flanges and column flanges in their plastic hinge region (Section 2.3-2.5). The specimens that cover a wide range of element slenderness ratios are selected to study the major influence of variables: flange slenderness ratio, level of web restraint, and loading scheme (monotonic versus cyclic) (Section 2.6). A computational study is also performed to expand the parameter space and further investigate the observations from the tests (Section 2.7). The peak strength and strength degradation rates observed from the test and simulations are used to evaluate current seismic provisions for local instability in steel structures (Section 2.8). Appendix A provides experimental results in detail.

2.2 Motivation

Local buckling can cause significant strength and stiffness degradation in steel member response during an earthquake. Maximum values for the slenderness ratios of unstiffened and stiffened elements of wide flange sections (i.e. $b/2t_f$ for flanges and h/t_w for webs, where b and h are flange

width and web height, respectively, and t_f and t_w are flange and web thicknesses, respectively) are specified in the AISC specifications (AISC 2016c). When ductility is important, e.g. in earthquake applications, the maximum slenderness ratios are specified in the AISC seismic provisions (AISC 2016b) for members classified as highly ductile or moderately ductile. The current slenderness limits are derived from early analytical and experimental research on beams under monotonic loading (Sawyer, 1961; Lay, 1965; Bansal, 1971; Kemp, 1986).

While local buckling in beam plastic hinges has been investigated in the past for monotonic loading situations, information on the effect of cyclic loading on the slenderness limits is rather rare in the literature and is typically inferred from member level response. Richards and Uang (2005) studied the effect of flange slenderness ratio on the cyclic rotation capacity of links using finite element models. Their results suggested that the existing limiting slenderness ratios for link flanges could be relaxed. Newell and Uang (2008) conducted cyclic tests of W14 columns subjected to axial forces combined with large drift loading. The stocky webs of W14 columns were found to stabilize the flange and contribute to the observed large deformation capacity of the studied sections. Cheng et al. (2013) tested nine H-shaped beam-columns with large slenderness ratios and concluded that the effect of flange/web slenderness ratios and axial force ratios should be considered mutually because of their strong dependence upon each other.

Based on the above experimental and computational member level studies, the effect of cyclic FLB on beam and column behaviors is still not well understood. To deepen the understanding, a study that directly relates the element slenderness ratios to flange post-buckling strength under cyclic loading is needed, which motivates the presented work that utilizes T-section members to study the key portions of steel structural members.

2.3 Finite Element Model Development and Validation

The finite element models employed in this dissertation are created and analyzed using the commercial software, Hypermesh (2013) and LS-DYNA (2013), respectively. The models are discretized using 4-node fully integrated shell elements (ELFORM 16) based on the formulation published by Engelmann et al. (1989) with a mesh size of 25.4 mm, which is also employed in Fogarty and El-Tawil (2015). The mesh density is kept constant in all models to avoid mesh size dependency. A combined isotropic/kinematic hardening material model (MAT_153) developed by Huang and Mahin (2010) is assigned to the shell elements. This material model has two back stress terms for kinematic hardening combined with linear isotropic hardening. The hardening moduli and model parameters are calibrated to the true stress-true strain model proposed by Arasaratnam et al. (2011) using nominal or measured material properties of the employed steel. Initial imperfections in the T-section members used herein are obtained by applying the first buckling mode as a geometric perturbation. Calibration studies showed that the results match the test data best when the maximum amplitude of the applied perturbation geometry is the plate width divided by 500.

The finite-element models used in this work were thoroughly validated by Fogarty et al. (2017) using the cyclic experimental data from deep column specimens of Ozkula et al. (2017b). The test matrix used in the validation studies included five W24 sections and three levels of axial load that resulted in a total of 25 specimens categorized into eight groups. The column specimens were 5.49 m long, tested with fixed-fixed boundary conditions, and subjected to a combination of a constant axial force and a symmetric cyclic drift loading associated with steel beam-to-column moment connection tests as outlined by AISC (2016b). The validation study showed that the finite-element models were able to reasonably capture the shape, length, and occurrence of local and global

buckling behavior. More details can be found in Fogarty et al. (2017), which, in the interest of space, are not repeated here. Additional validation studies using the experimental data obtained in this work are discussed later on in Section 2.7.

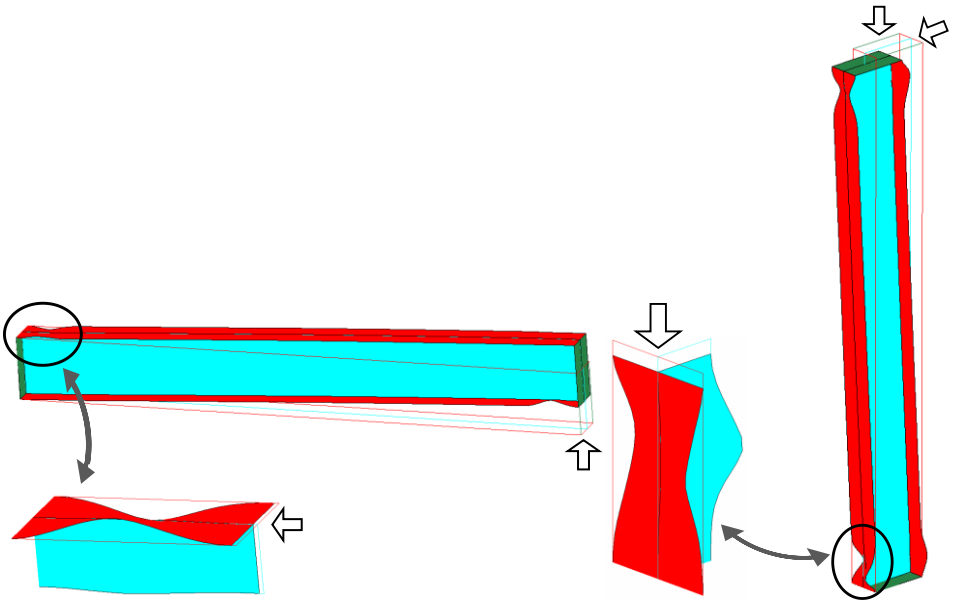

(a) (b)

Figure 2-1. Flange deformed shape in plastic hinge region of (a) wide flange beams under cyclic bending moment and (b) wide flange columns under combined cyclic axial force and bending moment

2.4 Rationale for T-Section Test Specimens

Under seismic loading, structural members of a special moment frame (SMF), such as beams and columns, are subjected to either cyclic bending moment or combined cyclic axial force and bending moment in their plastic hinge regions. The premise of this study is that the seismic demands on flanges in the plastic hinge region can be approximated as cyclic axial deformation demands for wide flange beams and columns, as shown in Figure 2-1. Therefore, rather than testing a complete structural component or subassemblage, a short T-section column with fixed ends can

be tested under cyclic axial loading instead. This assumption substantially simplifies the study of inelastic cyclic FLB because a hydraulic axial load frame can be used instead of a more comprehensive and complicated setup needed to test a structural member or sub-assembly under cyclic loading.

To ensure that the proposed T-section members realistically represent their full section counterparts, the web portion of the T must be adequately long to impose the same level of flange restraint achieved in the original section. Detailed finite element studies of W24 sections are conducted to determine a reasonable web length. The axial deformation history of the flange in the plastic hinge region, whose length is the same as the section depth as usually assumed (MacRae et al. 1990), is extracted and applied to its counterpart T-section member. The responses of the T-section member and the corresponding portion in the full member are compared in terms of overall deformed shape and the force versus deformation history. The studies suggest that a web length equal to one third of the full section depth results in a meaningful representation of the overall section's behavior.

Figure 2-2 shows comparisons between the full and T-section member responses for two different W24 sections under different levels of axial loading (P/P_y, where P_y is the axial yield strength of the cross section). Section sizes are listed in English units (in. × lb/ft) throughout this dissertation because this naming scheme is widely recognized. Here, the effective stress ratio (ESR) is defined as the axial strength normalized by the yield strength of the cross-section, i.e., and the normalized axial deformation (NAD) is calculated by Δ/L, where Δ is the relative axial displacement between member's ends and L is the original length of the members. The ESR is used as the performance parameter and represents the retained axial strength of the T-section member after experiencing a given axial deformation history, while the NAD is used to describe the overall status of the

members. In Figure 2-2, the full members are adapted from Fogarty et al. (2017) and are subjected to the symmetric cyclic drift loading used to qualify beam-to-column moment connections in the AISC seismic provisions (2016b). It is clear that the overall buckled shape and force deformation history match reasonably well. These results are quite typical and are observed for other W24 sections subjected to different levels of axial load and other types of loading histories including monotonic and the ratcheting history associated with collapse, as discussed in Wu et al. (2018a).

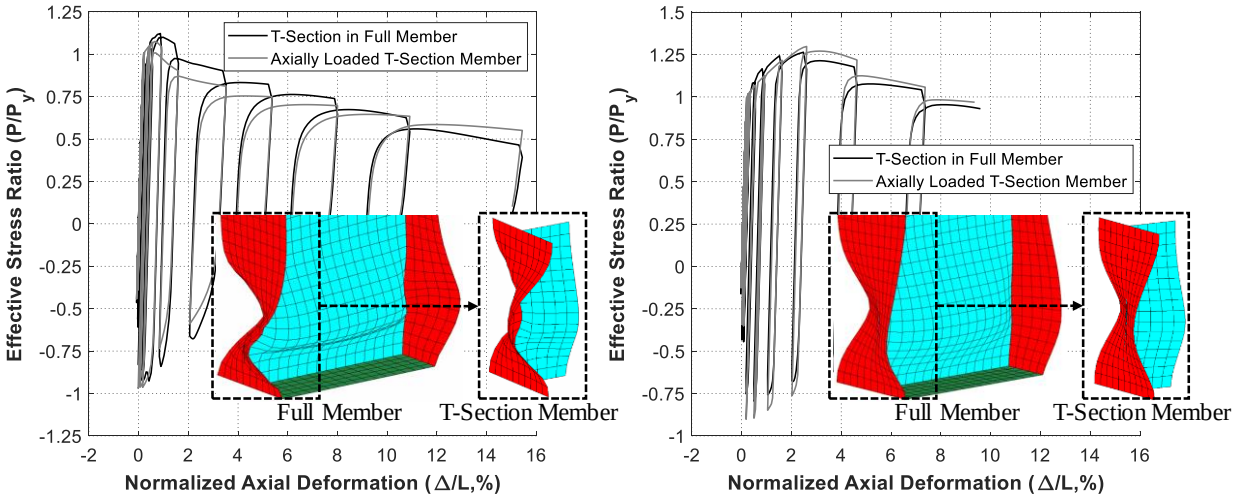

(a) W24×104, P/P_y = 0.2 (b) W24×176, P/P_y = 0.4

Figure 2-2. Comparison between full member and T-section member responses under symmetric drift loading with different axial load levels

2.5 Testing Program

2.5.1. Test Specimens and Setup

Nineteen half-scale T-section specimens with a depth of 305 mm were selected to represent the behavior of a W24 section, which is commonly used for beams and columns in the current design of special moment frames. The experimental parameters are flange and equivalent web slenderness ratios, i.e. $b/2t_f$ and $(h/t_w)_{eq}$. The parameter $(h/t_w)_{eq}$ is the web slenderness ratio of the full W24

section, where the depth is three times that of the T-section member. Changing $(h/t_w)_{eq}$ changes the amount of web restraint applied to the flanges. To achieve control over the slenderness ratios, built-up sections were preferred over cutting T-sections from an existing W-sections. The effect of residual stress due to the welding between the web and flange is considered insignificant as the specimens undergo large plastic deformations. To confirm that the test results from built-up T-section specimens are transferable to WT-section members, a WT-section specimen cut from a W-section member with similar slenderness ratios to one of the built-up T-section specimens is also studied.

Five flange thicknesses and three web thicknesses are selected to cover a range of element slenderness ratios. The employed built-up T-section specimens are listed in Table 2-1, where F1 and W1 represent the thickest flange and web used in the test, respectively, and F5 and W3 represent the thinnest ones. The element slenderness ratios of the specimens are shown in Figure 2-3 along with the code-specified limiting ratios for highly ductile (λ_{hd}), moderately ductile (λ_{md}), and non-slender (λ_r) elements, as listed in Table 2-2. According to AISC (2016b, 2016c), highly/moderately ductile members are "intended to withstand significant plastic rotation of 0.04/0.02 rad or more" during the design earthquake, and non-slender sections are "cross sections possessing plate components where local buckling in the elastic range will not occur". Note that only non-slender limits for built-up sections consider the effect of web slenderness ratio on flange capacity by using the k_c factor, where k_c is the buckling coefficient for unstiffened elements and is calculated as $4/\sqrt{h/t_w}$.

Table 2-1. Test matrix

Specimen ID	b (mm)	$d/3$ (mm)	t_f (mm)	t_w (mm)	$b/2t_f$	$(h/t_w)_{eq}$	Material (Batch)	Loading Protocol	Buckled Shape	ESR at 4% Beam Drift	ESR at 4% Column Drift
W12×26-CB	164.8	101.6	9.7	5.8	8.54	47.2	A992 (1)	CB	Asym.	0.71	N/A[a]
F1W1-M	152.4	101.6	19.1	9.5	4.0	28.0	A572 (1)	M	Sym.	1.16	1.04
F2W1-M	152.4	101.6	12.7	9.5	6.0	29.3	A572 (1)	M	Asym.	1.18	0.86
F2W1-CB	152.4	101.6	12.7	9.5	6.0	29.3	A572 (1)	CB	Asym.	0.85	N/A[a]
F2W1-CC	152.4	101.6	12.7	9.5	6.0	29.3	A572 (1)	CC	Sym.	N/A[a]	0.78
F4W1-M	152.4	101.6	7.9	9.5	9.6	30.3	A572 (1)	M	Asym.	0.79	0.62
F5W1-M	152.4	101.6	4.8	9.5	16.0	31.0	A572 (1)	M	Asym.	0.73	0.53
F5W1-CB	152.4	101.6	4.8	9.5	16.0	31.0	A572 (1)	CB	Asym.	0.62	N/A[a]
F5W1-CC	152.4	101.6	4.8	9.5	16.0	31.0	A572 (1)	CC	Asym.	N/A[a]	0.49
F1W2-M	152.4	101.6	19.1	6.4	4.0	42.0	A572 (2)	M	Sym.	1.12	0.91
F3W2-M	152.4	101.6	9.5	6.4	8.0	45.0	A572 (1)	M	Asym.	0.79	0.62
F3W2-CB	152.4	101.6	9.5	6.4	8.0	45.0	A572 (2)	CB	Asym.	0.73	N/A[a]
F2W3-M	152.4	101.6	12.7	4.8	6.0	58.7	A572 (1)	M	Sym.	1.08	0.70
F2W3-CB	152.4	101.6	12.7	4.8	6.0	58.7	A572 (2)	CB	Sym.	0.68	N/A[a]
F2W3-CC	152.4	101.6	12.7	4.8	6.0	58.7	A572 (1)	CC	Sym.	N/A[a]	0.51
F4W3-M	152.4	101.6	7.9	4.8	9.6	60.7	A572 (2)	M	Asym.	0.79	0.63
F5W3-M	152.4	101.6	4.8	4.8	16.0	62.0	A572 (1)	M	Asym.	0.59	0.45
F5W3-CB	152.4	101.6	4.8	4.8	16.0	62.0	A572 (1)	CB	Asym.	0.53	N/A[a]
F5W3-CC	152.4	101.6	4.8	4.8	16.0	62.0	A572 (1)	CC	Asym.	N/A[a]	0.44

[a]Not available because the loading protocol is intended to approximate the seismic demands on flanges in beams (columns).

Table 2-2. Limiting slenderness ratios for flanges and webs

Description of element	Element slenderness ratio	Limiting width-to-thickness ratio		
		λ_r[a] (nonslender)	λ_{md}[b] (moderately ductile)	λ_{hd}[b] (highly ductile)
Flanges of rolled I-shaped sections	$b/2t_f$	$0.56\sqrt{E/F_y}$	$0.40\sqrt{E/R_yF_y}$	$0.32\sqrt{E/R_yF_y}$
Flanges of built-up I-sections	$b/2t_f$	$0.64\sqrt{k_cE/F_y}$ $0.35 \le k_c \le 0.76$ where $k_c = 4/\sqrt{h/t_w}$	$0.40\sqrt{E/R_yF_y}$	$0.32\sqrt{E/R_yF_y}$
Webs of doubly symmetric rolled and built-up I-shaped sections	h/t_w	$1.49\sqrt{E/F_y}$	For $C_a \le 0.114$ $3.96\sqrt{E/R_yF_y}(1-3.04C_a)$ For $C_a > 0.114$ $1.29\sqrt{E/R_yF_y}(2.12-C_a)$ $\ge 1.57\sqrt{E/R_yF_y}$ where $C_a = P_u/\varphi_c P_y$ (LRFD)	For $C_a \le 0.114$ $2.57\sqrt{E/R_yF_y}(1-1.04C_a)$ For $C_a > 0.114$ $0.88\sqrt{E/R_yF_y}(2.68-C_a)$ $\ge 1.57\sqrt{E/R_yF_y}$ where $C_a = P_u/\varphi_c P_y$ (LRFD)

[a]AISC (2016c)
[b]AISC (2016b)

The built-up T-section and WT-section specimens were made of ASTM A572 Gr. 50 steel and A992 steel, respectively. The steel was ordered in two batches, and two coupons were taken from each plate in each batch and tested in accordance with ASTM E8 (ASTM 2015). Table 2-3 summarizes the average material properties of the two coupons from each batch of material.

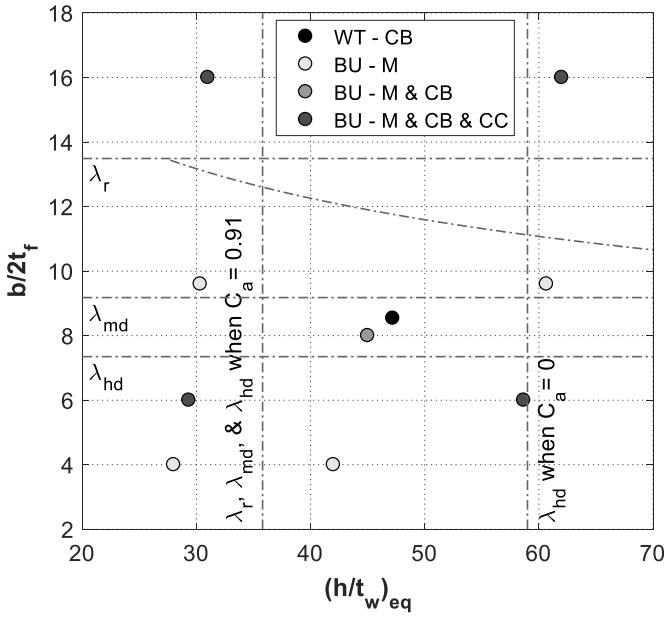

Figure 2-3. Element slenderness ratios of specimens along with code-specified limiting ratios for highly ductile (λ_{hd}), moderately ductile (λ_{md}), and non-slender (λ_r) elements. WT: WT sections. BU: built-up section

Table 2-3. Results of Tensile Coupon Tests

Material	t (mm)	Batch 1			Batch 2		
		F_y (MPa)	F_u (MPa)	Elongation (%)	F_y (MPa)	F_u (MPa)	Elongation (%)
A992	9.65	357	470	39.8	381	481	49.9
	5.84	360	475	35.6	400	487	42.0
A572	19.1	357	506	36.2	380	540	-
	12.7	380	460	40.5	407	464	36.9
	9.53	414	469	41.7	401	465	54.9
	7.94	440	484	31.3	471	537	42.3
	6.35	425	470	27.6	365	448	48.3
	4.76	408	513	29.2	368	496	36.9

The specimens are tested using the setup shown in Figure 2-4. The web plate is welded to the flange plate using a 2-sided fillet weld to form the built-up specimens. The specimens are then welded to fixture plates that are bolted to the fixed loading heads of a 2.22 MN uniaxial hydraulic load frame. Axial loading is applied in displacement control. The applied axial load is directly measured by a load cell, while the axial displacement is measured by an optical tracking system with the markers located at the center and four edges of the fixture plates. The five measured relative axial displacements were averaged to obtain only the deformation in the specimen.

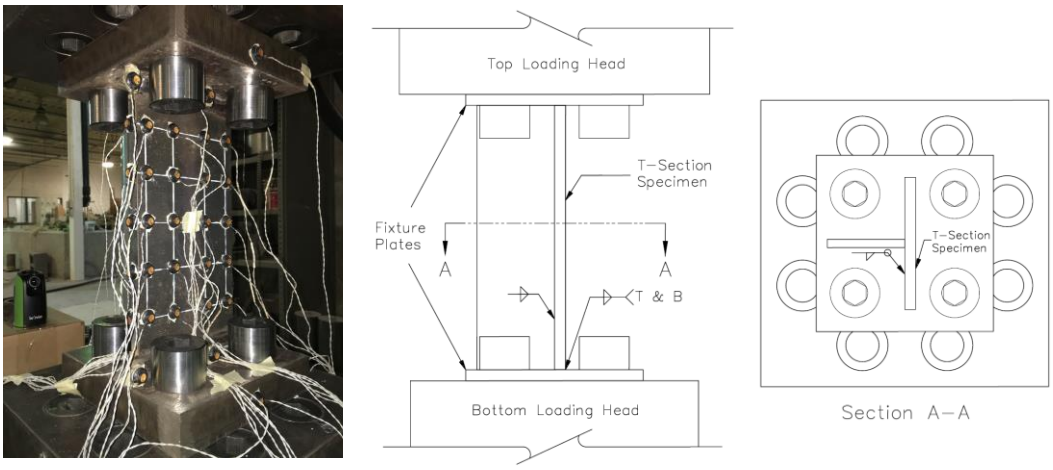

Figure 2-4. Test setup

2.5.2. Loading Schemes

Three different loading protocols are employed in the experiment: (1) monotonic axial compression (designated M); (2) cyclic axial loading that is intended to approximate the seismic demands on flanges in beams (cyclic-beam, designated CB); and (3) cyclic axial loading intended to approximate the seismic demands on flanges in columns (cyclic-column, designated CC). The monotonic loading scheme is used to obtain the buckling and post-buckling capacity of the cross-section without cyclic degradation. The cyclic loading schemes reflect the axial demands on beams

and columns under the symmetric cyclic drift loading specified in the AISC seismic provisions (2016b).

It is assumed that the overall strain distribution across the cross-section of a beam is linear about the neutral axis and that the neutral axis location does not fluctuate with cyclic loading. For a plastic hinge rotation, θ, the flange is subjected to an axial deformation $\Delta = d\theta/2$ in the plastic hinge region, where d is the section depth. Assuming that the plastic hinge length is d (MacRae et al. 1990), then the flange is subjected to a NAD = $\Delta/L = d\theta/2d = \theta/2$ in the plastic hinge region. As a result, the NAD protocol applied to the T-section member, i.e. the CB protocol, is half the beam rotation specified in the beam-column connection qualification protocol. For example, NAD = 2% when a beam achieves 4% plastic rotation, a limit commonly associated with highly ductile response. The resulting CB protocol is shown in Figure 2-5.

The existence of axial force in columns increases the severity of web local buckling in column members and causes the columns to shorten under cyclic loading. To take this into account, the CC protocol is developed using finite element simulations of deep column specimens 1L (W24×176), 2L (W24×131), and 3L (W24×104) tested in Ozkula et al. (2017b) and subjected to symmetric cyclic drift loading. The three columns specimens are subjected to a constant axial load of $0.18P_y$. The computed axial demand histories are averaged and smoothed to get the CC loading protocol shown in Figure 2-5. The NAD corresponding to a column drift of 4% in the selected CC protocol is 8.3%. Although this protocol is specific to certain column sizes (similar to those considered in this research) and may not be applicable to other columns, it reflects the flange behavior commonly seen in experimental column tests.

The loading rate for monotonic loading (M protocol) is 1.52 mm/min. Faster rates of 3.05 mm/min for small deformations and 12.2 mm/min for 4% NAD or larger are used for the cyclic loading tests (the CB and CC protocols) to reduce test duration to a reasonable time.

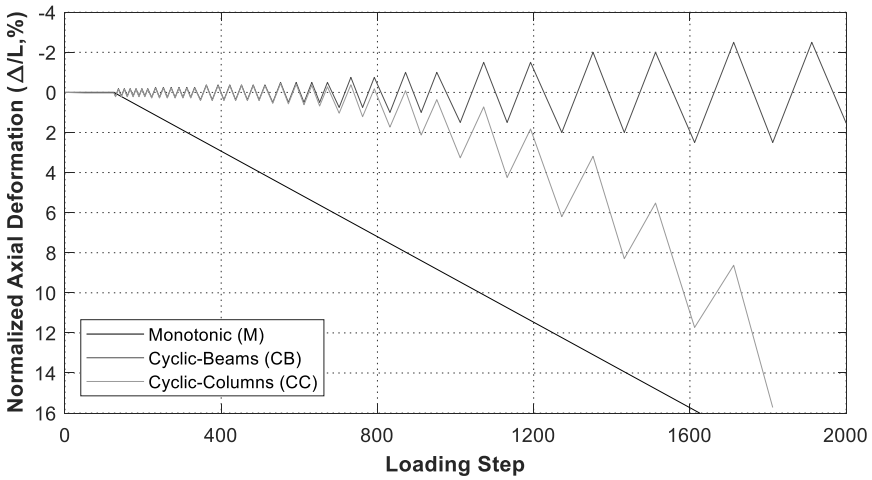

Figure 2-5. Employed loading schemes

2.6 Experimental Results

2.6.1. Comparison between WT-Section and T-Section Specimens

Figure 2-6 shows a comparison between the hysteresis responses and backbone curves of a WT-section (W12×26) and a T-section (F3W2) specimen with similar slenderness ratios subjected to the CB loading protocol. Except for the sudden drop in the backbone curve under tension due to a lapse of applying axial displacement, Figure 2-6 clearly shows that both specimens yield generally similar responses in terms of peak load, post-buckling strength, post-peak degradation rate and hysteresis under cyclic loading. This comparison provides confidence in the use of built-up sections in this study and suggests that the findings also can be applied to W-sections.

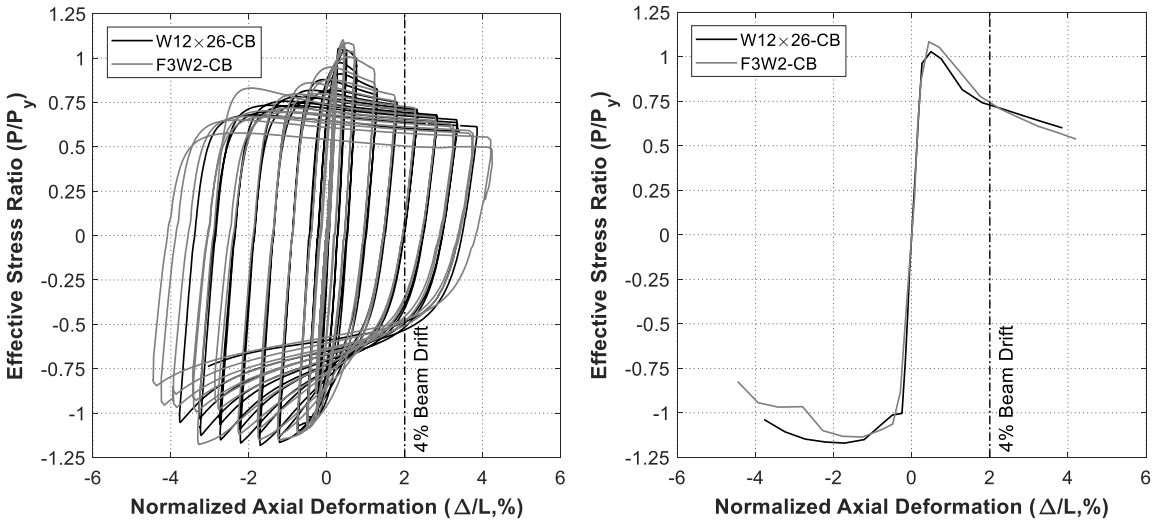

(a) (b)

Figure 2-6. Comparison of (a) hysteresis responses and (b) backbone curves for WT-section and T-section specimens with similar slenderness ratios under the CB protocol

2.6.2. FLB Modes

The specimens subjected to both monotonic and cyclic loading exhibit two distinct buckled shapes, asymmetric and symmetric FLB, as shown in Figure 2-7(a, d) and (b, e), respectively. The buckling mode of each specimen is documented in Table 2-1. Most of the specimens exhibit asymmetric buckling behavior, where the flange and web interact with each other and experience local buckling simultaneously. The test data indicates that specimens that have comparable flange and web slendernesses are more likely to experience asymmetric buckling.

A few specimens with a very stocky flange and a slender web, e.g. Specimen F1W2 with $b/2t_f$ of 4.0 and $(h/t_w)_{eq}$ of 42.0, buckle in a symmetric mode, i.e. both half flanges bend together in the direction of the plane of the web, as shown in Figure 2-7(b). In this case, the flange itself suffers from weak-axis flexural buckling because the restraint provided by the web is relatively minimal

and not able to alter the flange buckling mode. Within the studied range of slenderness ratios, only the specimens with $b/2t_f \leq 6$ are susceptible to this mode.

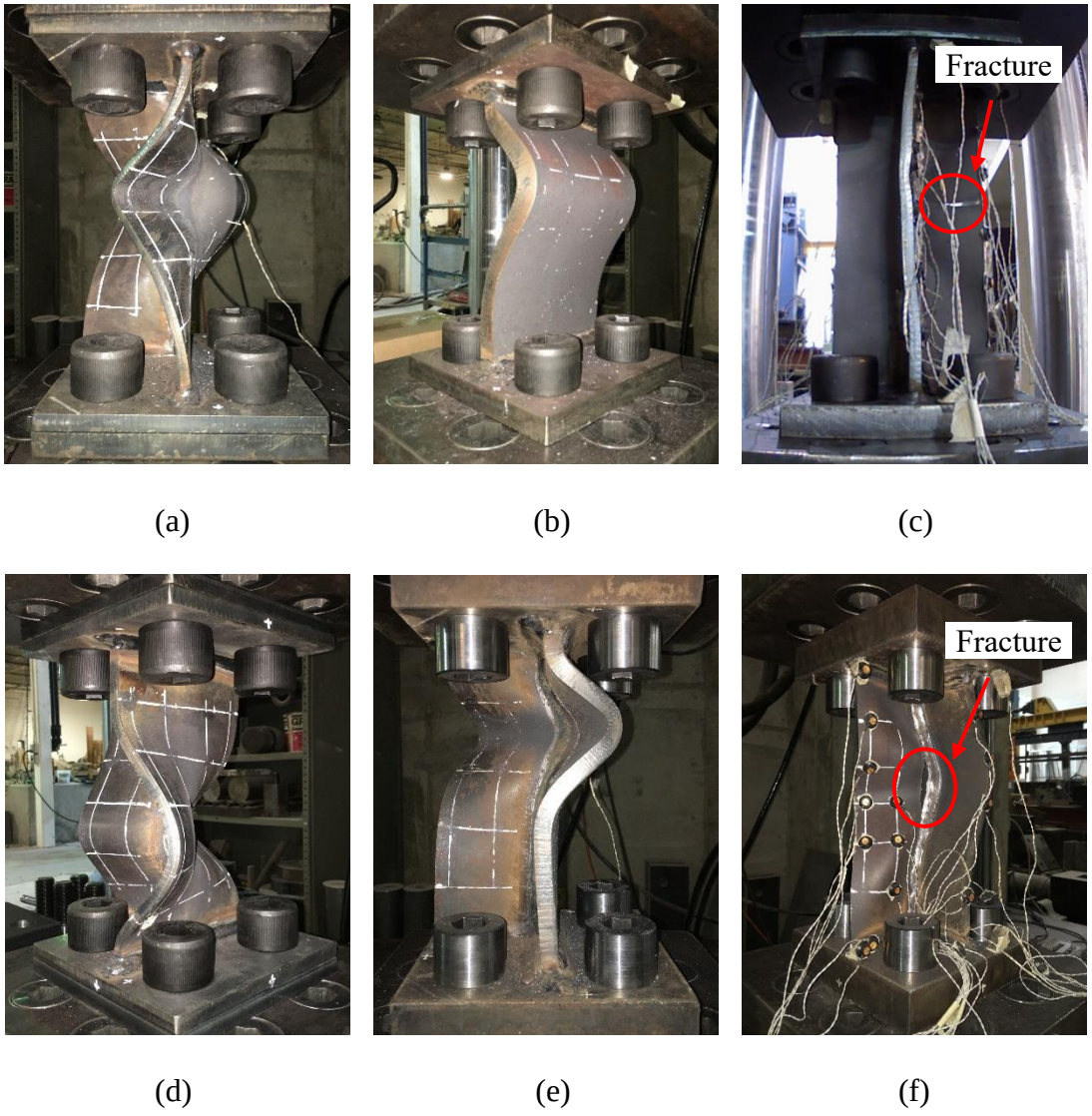

Figure 2-7. Asymmetric local buckling in (a) Specimen F4W3-M and (d) Specimen F3W2-M; symmetric local buckling in (b) Specimen F1W2-M and (e) Specimen F2W1-CC; and fracture in (c) Specimen F2W1-CB and (f) Specimen F2W3-CB

The asymmetric buckling behavior is commonly seen in plastic hinge zones of deep columns subjected to combined axial and lateral loading (Elkady and Lignos 2017; Ozkula et al. 2017b), lending credence to the premise of this study, i.e. the T-section specimens can replicate certain

flange buckling responses and be used to study the flange behavior in plastic hinge regions under large lateral displacements. The symmetric buckling behavior has also been seen in the previous tests (Ozkula et al. 2017a), but in columns with the extreme combination of a stocky flange and a very stocky web, e.g. W14×176 with $b/2t_f$ = 5.97 and h/t_w = 13.7.

2.6.3. Response under Monotonic Loading

The nine specimens under monotonic loading are compressed to 10% NAD and ESR is computed using the material yield strength obtained from the coupon tests listed in Table 2-3. The ESR versus NAD curves of the nine T-section specimens are plotted in Figure 2-8, where specimens with the same flange thickness are plotted in the same color, while the specimens with the same web thickness are plotted in the same line style.

By comparing the curves of the specimens with a web thickness of 9.5 mm, i.e. W1 specimens plotted as solid curves, it is clear that the smaller the $b/2t_f$, the higher the buckling and post-buckling strength. For example, specimen F1W1-M's peak strength reaches 1.24P_y ($b/2t_f$ = 4.0), meanwhile as $b/2t_f$ increases, the buckling strength drops to 1.18P_y, 1.07P_y, and 1.02P_y for F2W1-M, F4W1-M, and F5W1-M, respectively. All four W1 specimens can reach P_y even though F5W1-M has a $b/2t_f$ = 16.0, which is larger than λ_r = 13.5. The better than expected performance results from the fixed end condition, which causes a full buckling wavelength that is commonly seen in experiments and simulations (Ozkula et al. 2017a, Wu et al. 2018a), unlike the pinned end conditions conservatively assumed in the AISC specification (2016c). In terms of post-buckling capacity, λ_{hd} works well for identifying the sections with superior ductility. Specimens with a $b/2t_f$ lower than λ_{hd} = 7.35, i.e. F1W1-M and F2W1-M, maintain a large post-buckling capacity of at least P_y until 8.9% and 4.5% NAD, respectively, which are much higher than NAD = 2% that

corresponds to 4% beam drift. On the other hand, F4W1-M and F5W1-M that have a $b/2t_f$ larger than λ_{hd} exhibit rapid strength degradation after reaching the peak values and can only maintain P_y up to NADs of 0.8% and 0.7%, respectively.

The effect of equivalent web slenderness ratio, $(h/t_w)_{eq}$, on flange behavior is not significant when $b/2t_f$ is smaller than 10 as can be seen from the comparison of specimens F1W1-M, F2W1-M, and F4W1-M to their counterparts with slenderer webs, i.e. F1W2-M, F2W3-M, and F4W3-M. For specimens with slender flanges, e.g. F5W1-M and F5W3-M, the effect of $(h/t_w)_{eq}$ is significant because the slender flange negatively interacts with the slender web. As shown in Figure 2-8, while Specimen F5W1-M has a peak strength of $1.02P_y$, F5W3-M reaches an axial capacity of only $0.7P_y$. Overall, for flanges under monotonic compression, the λ_r and λ_{hd} limits in current seismic provisions seem to be reasonable.

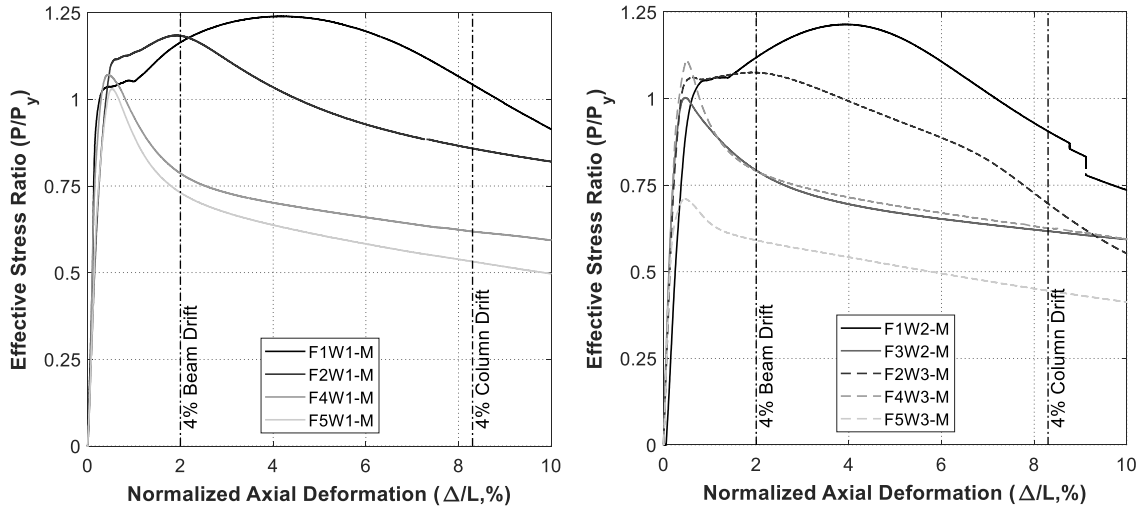

Figure 2-8. Effective stress ratio-normalized axial deformation curves of specimens under monotonic axial compression: (a) W1 specimens; (b) W2 and W3 specimens

2.6.4. Effect of Cyclic Loading

The resulting relationship between ESR and NAD of the specimens under the three applied loading protocols are plotted together in Figure 2-9. Positive and negative NAD represent compression and tension, respectively, to be consistent with Figure 2-8.

Although the difference in peak compression strength between specimens under the M and CB protocol is not significant, the degradation rate of post-buckling compression strength of the specimens subjected to CB demands is considerably faster than their monotonic counterparts. For example, as shown in Figure 2-9(c), while Specimen F2W1-M maintains an axial capacity of at least P_y up to 4.5% NAD, Specimen F2W1-CB can only sustain P_y to 1.5% NAD and quickly degrades to $0.85P_y$ at 2% NAD, suggesting that moment capacity of beams satisfying the λ_{hd} limits starts to degrade after reaching 3% drift. The effect is even more pronounced for Specimen F2W3-CB. These results suggest that the web restraint has a large impact on the rate of degradation with continued cycling to large NAD levels. The strength degradation rates for specimens with high $b/2t_f$, e.g. specimen F5W1-CB and F5W3-CB, are comparable to their monotonic counterparts before 2% NAD. After reaching 2% NAD, the rate of degradation is much faster. For example, the post-buckling strength of both specimens under the CB protocol is $0.51P_y$ and $0.44P_y$ at 3% NAD, respectively, compared to $0.67P_y$ and $0.57P_y$, respectively, under monotonic loading.

Degradation of tensile strength occurs with cyclic loading, but the rate is substantially smaller than that under compression. Tensile degradation generally begins during the 1.5% or 2% NAD cycles. Specimens typically fail when the tensile strength drops to $0.8P_y$. Failure occurs due to fracture, as marked by red circles in Figure 2-9. One key characteristic that slenderness ratios influence is the recovery of the tensile strength after unloading from compression. Specifically, more tensile

strain is required to stretch out the buckled shape and recover tensile strength for specimens that have higher $b/2t_f$ and $(h/t_w)_{eq}$, i.e. experience more severe local buckling. For example, during the 2% NAD cycle, Specimen F2W1-CB can reach $0.8P_y$ at 0.7% NAD, but Specimen F5W3-CB has to be pulled to -1.3% NAD (tension side) to recover the same level of tensile strength, as shown by the red (thicker) lines in Figure 2-9(c) and (b).

Although specimens under the CB protocol have the same buckled shape as the ones under the M protocol, they eventually failed by ultra-low-cycle fatigue under tension. As shown in Figure 2-7(c), for Specimen F2W1-CB, fracture initiates at midpoints along the outer edges of the flange and web, where the highest strain level occurs due to the buckling behavior. Because of the connection between strain level and buckling behavior, fracture occurs earlier for specimens with larger $b/2t_f$ and $(h/t_w)_{eq}$ due to buckling during earlier cycles. For example, fracture occurs during the 3.5% NAD cycle for Specimen F5W3-CB and is delayed to the 4.5% and 5.5% NAD cycles for Specimens F5W1-CB and F2W1-CB, respectively. One exception is that Specimen F2W3-CB suffers from earlier fracture at the midpoint along the flange-web connection during the 3% NAD cycle due to symmetric buckling behavior, as shown in Figure 2-7(f), suggesting that buckling mode also has an influence on fracture behavior. Although ultra-low-cycle fatigue is the eventual failure mode for all specimens, severe strength degradation under compression occurred much earlier and therefore is a design concern.

The responses of the four specimens under the CC protocol are shown in Figure 2-9. The backbone curves of the F5 specimens are almost identical to the responses of their monotonic counterparts. The F2 specimens under the CC protocol, unlike their monotonic counterparts, buckle in a symmetric mode and have a lower backbone curve. From Figure 2-9 it can be seen that all specimens under the CC protocol experience much less tensile plastic strain than specimens under

the CB protocol, allowing the specimens to deform to greater NADs without succumbing to ductile fracture. Nevertheless, the ESR of the specimens under the CC protocol at the 8.3% NAD that corresponds to 4% column drift is lower than that of the specimens under the CB protocol at the 2% NAD that corresponds to 4% beam drift, as can be observed from Figure 2-9. For example, the ESR of F2W1-CC at the 8.3% NAD and F2W1-CB at the 2% NAD is 0.78 and 0.85, respectively. These lower ESRs may greatly degrade column capacity and require further investigation.

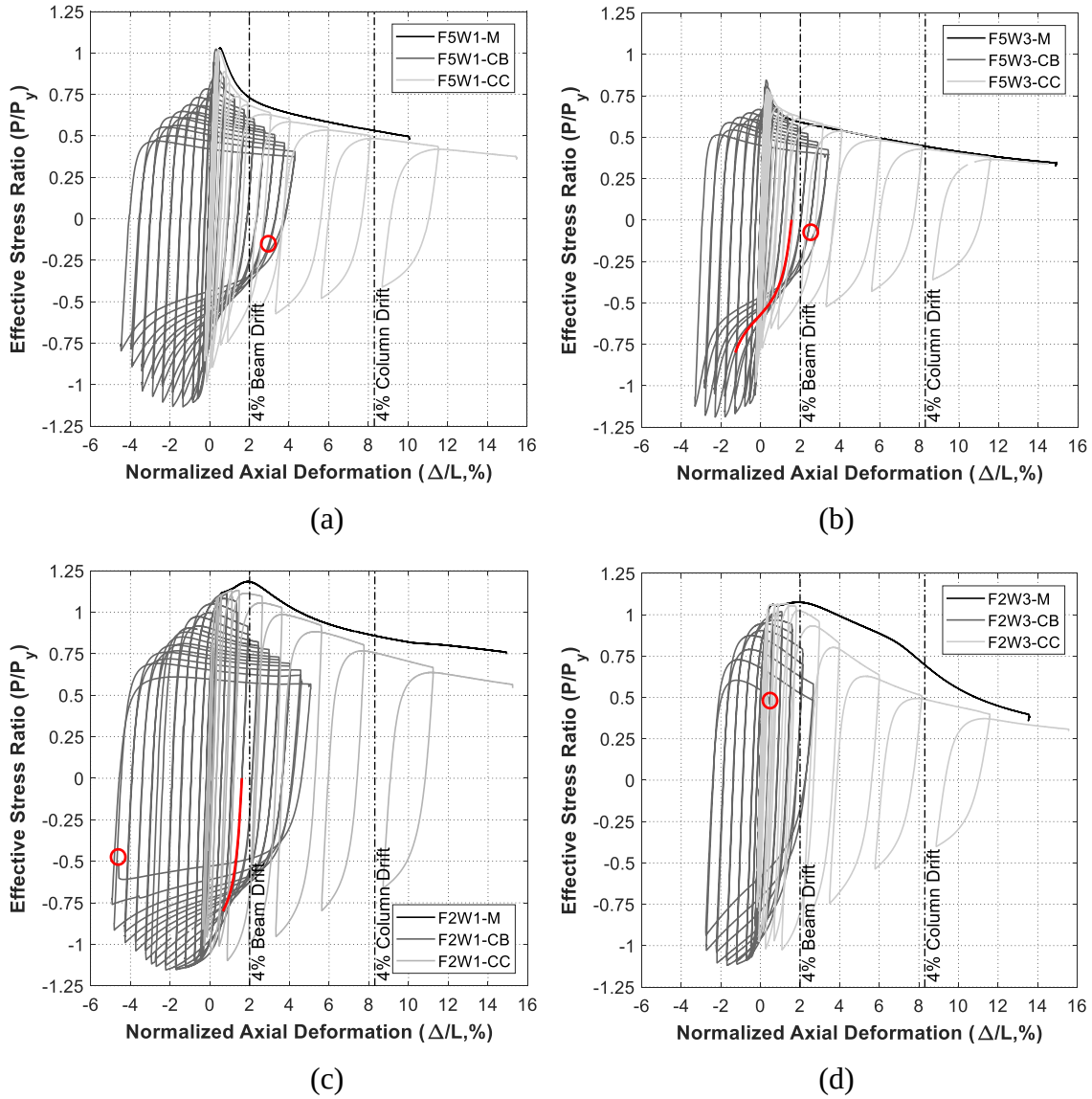

Figure 2-9. Comparison of axial force ratio-axial strain curves between different loading schemes for Specimen (a) F5W1; (b) F5W3; (c) F2W1; and (d) F2W3

2.7 Finite Element Simulations

Computational simulation is used to expand the parameter space and gain greater insight into the effects of FLB on member capacity.

2.7.1. Validation

In addition to the validation effort discussed earlier in Section 2.3, the modeling approach is further validated using the experimental data presented in Section 2.6. Due to limited space, only a comparison of responses of Specimen F3W2-M and F5W1-CC are shown in Figure 2-10. The measured specimen dimensions and material properties obtained from tensile coupon tests in Table 2-3 are used in the finite element simulation. The peak strength, post-buckling strength, cyclic strength degradation rate obtained from the simulation match well with those measured during the physical testing and provide additional confidence that the employed modeling techniques can generate reasonable behavior.

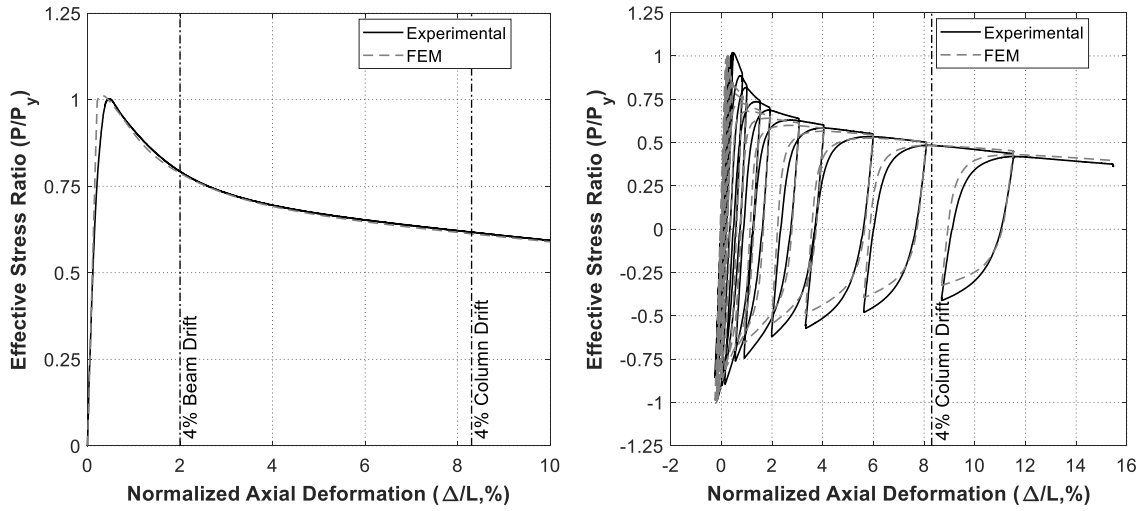

Figure 2-10. Comparison of responses between experimental and simulation results for Specimen (a) F3W2-M and (b) F5W1-CC

2.7.2. Section Selection and Performance Parameter

To study the effect of slenderness ratio on cyclic capacity of column flanges, finite element models of T-sections with b = 152.4 mm, $d/3$ = 101.6 mm, and $b/2t_f$ and $(h/t_w)_{eq}$ ranging from 6 to 16 and 24 to 56, respectively, are created using the modeling approach described in Section 2.3. The values of b and d are the same as the tested specimens, and the range of slenderness ratios is selected to cover most commercial standard W-section sections. The T-section models are axially loaded according to the CC protocol to further study the lower ESRs observed from these specimens.

In all simulation cases, ESR is used to track cross-section capacity at different column drift levels. As noted earlier, column drift levels are gaged from detailed finite element analysis of entire columns. Figure 2-11 shows the results of a T-section where $b/2t_f$ = 6 and $(h/t_w)_{eq}$ = 32. The ESR is 0.94, 0.83, 0.76 and 0.69 at column drift levels of 1%, 2%, 3%, and 4%.

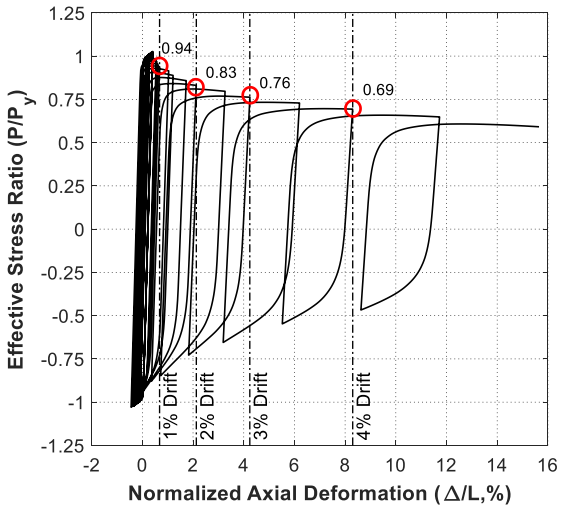

Figure 2-11. The effective stress ratio (ESR) corresponding to different column drifts for the T-section with $b/2t_f$ = 6 and $(h/t_w)_{eq}$ = 32 under the CC protocol

2.7.3. Simulation Results

The ESRs of the various T-sections are plotted in Figure 2-12 against $b/2t_f$ for column drift levels of 1% through 4% for different values of $(h/t_w)_{eq}$. It is clear that $(h/t_w)_{eq}$ has a negative effect on ESR. While the negative effect is significant when the drift level is small, 1%, it diminishes as both $(h/t_w)_{eq}$ and drift level decrease in value. The effect also diminishes as the value of $b/2t_f$ decreases. The above results further confirm the trend observed from the tests: the effect of $(h/t_w)_{eq}$ is significant only on post-buckling strength at small strain levels when the flange is slender. An important observation from Figure 2-12(d) is that the ESR curves tend to cluster together at drift levels in excess of 2%, suggesting that it is reasonably accurate to ignore the effect of $(h/t_w)_{eq}$ on λ_{hd} limits for the flanges.

Figure 2-12 also shows that both $b/2t_f$ and drift level adversely affect ESR. For example, for T-sections with $(h/t_w)_{eq}$ = 56, the ESR corresponding to 1% drift decreases from 0.92 to 0.61 when $b/2t_f$ increases from 6 to 16. ESR drops significantly as the column drift increases to 4%, where its range decreases from 0.92 - 0.61 to 0.70 - 0.50 for $b/2t_f$ ranging from 6 to 16. Through a regression analysis, the effect of $b/2t_f$ and drift level on ESR can be quantified by the following bilinear equation with $b/2t_f$ = 8 as a transition point:

$$ESR = (0.0575 - 0.422DR)\left(23.3 - \frac{b}{2t_f}\right) \text{ for } 6 \leq \frac{b}{2t_f} \leq 8$$

$$ESR = (0.0205 - 0.15DR)\left(51 - \frac{b}{2t_f}\right) \text{for } 8 < \frac{b}{2t_f} \leq 16 \qquad (2\text{-}1)$$

where DR is the column drift ratio, e.g. 0.04 rad for the cases in Figure 2-12(d). Equation (2-1) is plotted in red in Figure 2-12 and portrays the negative effect of both $b/2t_f$ and drift level on ESR.

Another observation is that the degradation of ESR with drift level could be substantial. According to Equation (2-1), when $b/2t_f=\lambda_{hd}$, ESR drops from 0.78 to 0.65 (17% decrease) as *DR* increases from 2% to 4%.

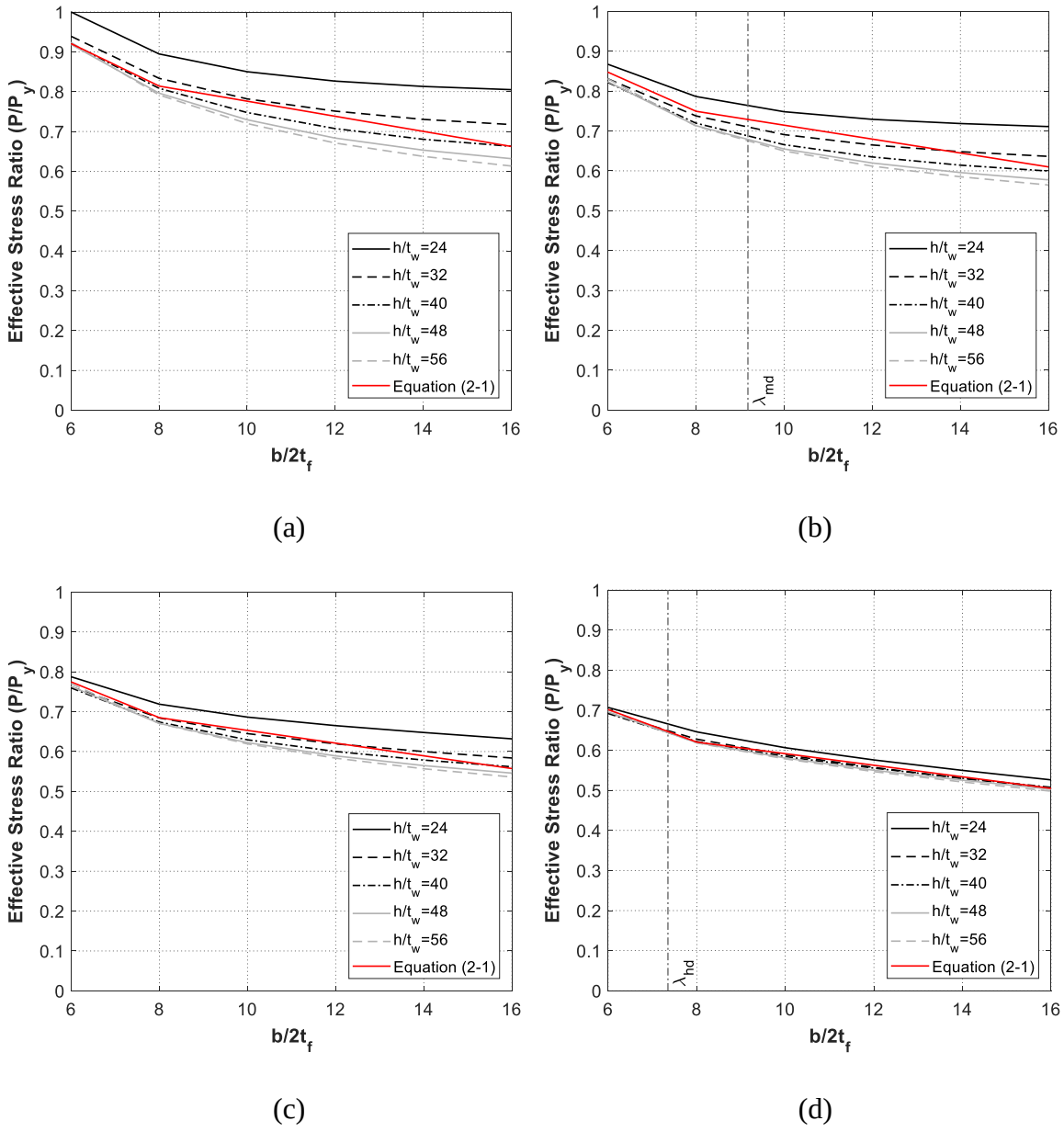

Figure 2-12. Effective stress ratio (ESR) of T-sections at column *DR* of (a) 1%; (b) 2%; (c) 3% and (d) 4%

2.8 Comparison with Current AISC Seismic Provisions

All specimens with $b/2t_f$ and $(h/t_w)_{eq}$ smaller than λ_r have a buckling strength larger than P_y under all loading schemes. Even when $b/2t_f$ exceeds λ_r, e.g. F5W1 specimens, a peak strength of at least P_y is still achieved. While not shown here, the computational study also supports this finding. As a result, the current λ_r limit is considered adequate for flanges in beams and columns under the monotonic and cyclic loading schemes considered in this work.

From the experimental results, it is also clear that λ_{hd} is reasonable under monotonic loading. This assessment is based on the observed good post-buckling responses exhibited by monotonically loaded specimens with F1 and F2 flanges. The same can be said for specimens subjected to cyclic axial loading for demands under the CB protocol. The post-buckling degradation seen under compression is offset by the mild degradation in tensile strength, which combined, will likely allow most available cross-sections to carry at least 80% of their plastic moment capacity up to 4% rotation. Therefore, current limits on λ_{hd} for flanges appear to provide appropriate highly ductile behavior for beams under cyclic loading.

Specimen F2W1-CC, which has a $b/2t_f$ smaller than the current λ_{hd} limit, exhibits an ESR of $0.78P_y$ at a NAD corresponding to 4% column drift. Equation (2-1) indicates that ESR reaches 0.65 at the highly ductile slenderness limit. The evidence in this study suggests that, barring other failure modes such as global instability, a W24 column with slenderness characteristics similar to those considered would be able "to withstand significant plastic rotation of 0.04 rad or more" per current design philosophy and still support a substantial axial load. However, the key question of whether the moment or axial capacities have been degraded too much by cyclic FLB is not addressed in current seismic provisions. Unlike beams, where current seismic design provisions require that the

moment capacity be at least 80% of the plastic capacity at 4% drift, columns have no such requirement. The research in this study points out the need for more precise performance requirements for columns.

2.9 Conclusions

The effect of cyclic FLB on the capacity of structural members in special moment frames was experimentally and computationally investigated in this study. Nineteen half-scale T-section specimens were axially loaded to represent the flange/web subassembly in the plastic hinge region of a wide flange section under combined axial and flexural loading. The specimens were selected to cover a wide range of slenderness ratios and subjected to three different loading schemes. The loading schemes included monotonic compression, meant to obtain the flange capacity without cyclic degradation, and two cyclic axial loading histories, one that reflected the axial demands on beam flanges and another for column flanges under cyclic drift loading. To further study the cyclic behavior of column flanges and justify the observation from the test results, a parametric computational study with different slenderness ratios was performed. The effect of slenderness ratios on column compression capacity due to flange strength degradation was then evaluated.

The test results showed that most T-section specimens could reach a peak strength of P_y regardless of the value of $b/2t_f$, but $b/2t_f$ substantially influenced post-buckling behavior. Under monotonic loading, the current value for λ_{hd} for a flange was shown to be a boundary between large buckling capacity and rapid degradation after reaching peak strength. The effect of $(h/t_w)_{eq}$, on the other hand, was shown to be secondary and became significant only when both $b/2t_f$ and $(h/t_w)_{eq}$ were large and negatively interacted with each other.

Specimens under the CB loading protocol exhibited much more severe compressive strength degradation than the monotonic protocol. Depending on a specimen's $b/2t_f$, the compressive strength dropped to as low as 0.53 P_y at deformation levels that corresponded to 4% beam rotation. The tensile strength had a much milder degradation rate than the compressive strength. However, the required tensile strain for recovery of tensile strength after unloading from compression depended on the slenderness ratio due to the effort of stretching out the buckled shape.

The backbone curves of specimens under CC loading were much higher than those for specimens under CB loading and were quite close to the responses under M loading. This result was attributed to the smaller tensile plastic strain demands and led to a milder cyclic degradation rate under compression. Nevertheless, the degradation at higher drift levels could be substantial and could compromise the axial and flexural capacities of the columns.

The experimental and computational data was used to evaluate the current AISC seismic provisions. It was shown that the current λ_r limit is adequate for flanges in beams and columns under the monotonic and cyclic loading schemes considered in this work. It was also shown that λ_{hd} is reasonable for members under monotonic loading and CB loading, which is representative of the demands seen in beams. The conclusion for λ_{hd} and λ_{md} under CC loading, representative of the demands seen in columns, was not definitive because the performance expectations of the AISC seismic provisions are not as explicit as they are for beams. The research outlined in this study provides useful input to refine current specifications to address this issue.

The evaluation in this study is only valid for the specific wide flange section sizes, loading protocols and range of parameters studied. Although this research points out specific drawbacks

in the current AISC seismic provisions, additional research is needed to broaden the results and draw comprehensive conclusions that warrant specification changes.

CHAPTER 3

COLLAPSE RESISTANCE OF DEEP STEEL COLUMNS IN SPECIAL MOMENT FRAMES

3.1 General

This chapter reiterates, with greater specificity, concerns about the seismic behavior of deep steel columns and presents a computational study of their seismic collapse resistance using detailed finite element models. To create and properly evaluate realistic models of columns in special moment frames, loading protocols that represent seismic demands on first-story columns are developed through collapse simulations of complete frames (Section 3.3). A parametric simulation is performed to identify the most realistic loading and boundary condition for column models (Section 3.4). A set of deep columns that cover a wide range of both global and element slenderness ratios is modeled to study key parameters affecting column collapse behavior (Section 3.5). The insight gained from the simulations is used to evaluate current design recommendations and propose improvements suitable for adoption into future seismic provisions (Section 3.6).

3.2 Motivation

As discussed in Chapter 1, the use of deep, slender wide flange sections, with a depth of 600 mm (24 inches) or greater, has been prevalent in special moment frames (SMFs) since the late 1990s. The large depth, high in-plane flexural stiffness and strength make such sections an attractive choice for engineers seeking to satisfy current panel zone, drift and strong-column/weak-beam

design criteria. However, deep columns are also susceptible to weak-axis global and lateral torsional buckling, leading to potential vulnerabilities that are not yet fully understood (NIST 2011).

To address this shortcoming, NIST (2011) proposed a comprehensive analytical and experimental research plan to better understand the inelastic behavior of deep steel columns. The plan had three categories of proposed research needs: member, subassemblage, and system level studies. A number of researchers have conducted computational and experimental studies at the member level (Fogarty and El-Tawil 2015; Elkady and Lignos 2015a, 2017; Ozkula et al. 2017b) and computational studies at the system level (Wu et al. 2017), but no studies have yet addressed the subassemblage level.

Using computational simulation, Fogarty and El-Tawil (2015) investigated the collapse resistance of steel columns under combined axial and symmetric cyclic drift loading. They noted that many deep sections considered highly ductile per current provisions cannot reach a 4% drift ratio under feasible axial loads (0.2-0.4P_y). They also showed that while the flange slenderness ratio ($b/2t_f$) has a minor effect on column collapse capacity when the current AISC highly ductile limit for flange slenderness is satisfied, web (h/t_w) and global slenderness (L/r_y, where L is the unbraced column length and r_y is radius of gyration about the column's weak-axis) ratios are highly influential. They proposed equations that assessed the peak axial load capacity of the column as a function of these parameters.

Elkady and Lignos (2015a) studied the cyclic behavior of deep columns through detailed finite element analyses. They noted that current seismic requirements for highly ductile sections were not adequate for interior columns subjected to an axial load of 0.2-0.35P_y. Ozkula et al. (2017b)

conducted experiments to study the cyclic behavior of deep column specimens under a symmetric cyclic drift loading combined with a constant axial load of 0.2-0.6P_y. Most specimens were not able to deliver a plastic rotation of 0.03 radian without a reduction in maximum flexural strength of 10% or more during the test.

A common finding in the above studies is that the capacity of deep steel columns may be lower than expected by current seismic design provisions (AISC 2016b) for highly ductile members, especially when the axial load is larger than 0.20P_y. However, the symmetric loading schemes as well as idealized boundary conditions employed in these studies do not fully reflect system-level demands. Wu et al. (2017) observed much better component performance in their system studies and suggested that system demands could be significantly milder than those used in studies of isolated columns. Elkady and Lignos (2017) also pointed out the significant difference in column capacity under different loading protocols.

The above recent studies suggest that the inelastic behavior of deep columns is still not yet well understood. Moreover, while L/r_y was shown to be an influential variable in Fogarty and El-Tawil (2015), it is not considered in current AISC highly ductile member limits (AISC 2016b). With these shortcomings as motivation, the computational study presented in this chapter is geared towards providing new, detailed insight into deep column behavior under realistic seismic demands.

3.3 System Analysis

Earthquake-induced collapse simulations of a four-story frame are performed using ground motions selected from the far-field record set in FEMA P695 (2009). The results of the

computational studies are used to develop meaningful and realistic loading protocols for first-story columns.

3.3.1 Prototype Building

The four-story building outlined in NIST (2010) is selected as the prototype building. The building's plan is shown in Figure 3-1(a). The building has three-bay steel SMFs on each exterior side, which are assumed to resist all the seismic demands acting on the building. The circled frame in Figure 3-1(a), whose elevation is shown in Figure 3-1(b), is considered for further study in this chapter. The beam and column sections are listed in Figure 3-1(b). The frame is assumed to carry the tributary gravity loads indicated in Figure 3-1(a). The SMFs are designed with deep columns and reduced beam sections (RBS) using ASTM A992 steel in accordance with AISC (2016a, 2016b) and ASCE (2010). The site class of the building is *D* and the seismic design category (SDC) is D_{max}. Further design details of the building can be found in NIST (2010).

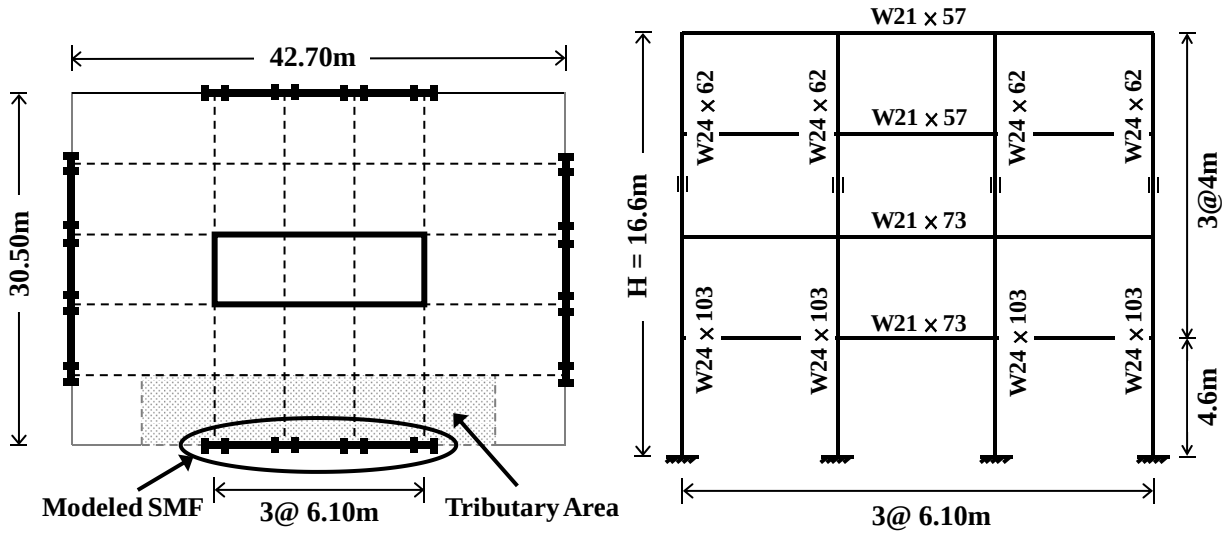

Figure 3-1. (a) Plan view of the four-story building; (b) elevation view of the modeled SMF

3.3.2 Modeling Approach

As in Section 2.3, detailed finite element models of the SMF are created and analyzed using Hypermesh (2013) and LS-DYNA (2013), respectively, with the same formulation for 3- and 4-node fully integrated shell elements, mesh size, and material model, except that the nominal strength of A992 steel is used to calibrate the hardening moduli as shown in Figure 3-2. The SMF model is assumed to be fully fixed at its base. The lateral bracing of the SMF is simulated by preventing out-of-plane translation at key nodes, as shown in (Figure 3-3(b)). Both flanges of the beams are laterally braced at locations with a spacing L_b that satisfies the maximum unbraced length for highly ductile members in AISC (2016b). Column flanges in the beam-column connection region are laterally braced at the levels of both beam flanges. System-wide P-Delta effects are considered by connecting a leaning column to the SMF with rigid truss members as shown in Figure 3-3(a). The rigid truss member at each floor is attached to the center point of the continuity plate for beam top flanges with an x-translation constraint (Figure 3-3(b)). A gravity load equal to half of the building floor mass minus that distributed to the SMF system is applied at each floor of the leaning column. Because the use of stiffness-proportional damping considerably reduces the time step in explicit schemes, only mass-proportional damping is considered (Xiaoming et al. 2015). A mass-proportional damping of 2.5%, which is consistent with recommendation in PEER/ATC-72-1 (PEER/ATC 2010), is assumed at the first mode period (1.67 s) of the SMF. Imperfections are deliberately excluded to avoid favoring pre-determined instability modes.

The axial load induced by gravity load, i.e. P_g, due to the tributary area indicated in Figure 3-1(a) is $0.18P_y$ for exterior SMF columns. This case is designated TGL2. To promote vertical progressive collapse, another case is considered where the gravity load on the SMF is increased to

a value that causes an axial load of $0.27P_y$ on the exterior SMF columns. For this case (designated TGL3), the load on the leaning column is adjusted down to ensure that the total building mass remains the same. The frames that consider other conditions including the TGL1 case are not used in this study and will be discussed in Section 4.4.

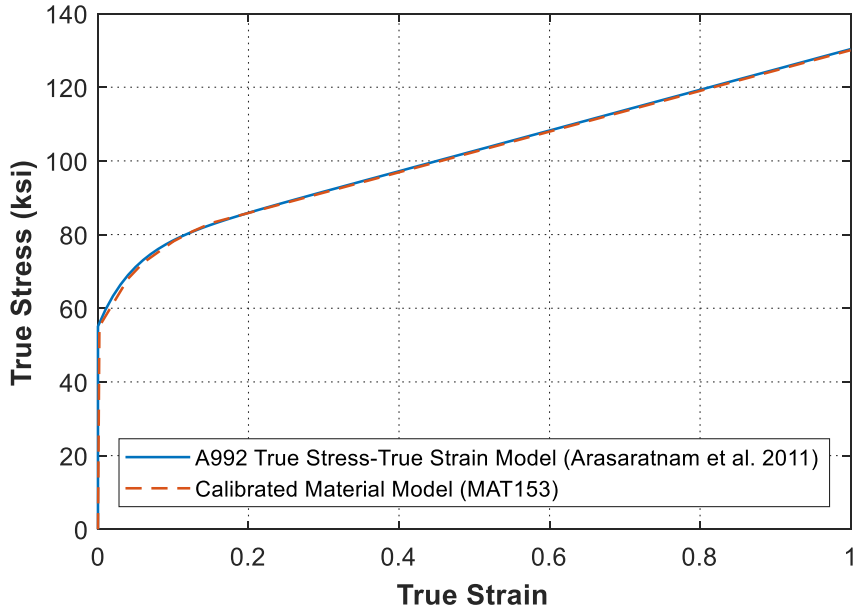

Figure 3-2. Material model calibration with true stress-true strain model for A992 steel

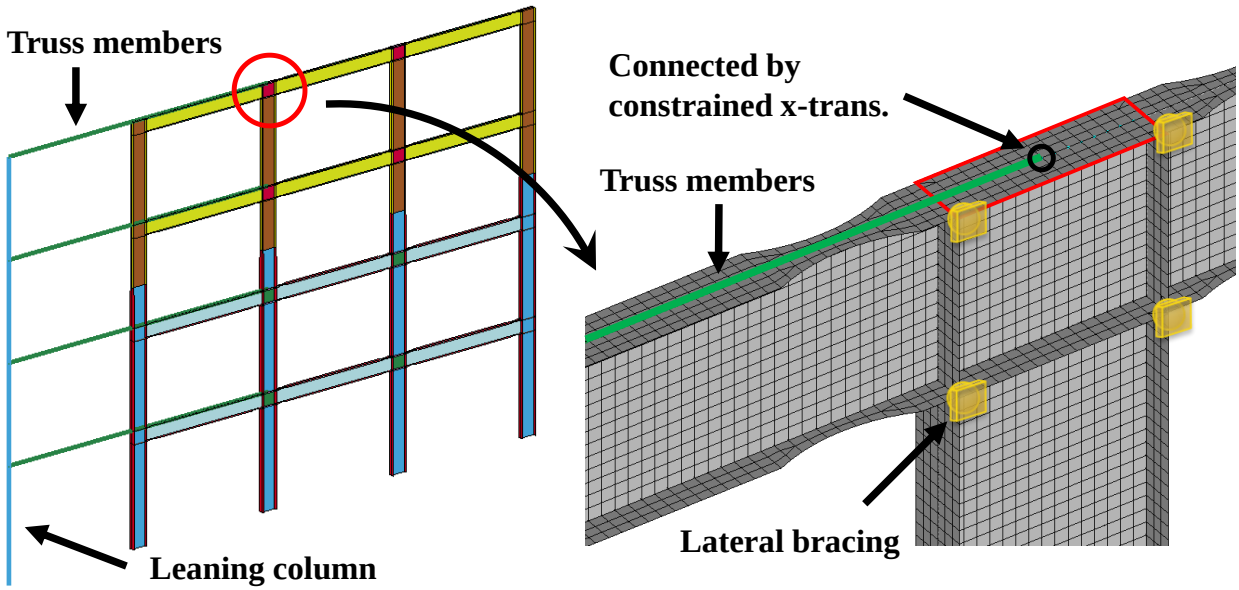

(a) (b)

Figure 3-3. Finite element models of (a) four-story SMF; and (b) beam-to-column connections of four-story SMF

3.3.3 Development of Lateral Drift Protocol

Eleven ground motions listed in Table 3-1 are selected from the Far-Field record set in FEMA P695 (2009) and scaled up until they induce collapse of the SMF. The definition of different collapse modes (sidesway collapse and vertical progressive collapse) and criteria used to detect them will be detailed in Section 4.5.2. For the TGL2 situation, nine of eleven ground motions induce sidesway collapse of the SMF as shown in Figure 3-4(a). The corresponding first-story drift histories for these nine records are plotted in Figure 3-5(a) and are used to develop a representative protocol for sidesway collapse. As seen in Figure 3-5(a), the drift histories have initial cyclic response followed by ratcheting behavior, where the frame keeps leaning farther and farther until it collapses. A loading protocol that is deemed to reflect this behavior is shown as a solid dark line in Figure 3-5(a). It starts with a group of symmetric cycles followed by generally increasing drift

that incorporates three groups of ratcheting loading cycles. The symmetric group has six cycles with increasing magnitudes, while each ratcheting group consists of two small and one large reversed loading cycles. This protocol is designated CR (cyclic ratcheting) protocol.

In the TGL3 situation, the higher initial gravity load increases the possibility of vertical progressive collapse. Of the 11 applied histories, seven ground motions induce vertical progressive collapse of the SMF as they are scaled up. A typical collapse response is shown in Figure 3-4(b). As with sidesway collapse, the drift histories also show initial symmetric cycles followed by ratcheting behvior. The main difference is that the drift does not increase as sharply as in TGL2. Collapse occurs at smaller drift levels, in the range of 2% to 6% rather than about 10% for TGL2, as shown in Figure 3-5(b). The selected drift history deemed to represent the observed histories is shown as a solid dark line in Figure 3-5(b). The selected protocol has the same number of cycles and reversed loadings as the CR protocol but with larger amplitudes. It is designated CR2.

The CR and CR2 protocols represent realistic drift demands imposed by a ground motion on a first-story column in a collapsing structural system. These loading protocols are used, along with others, to investigate the inelastic behavior of axially loaded columns undergoing lateral drift.

Table 3-1. Ground motion records employed in the frame collapse analysis

No.	Event	Station	Component
1	Northridge, 1994	Beverly Hills - Mulhol	9
2	Northridge, 1994	Canyon Country - WLC	0
3	Duzce, 1999	Bolu	0
4	Hector Mine, 1999	Hector	0
5	Imperial Valley, 1979	Delta	262
6	Imperial Valley, 1979	El Centro Array #11	140
7	Kobe, 1995	Nishi-Akashi	0
8	Kobe, 1995	Shin-Osaka	0
9	Kocaeli, 1999	Duzce	180
10	Kocaeli, 1999	Arcelik	0
11	Landers, 1992	Yermo Fire Station	270

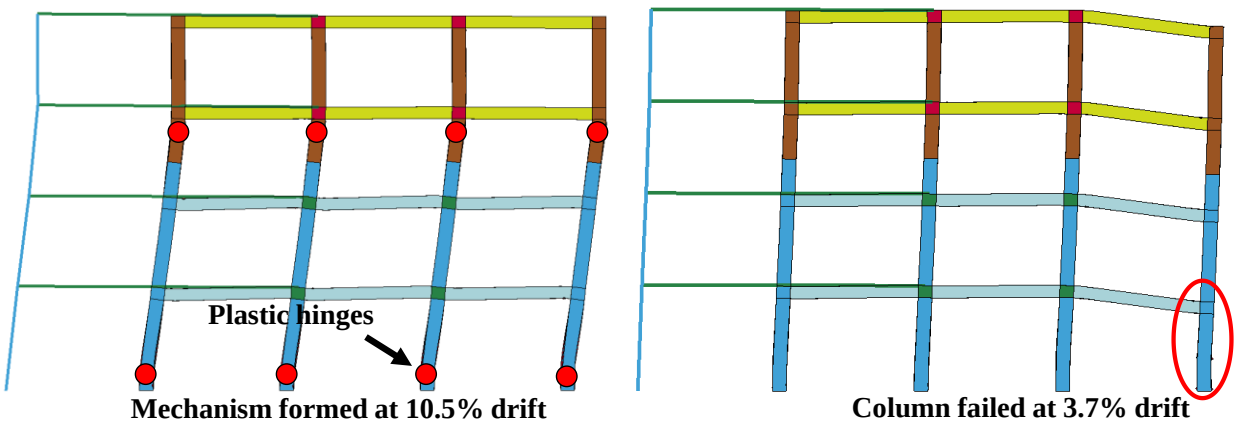

(a) (b)

Figure 3-4. (a) Sidesway collapse of TGL2 frame subjected to Northr/MUL009 record with S_a(1.67s, 5%)=1.61g; and (b) vertical progressive collapse of TGL3 frame subjected to Northr/MUL009 record with S_a(1.67s, 5%)=1.19g

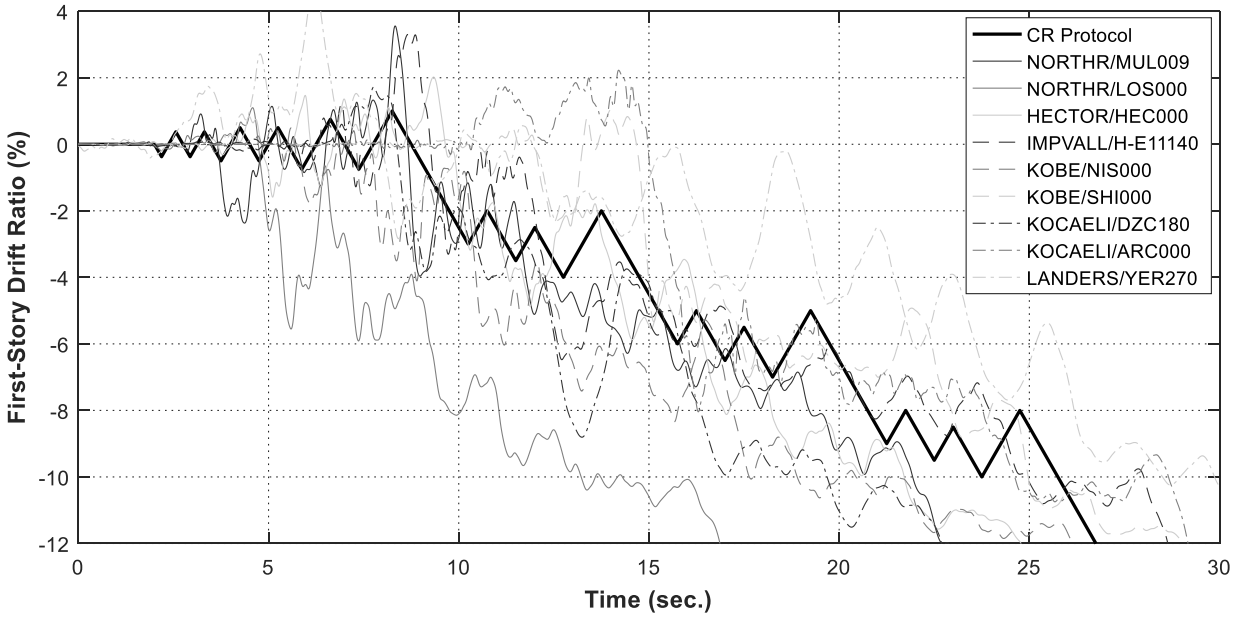

(a)

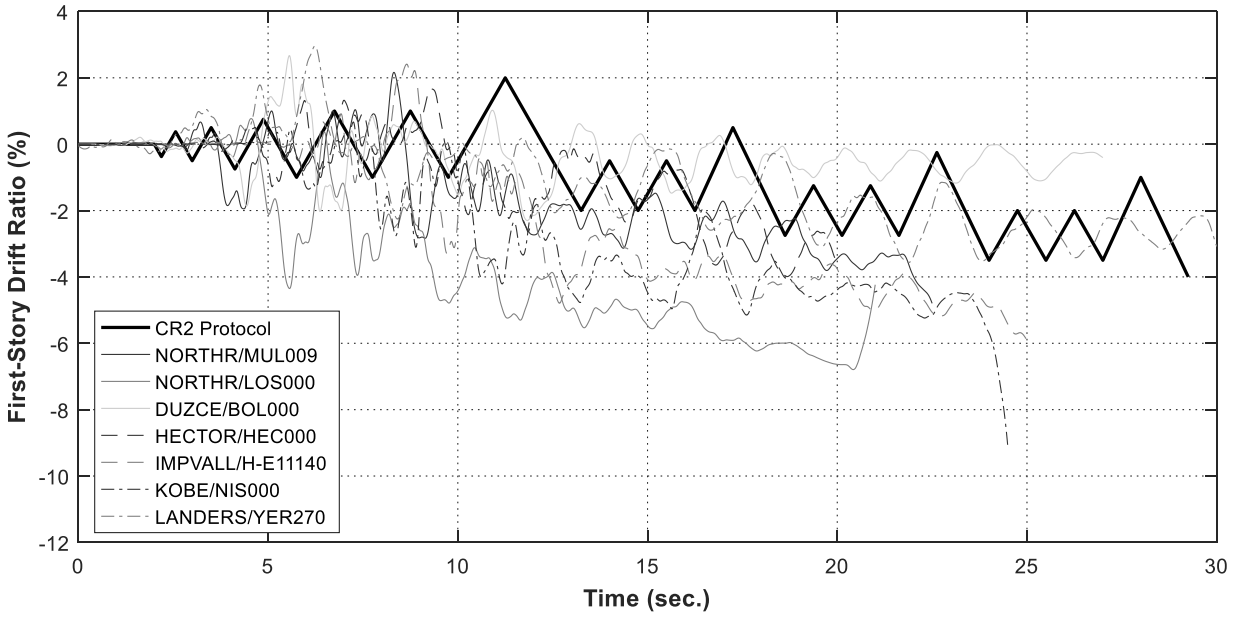

(b)

Figure 3-5. (a) First-story drift history of TGL2 frame undergoing sidesway collapse; and (b) first-story drift history of TGL3 frame undergoing vertical progressive mechanism

3.4 Analysis of Component Column Models

Conducting parametric simulations with the full SMF to study the collapse behavior of steel columns is computationally intractable. Therefore, component column models are used instead. To ensure that the component models yield results that are close to the system results, a series of parametric simulations are conducted to identify the most realistic boundary conditions and drift loading histories for the component model.

3.4.1. Component Model Setup

The column length is taken as 3.96 m, which is the same as the clear floor height of the prototype moment frames. Initial column imperfection is considered by applying a geometric perturbation with an out-of-plane sinusoidal shape. The maximum deflection of the imperfection at mid-height of the columns is $L/1000$, which corresponds to the maximum out-of-straightness tolerance per AISC (2016c).

Interior columns do not see large variations in axial loading while exterior columns are subjected to significant fluctuations in the axial load level during seismic events. The axial loading on exterior column members increases greatly at higher drift levels as a result of the overturning moments on the system. To approximate these effects and enable practical treatment of the problem using component models, interior columns are assumed to carry a constant gravity load, P_g, during their entire drift history. Exterior columns are also assumed to carry a constant gravity load during their drift history but are further compressed at peak drift in one direction to reflect the increase in load demands on exterior columns. The constant compressive axial load in both cases is $P_g = 0.2P_y$, which is the axial load threshold at which unsatisfactory column behavior starts

to occur as noted in Fogarty and El-Tawil (2015), Elkady and Lignos (2015a), and Ozkula et al. (2017b).

The bottom end of the prototype column is assumed to be fully fixed. For the top end, three boundary conditions are explored, as shown in Figure 3-6(a): (1) both in-plane and out-of-plane rotations are fixed (fixed-fixed, FF), (2) in-plane rotation is fixed, while out-of-plane rotation is allowed (fixed-pinned, FP), and (3) in-plane rotation is restrained by an elastoplastic spring with a flexural stiffness, yield moment and hardening post-yield response obtained from subassembly analysis, while out-of-plane rotation is fixed (spring-fixed, SF). The FF condition is similar to that used by Ozkula et al. (2017b) in their experiments. The FP was used by Fogarty et al. (2017) in their computational studies, while the SF condition is newly used in this study to capture the nonlinear, partial rigidity of adjacent beam-column connections.

The subassembly used to determine the properties of the elastoplastic spring is taken from the frame at the inflection points of the beams and columns as shown in Figure 3-6(b). A small push load is first applied at the tip of the second-story column to determine the flexural stiffness of the spring using the moment and rotation measured at the top end of the first-story column (see Figure 3-6b). The push load is then increased until plastic hinges form in the beams. The corresponding moment at the column top end is taken as the yield moment of the spring. The flexural stiffness and yield moment obtained from the subassembly are obtained for interior columns that are W24×103. When other member sections are used, the values are linearly modified based on their flexural stiffness and plastic modulus, respectively. For exterior columns, the flexural stiffness and yield moment are halved to reflect the fact that only one beam is connected to the columns.

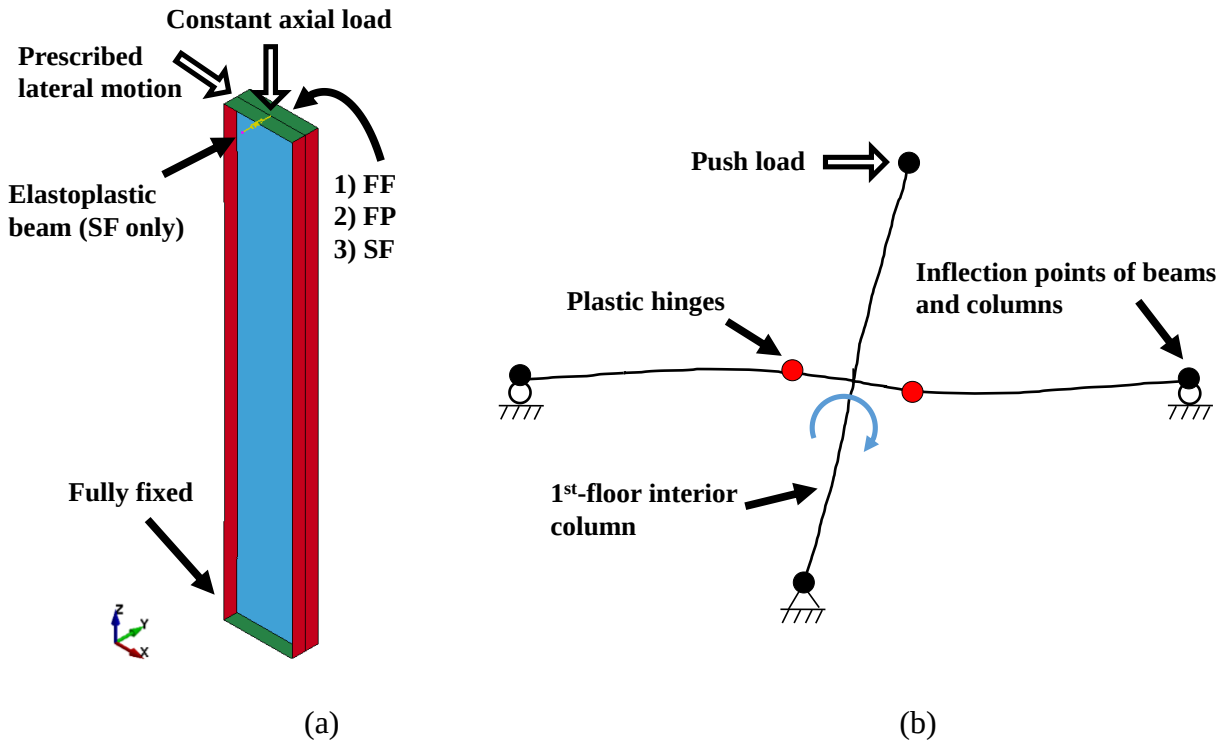

Figure 3-6. (a) Finite element models of individual deep columns; and (b) subassembly analysis for determining properties of elastoplastic spring

In addition to the CR and CR2 loading protocols, two other protocols are used, monotonic (designated M), and symmetric cyclic (designated SC). The former was used in the computational studies of Fogarty et al. (2017), while the latter was used in the experimental research by Ozkula et al. (2017b). The four loading schemes used in this work are shown in Figure 3-7, where the drift level is plotted versus time on the horizontal axis. The loading speeds (and hence times on the horizontal axis of Figure 3-7) are selected through a trial and error process to be low enough so as not to excite unwarranted dynamic effects and yet fast enough to permit the simulations to be conducted in a timely manner.

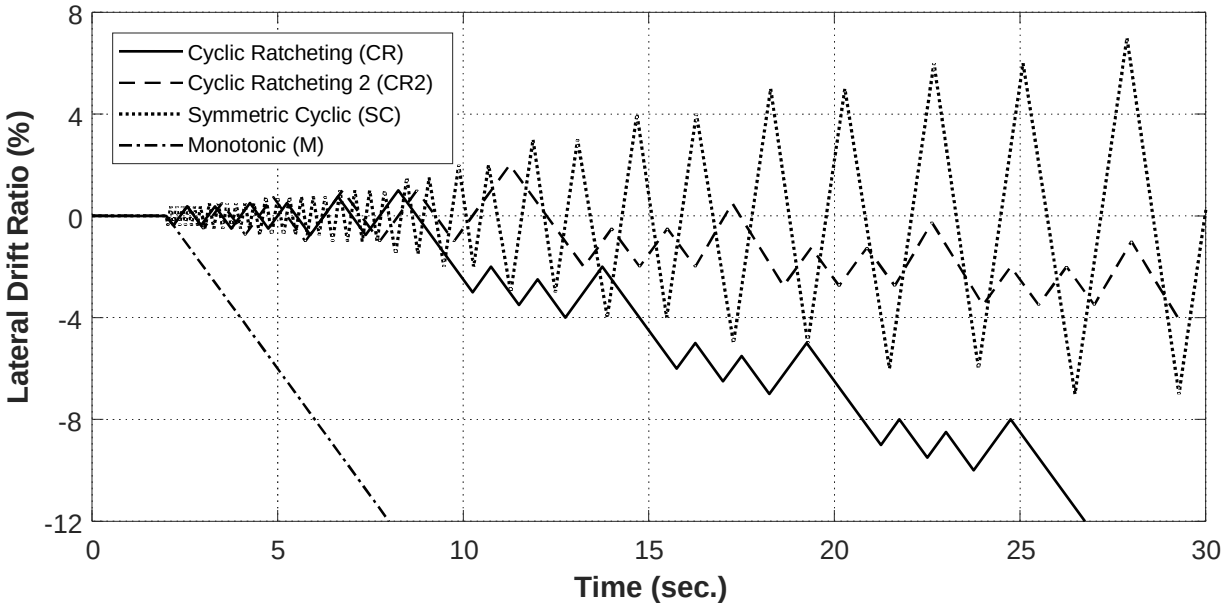

Figure 3-7. Employed lateral drift loading protocols

Collapse is deemed to occur when a column is unable to sustain the applied axial load (explicit collapse) due to instability, i.e. the column unloads and the axial force in it drops suddenly (Fogarty and El-Tawil 2015). The maximum drift ratio (DR_{max}) achieved prior to axial failure is then recorded and taken as the drift capacity of the column.

In order to facilitate discussion of the research parameters, columns under specific loading schemes are designated as W-X-Y, where "W" is the section, "X" is the boundary condition, "Y" is the drift loading protocol. For example, W24×103-FP-CR is the W24×103 column with FP boundary conditions subjected to CR loading.

3.4.2. Effect of Boundary Conditions

Collapse simulations are conducted for a variety of component models with W24 sections. The results of the simulations indicate that the performance of FP columns is substantially worse than columns with other boundary conditions, as shown in Figure 3-8(a), which plots DR_{max} versus

section weight for various boundary conditions. The reason for the poorer performance under FP conditions is that FP columns are more sensitive to changes in the end restraints of the member, which are affected by accumulation of local buckling at the column ends as a result of large drift loading. The evolving local damage leads to stiffness and strength degradation of the effective boundary conditions at the column ends, essentially increasing the effective buckling length and hence lowering the axial strength of the column. At the other extreme, columns with SF conditions generally have the highest drift capacities. The improved performance stems from the flexibility of in-plane rotation at the top end of the columns, which reduces the demand at the top end and delays local buckling.

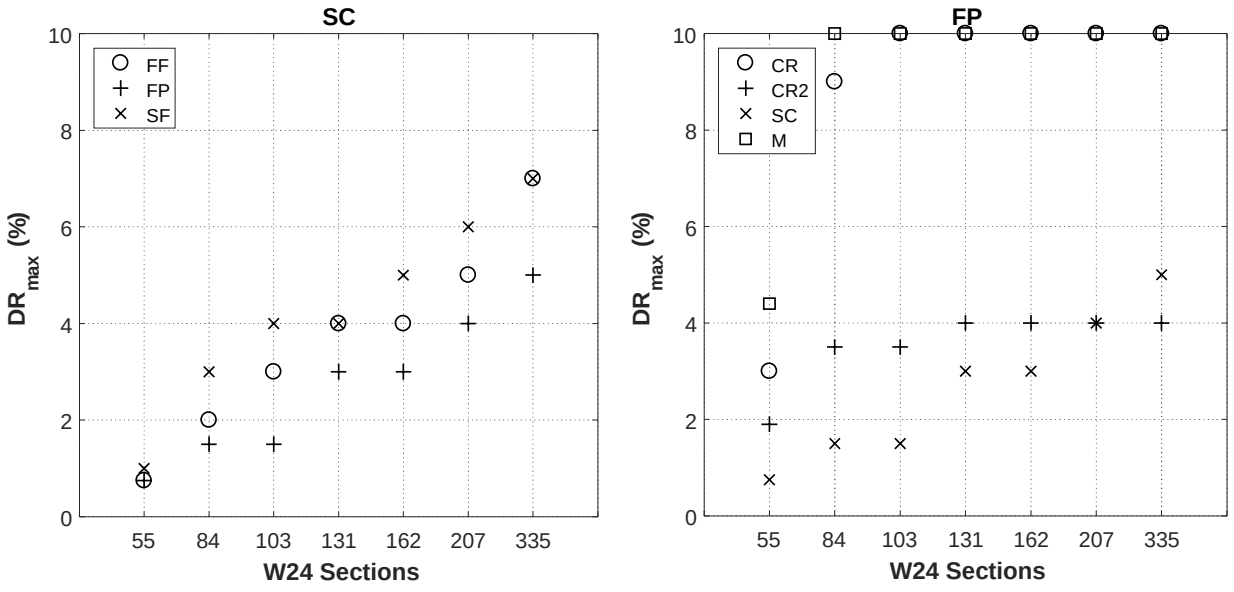

(a) (b)

Figure 3-8. Maximum achieved drift ratios (DR_{max}) of columns with (a) different boundary conditions under SC protocol; and (b) different loading protocols under FP boundary condition

3.4.3. Effect of Loading Protocols

Figure 3-8(b) shows the effects of loading protocol on the drift capacity of columns with FP boundary conditions. It shows that most of the columns subjected to M and CR loading can sustain the applied axial loads up to 10% drift ratio. While some light columns failed before reaching their end point of 4% drift under the CR2 protocol, e.g. DR_{max} of W24×84-FP-CR2 is 3.5%, several heavier columns survived without collapse to 4% drift under this protocol. However, unlike the other protocols, the SC protocol significantly decreases drift capacity. Indeed, most of the columns cannot reach 4% drift under the SC protocol. For example, DR_{max} of W24×84-FP-SC is only 1.5%.

The simulation results, including those in Figure 3-8(b), show that the damage due to the SC protocol is more severe than that due to other schemes. The reasons for this can be better appreciated in Figure 3-9, which shows the force versus drift performance and local buckling at 4% drift of the W24×103-SF column under different drift protocols. As marked by the red circles in Figure 3-9, the column's lateral strength at 4% drift under the SC protocol is only 43% and 36% of that under the CR2 and M protocols, respectively. The explanation for these observations stems from the amount of local buckling in the plastic hinge regions associated with the various loading schemes, which can be seen in the buckled shapes that correspond to the marked circles. The SC protocol tends to cause substantial local buckling at the column ends (Figure 3-9c), which reduces the end restraint and promotes global instability. M loading causes local buckling on only one side of the column end (compression side, see Figure 3-9d), limiting the amount of degradation in the boundary restraints and allowing the columns to reach larger drifts than their SC counterparts. A similar phenomenon (compared to M loading) can also be observed at the ends of columns under the CR and CR2 protocols as shown in Figure 3-9(a) and Figure 3-9(b), respectively. The columns under the CR2 protocol experienced more severe local buckling on both sides of the column than

under the CR protocol, providing explanation for why the CR2 protocol is more damaging than the CR one.

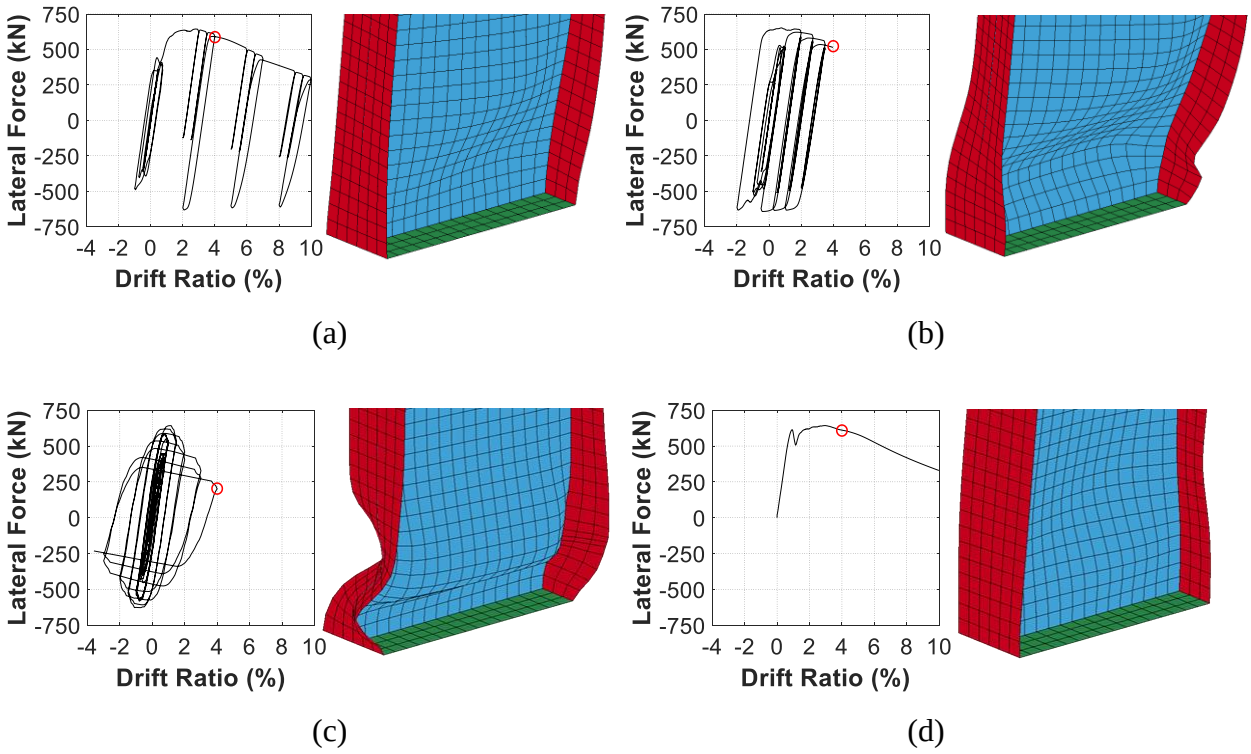

Figure 3-9. Responses of W24x103 SF columns under different loading protocols and corresponding local buckling shapes at 4% drift marked by circles: (a) CR; (b) CR2; (c) SC; and (d) M. Displacement scale factor is 3.0

3.4.4. Comparison between Column and Frame Analysis

Figure 3-10(a) shows the deformed shape of an interior W24×103 column at 4% drift in the four-story frame with TGL3 conditions. The frame is subjected to the Kobe/SHI000 record with S_a(1.67s, 5%)=0.36g and undergoes sidesway collapses. Figure 3-10(b) through Figure 3-10(d) show the response of individual columns at 4% drift for a variety of boundary and loading conditions, namely for W24×103-SF-CR, W24×103-FF-SC, and W24×103-FP-M, respectively. Figure 3-11 also shows the comparison of hysteresis responses between columns. Clearly, the

W24×103-SF-CR case matches the column in the frame well in terms of both deformed shape (Figure 3-10(b) versus Figure 3-10(a)) and hysteresis responses and therefore has an appropriate combination of boundary and loading conditions for simulating an interior column in a sidesway collapse scenario.

Figure 3-12(a) and Figure 3-12(c) show the deformed shape of interior and exterior columns (both W24×103), respectively, at 4% drift in the four-story frame with TGL3 condition, undergoing vertical progressive collapse. The frame is subjected to the Northr/MUL009 with a S_a(1.67s, 5%) of 1.19g. The deformed shape of W24×103-SF-CR2 is shown in Figure 3-12(b), which is reasonably consistent with the shape in Figure 3-12(a). The same is true for the exterior column in Figure 3-12(c) and its individual column comparison in Figure 3-12(d). Although the failure shapes for the exterior column (compare Figure 3-12c to Figure 3-12d) do not relate as well as they do for interior columns, the squash strength of the individual column is $0.53P_y$, which is close to the maximum axial force of $0.49P_y$ seen in the frame's exterior column during the earthquake.

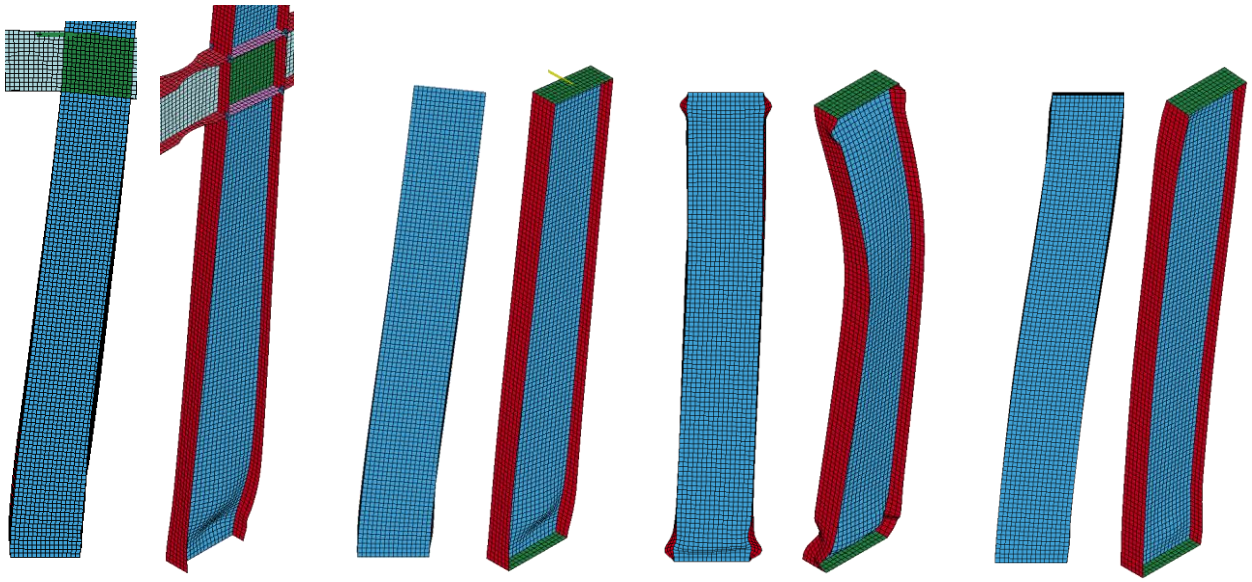

(a) (b) (c) (d)

Figure 3-10. Comparison between deformed shape of columns at 4% drift: (a) interior column (W24×103) in TGL3 frame undergoing sidesway collapse; (b) W24×103-SF-CR; (c) W24×103-FF-SC; and (d) W24×103-FP-M. Displacement scale factor is 3.0

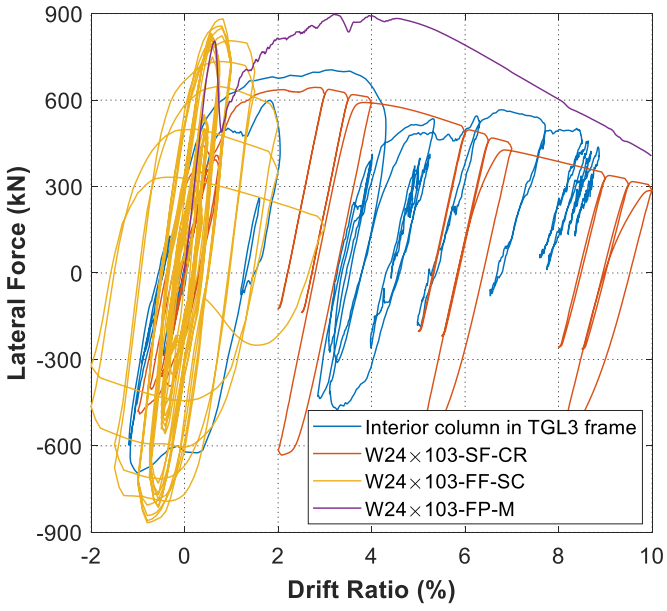

Figure 3-11. Comparison between hysteresis responses of an interior column (W24×103) in TGL3 frame and columns with different boundary and loading conditions

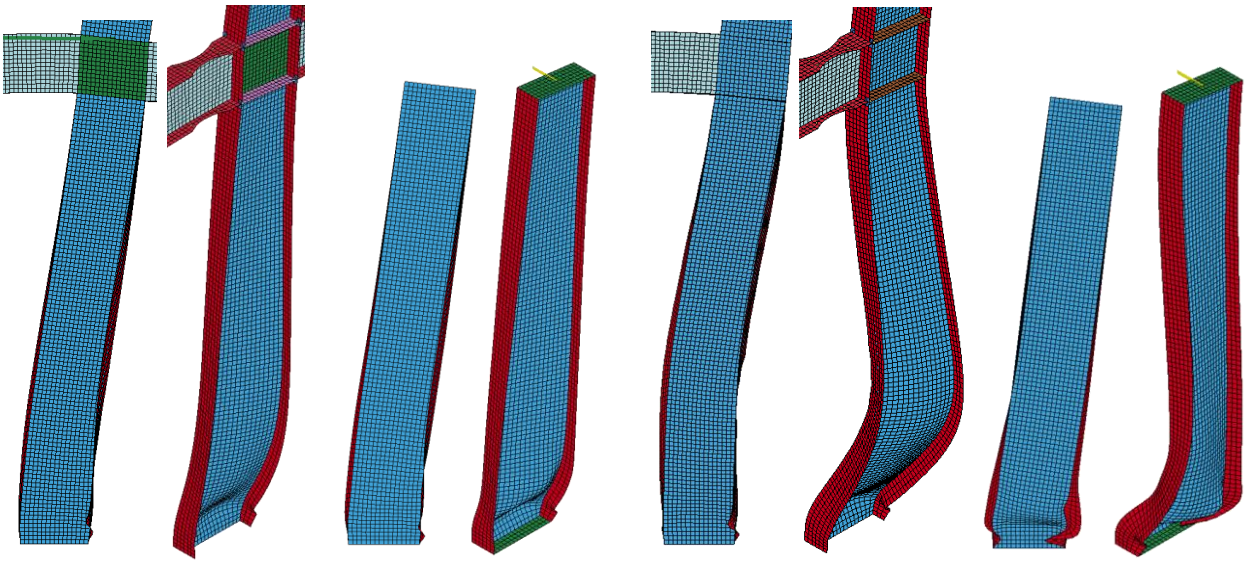

(a) (b) (c) (d)

Figure 3-12. Comparison between deformed shape of columns at 4% drift (a) interior column (W24×103) in TGL3 frame undergoing vertical progressive collapse; (b) W24×103-SF-CR2; (c) exterior column (W24×103) in TGL3 frame undergoing vertical progressive collapse; and (d) W24×103-SF-CR2 with halved spring properties. Displacement scale factor is 3.0

3.4.5. Implications of Component Column Study

The computational results demonstrate that the SF boundary condition is the most realistic one among the various combinations considered. When applied to an individual column, both the CR and CR2 protocols reasonably represent the demands seen at the system level. In the remainder of this chapter, SF boundary conditions are applied in conjunction with the CR2 protocol, which represents a severe design situation, to investigate the effect of section properties on column collapse capacity and develop proposed design guidelines.

3.5 Parametric Study of Section Properties

A set of deep columns that cover a wide range of both global and element slenderness ratios are analyzed using component column models. The selected sections and their properties are listed in Table 3-2 and cover a broad range of slenderness parameters as shown in Figure 3-13. The seismic slenderness limits specified in AISC (2016b) for highly ductile members (λ_{hd}) made of A992 steel (with an expected yield stress ratio R_y = 1.1) are also plotted. The highly ductile limit (λ_{hd}) for flange slenderness ratio ($b/2t_f$) and web slenderness ratio (h/t_w) are listed in Table 2-2.

Table 3-2. Global and element slenderness ratios of prototype columns in parametric study of section properties

Section (in. × lb/ft)	$b/2t_f$	h/t_w	L/r_y	CCALR	PDSR		
					P_g/P_y = 0.2	P_g/P_y = 0.3	P_g/P_y = 0.4
W24×55	6.94	54.6	116.4	0.20	-[a]	-[a]	-[a]
W24×76	6.61	49.0	81.3	0.30	0.57	-[a]	-[a]
W24×84	5.86	45.9	80.0	0.30	0.63	0.47	-[a]
W24×103	4.59	39.2	78.4	0.30	0.68	0.53	-[a]
W24×131	6.70	35.6	52.5	0.40	0.84	0.67	0.50
W24×162	5.31	30.6	51.1	0.45	0.93	0.83	0.68
W24×207	4.14	24.8	50.6	0.45	0.97	0.90	0.78
W24×335	2.73	15.6	48.3	0.55	1.00	1.00	0.92
W27×102	6.03	47.1	78.1	0.25	0.54	0.30	-[a]
W27×114	5.41	42.5	77.1	0.30	0.62	0.36	-[a]
W27×161	6.49	36.1	52.0	0.35	0.79	0.66	0.45
W27×217	4.71	28.7	50.6	0.45	0.90	0.88	0.66
W27×368	2.96	17.3	48.3	0.50	1.00	0.98	0.88
W30×108	6.89	49.6	83.7	0.20	0.47	-[a]	-[a]
W30×148	4.44	41.6	78.9	0.30	0.62	0.35	-[a]
W30×235	5.02	32.2	51.3	0.45	0.83	0.82	0.59
W30×357	3.45	21.6	49.6	0.45	1.00	0.94	0.85

[a]Not available because the column did not reach 4% drift under the applied P_g/P_y.

Because $b/2t_f$ has been shown to have a minor effect on column collapse capacity when it satisfies the current AISC highly ductile limit (Fogarty and El-Tawil 2015), all the selected sections have a $b/2t_f$ below this limit to investigate the more significant factors, h/t_w and L/r_y, as shown in Figure 3-13. The prototype columns are created using the selected W24, W27, and W30 sections with base lengths of 3.96, 4.27, and 4.57 m, respectively. More analysis cases are created by increasing these lengths in order to cover a wide range of L/r_y resulting in a total of 65 column models. The slenderness properties of these columns as well as the highly ductile limits for h/t_w are shown in Figure 3-13(b). Because there is no highly ductile limit for L/r_y of columns in AISC (2016b), the limit for a column with an unbraced beam-to-column connection, which is 60, is plotted instead.

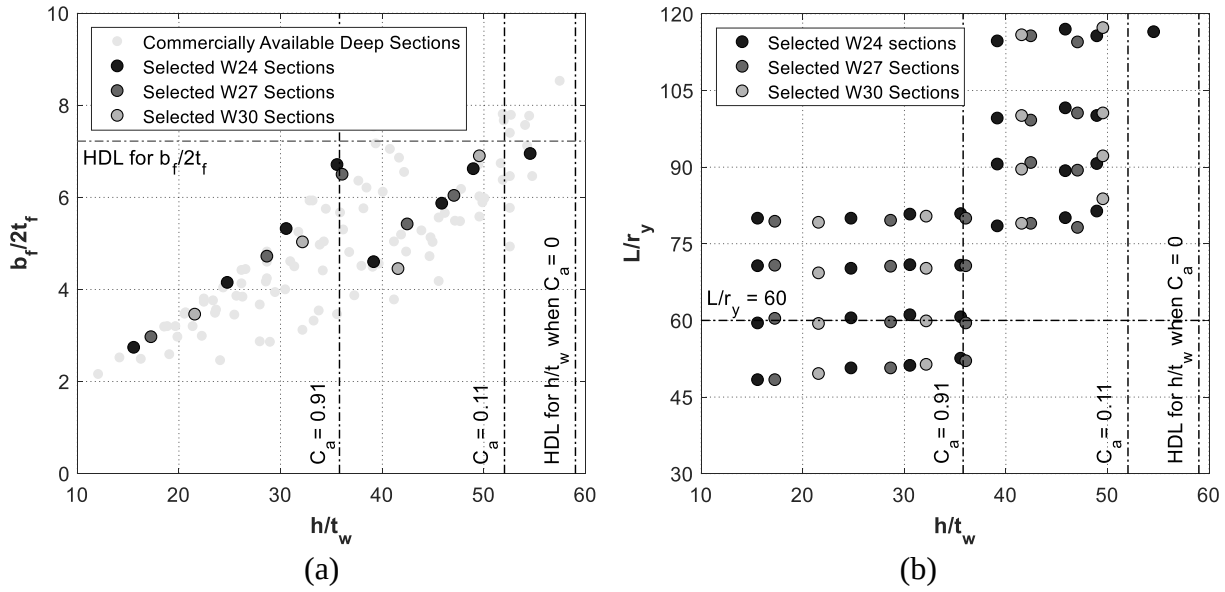

Figure 3-13. Slenderness ratios of selected sections and commercially available deep, wide flange sections made of A992 steel: (a) h/t_w versus $b/2t_f$; and (b) h/t_w versus L/r_y

3.5.1. Performance Parameters

Two performance parameters are considered. The first one is the critical constant axial load ratio (CCALR). The critical constant axial load is defined as the maximum constant axial load ratio

(P_g/P_y) that a column can sustain and still reach 4% drift under a prescribed protocol, as shown in Figure 3-14(a). Due to a compromise between precision and computational cost, the CCALR is determined in 0.05 increments. As noted earlier, interior columns do not see large variations in their axial load demands during a seismic event, therefore CCALR is representative of the collapse capacity of an interior column in a SMF.

The second performance parameter is the post-drift strength ratio (PDSR). The PDSR is defined as the squash capacity of a column at 4% drift after being subjected to a prescribed drift protocol under a given constant axial load (Figure 3-14(b)). The PDSR is the ratio of post-drift strength of the column to P_y and, per the earlier discussion of exterior column behavior, is considered to be an indicator of the collapse capacity of an exterior column in a SMF.

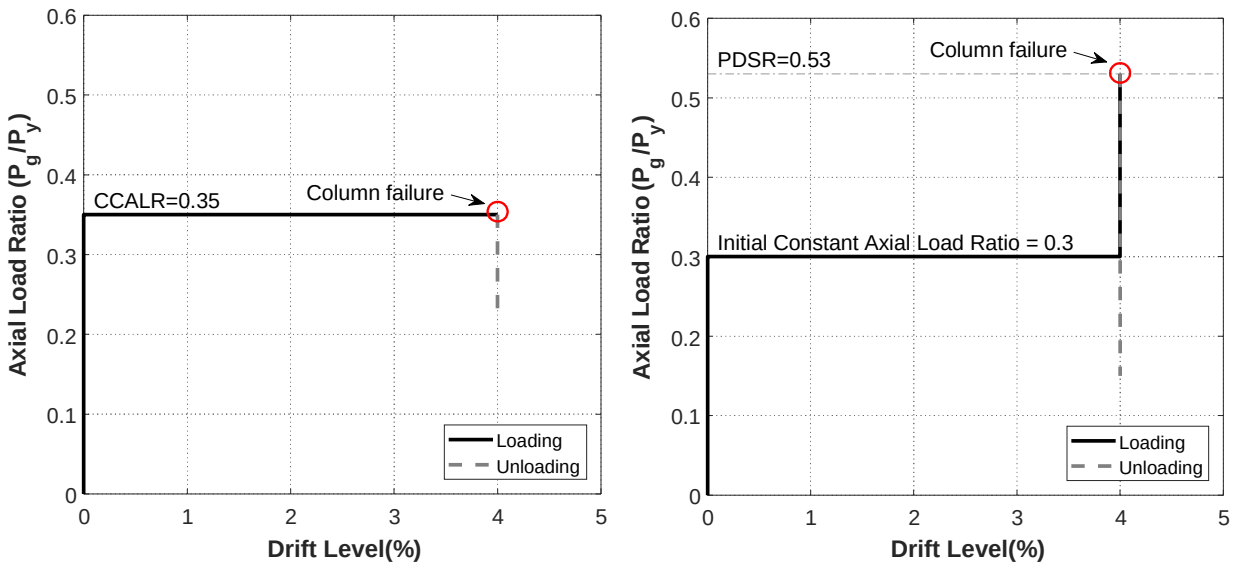

(a) (b)

Figure 3-14. Definition of performance parameters (a) CCALR and (b) PDSR

3.5.2. Influence of Key Variables on Column Behavior

The CCALRs and PDSRs of the prototype columns are shown in Table 3-2 as well as Figure 3-15 and Figure 3-16, respectively. Linear regression analysis is used to tie the CCALR and PDSR values to the web and global slenderness ratios and level of initial axial load. For CCALR, the significant parameters are h/t_w and L/r_y and the predictive function obtained from regression is:

$$\text{CCALR} = 0.72 - 0.0044\frac{h}{t_w} - 0.0027\frac{L}{r_y} \qquad (3\text{-}1)$$

for deep columns with $b/2t_f$ satisfying current highly ductile limits (i.e. $0.32\sqrt{E/R_yF_y}$), $15 < h/t_w < 50$, and $45 < L/r_y < 120$. For PDSR, the significant parameters are h/t_w, L/r_y, and P_g/P_y and the predictive function is:

$$\text{PDSR} = 1.71 - 0.011\frac{h}{t_w} - 0.0055\frac{L}{r_y} - \frac{P_g}{P_y} \qquad (3\text{-}2)$$

for deep columns with $b/2t_f$ satisfying current highly ductile limits, $15 < h/t_w < 50$, $45 < L/r_y < 120$, and $0.2 < P_g/P_y < 0.4$. When applying Equation (3-2), P_g/P_y should be smaller than CCALR otherwise the column cannot support P_g/P_y up to 4% drift. To avoid computing CCALR for exterior columns, the values obtained from Equation (3-1) can be used instead even though they were developed for interior columns. CCALR values from Equation (3-1) are conservative because interior columns have larger in-plane rotational restraint at the top compared to exterior columns, which leads to lower column axial capacity and, hence, CCALR. The predictive functions are shown as a contour plot with the data in Figure 3-15 and Figure 3-16.

Figure 3-15 shows that there is a strong inverse relationship between CCALR and both web and global slenderness ratios (h/t_w and L/r_y). For columns with L/r_y about 80, increasing h/t_w from 15

to 50 reduces CCALR from 0.45 to 0.25. For columns with h/t_w about 37, the CCALR decreases from 0.4 to 0.2 when L/r_y increases from 52 to 115. These results show that both h/t_w and L/r_y have a significant effect on the collapse capacity of deep columns.

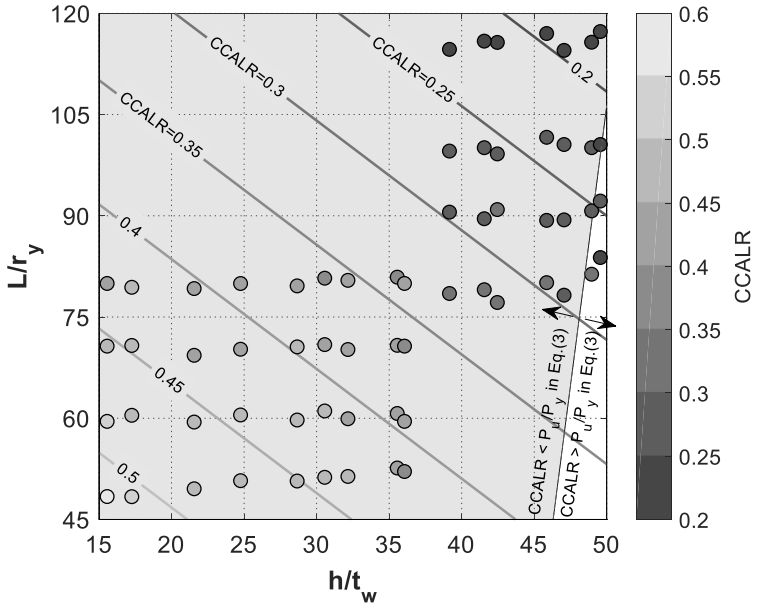

Figure 3-15. Contour plot of predictive function for CCALR

For the resistance factor under compression, ϕ_c, equal to 1.0, the current highly ductile limit for the web is plotted in Figure 3-15 as a sloping dotted line. The line represents the intersection between λ_{hd} and Equations (3-1). In other words, the line represents the condition $P_g = P_u$, which implies that CCALR = P_u/P_y. For example, when P_u/P_y = 0.25, the current highly ductile limit for h/t_w is 49.1. By substituting h/t_w = 49.1 and CCALR = 0.25 into Equation (3-1), we can get L/r_y = 94.0, which is a point (49.1, 94.0) on the sloping dotted line. The shaded region above the line therefore represents sections that do not satisfy highly ductile behavior, meaning that their CCALR is less than P_u/P_y. Clearly most of the considered cases are in the shaded area suggesting that current highly ductile limits cannot guarantee that deep columns with a constant axial load can

always reach 4% drift without failure. One of the reasons for this discrepancy is that current provisions do not consider the adverse interactions that occur between L/r_y and h/t_w.

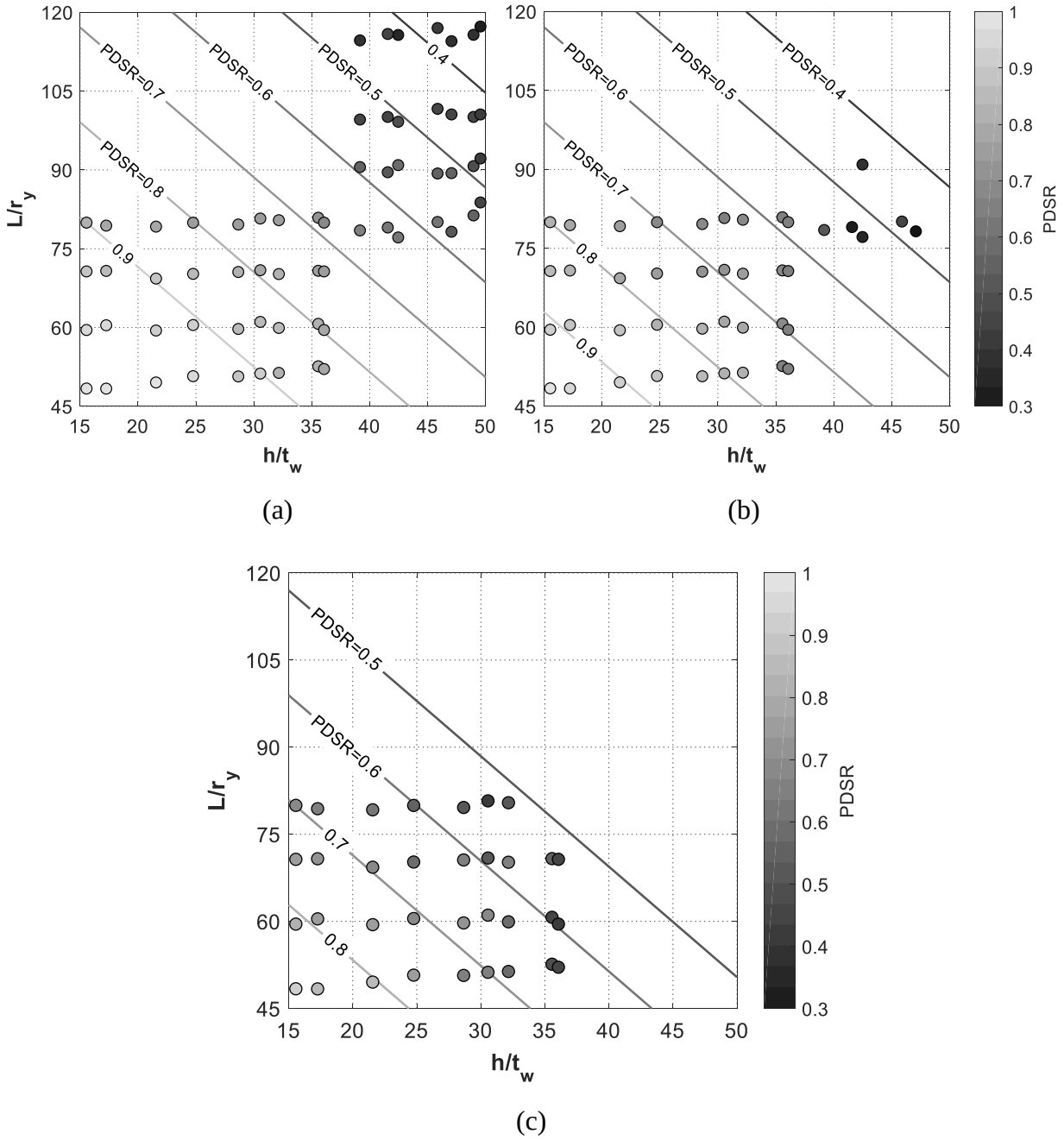

Figure 3-16. Contour plot of predictive function for PDSR when initial constant axial load ratio P_g/P_y = (a) 0.2; (b) 0.3; and (c) 0.4

Figure 3-16 shows the PDSR of each column subjected to different levels of an initial, constant axial load ratio P_g/P_y. It is clear that increasing h/t_w, L/r_y, or P_g/P_y all have a negative effect on PDSR. For example, when $P_g/P_y = 0.4$ as shown in Figure 3-16(c), the PDSR of columns with L/r_y about 50 decreases significantly from 0.92 to 0.45 when h/t_w increases from 15.6 to 35.6. Similarly, for W24×335 columns with $h/t_w = 15.6$, increasing L/r_y from 48.3 to 79.9 reduces the PSDR from 0.92 to 0.69.

The simulation data suggests that the effect of P_g/P_y increases the larger it becomes, which means that the difference of PDSR between $P_g/P_y = 0.3$ and 0.4 is larger than the one between $P_g/P_y = 0.2$ and 0.3. For example, for the W24×207 column with $h/t_w = 24.8$ and $L/r_y = 80$, the PDSR decreases from 0.77 to 0.7 when P_g/P_y increases from 0.2 to 0.3, and quickly decreases to 0.49 when P_g/P_y increases to 0.4.

3.5.3. Axial Shortening

It is well documented (Elkady and Lignos 2015a, 2017; Fogarty et al. 2017; Ozkula et al. 2017b) that axially loaded deep columns subjected to cyclic lateral drift shorten due to flange and web local buckling. Figure 3-17 shows the evolution of axial shortening for a range of W24 prototype columns with $P_g/P_y = 0.2$ and 0.4. The amount of axial shortening in Figure 3-17 is computed when the columns first reach drift levels between 0% and 4% and then normalized by column length (3.96 m). Also plotted are recent experimental results from Elkady and Lignos (2017). Figure 3-17 shows data from specimens C5 (W24×146) and C8 (W24×84), both of which are subjected to a constant axial load of $0.2P_y$ combined with a collapse-consistent lateral loading protocol as defined by Elkady and Lignos (2017). The axial shortening plotted corresponds to that achieved when the columns first reach 1%, 2%, 3% and 4% drift levels. Clearly, the experimental

data is consistent with the computational one, providing yet more confidence in the validity of the computational scheme.

Two trends are clear from Figure 3-17: (1) the amount of axial shortening depends greatly on the level of axial load (the curves for P_g/P_y = 0.4 are higher than those for P_g/P_y = 0.2); (2) the rate of growth of shortening is faster at the higher axial load level. Another key observation from Figure 3-17 is that the amount of shortening is small at 1% drift, which is commonly associated with the immediate occupancy performance objective (ASCE 2006). At that level, the axial shortening is 0.1% and 0.3% when P_g/P_y = 0.2 and 0.4, respectively. Even at 2% drift, at which nonstructural damage is anticipated to occur, the amount of axial shortening is still small (substantially than 1% shortening).

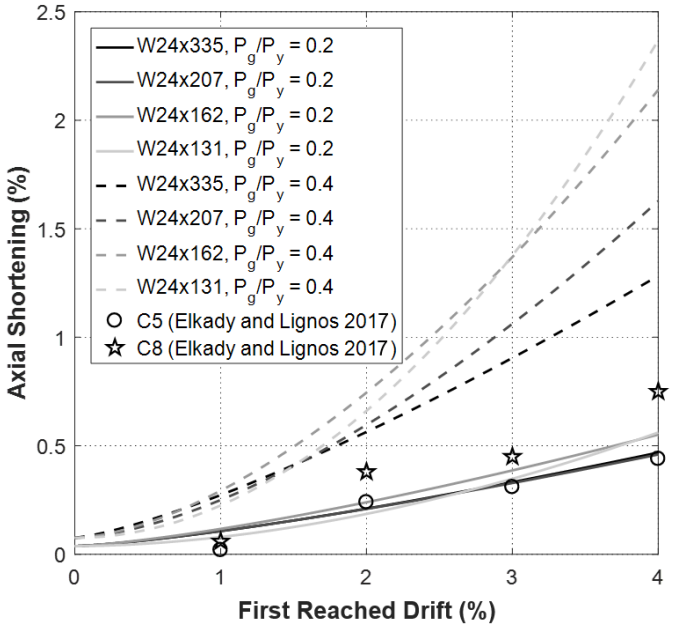

Figure 3-17. Axial shortening evolution of W24 prototype columns subjected to an axial load of 0.2P_y or 0.4P_y

The moment frame employed in this study has a span of 6.1 m and first-story clear height of 3.96 m. A relative axial shortening of 0.3% translates into a relative vertical displacement of 1/500 of the span between the beam's ends. This relative vertical displacement is expected to cause only minor non-structural damage per serviceability requirements in AISC (2016c), if any, especially for performance levels associated with immediate occupancy. At 4% drift, nominally associated with the collapse prevention performance level, axial shortening is substantial, reaching more than 2% in the sections selected for study. However, these columns are still capable of supporting their axial load in accord with the objective of collapse prevention.

3.6 Proposed Design Guidelines

As defined earlier, the CCALR can be interpreted as the maximum axial force that an interior column can support and still reach 4% drift. Assuming that the axial force on interior columns results from gravity loads and remains typically constant during an earthquake, Equation (3-1) can be rewritten as the following inequality:

$$\frac{P_g}{P_y} \leq 0.72 - 0.0044\frac{h}{t_w} - 0.0027\frac{L}{r_y} \qquad (3\text{-}3)$$

where P_g is the gravity-induced axial force. Rearranging Equation (3-3):

$$\frac{h}{t_w} \leq 226(0.72 - \frac{P_g}{P_y}) - 0.62\frac{L}{r_y} \qquad (3\text{-}4)$$

Based on the definition of CCALR, equation (3-4) suggests a way to get the highly ductile limit for h/t_w for interior columns, $\lambda_{hd,in}$. To frame equation (3-4) into a familiar format with the consideration of ϕ_c, it can be approximated and rearranged into the following form:

$$\lambda_{hd,in} = 9.86\sqrt{\frac{E}{R_y F_y}}(0.72 - \frac{P_g}{\emptyset_c P_y}) - 0.62\frac{L}{r_y} \quad (3\text{-}5)$$

for deep columns with $b/2t_f$ satisfying current highly ductile limits, $15 < h/t_w < 50$, and $45 < L/r_y < 120$.

The PDSR can be interpreted as the maximum required strength that an exterior column must resist due to gravity loads and overturning moments. Based on this, Equation (3-2) can be rewritten to derive the relationship between the required axial strength of an exterior column, its section properties and the initial axial force level, i.e. the gravity-induced axial force, P_g:

$$\frac{P_r}{P_y} \leq 1.71 - 0.011\frac{h}{t_w} - 0.0055\frac{L}{r_y} - \frac{P_g}{P_y} \quad (3\text{-}6)$$

where P_r is the required axial compressive strength as determined using the overstrength seismic load combined with the gravity-induced axial force. Rearranging Equation (3-6):

$$\frac{h}{t_w} \leq 95(1.71 - \frac{P_g}{P_y} - \frac{P_r}{P_y}) - 0.53\frac{L}{r_y} \quad (3\text{-}7)$$

which indicates the highly ductile limit for h/t_w for exterior deep columns, $\lambda_{hd,ex}$, and can be approximated and rearranged into the following form with the consideration of ϕ_c:

$$\lambda_{hd,ex} = 4.13\sqrt{\frac{E}{R_y F_y}}(1.71 - \frac{P_g}{\emptyset_c P_y} - \frac{P_r}{\emptyset_c P_y}) - 0.53\frac{L}{r_y} \quad (3\text{-}8)$$

for deep columns with $b/2t_f$ satisfying current highly ductile limits, $15 < h/t_w < 50$, $45 < L/r_y < 120$, and $0.2 < P_g/P_y < 0.4$.

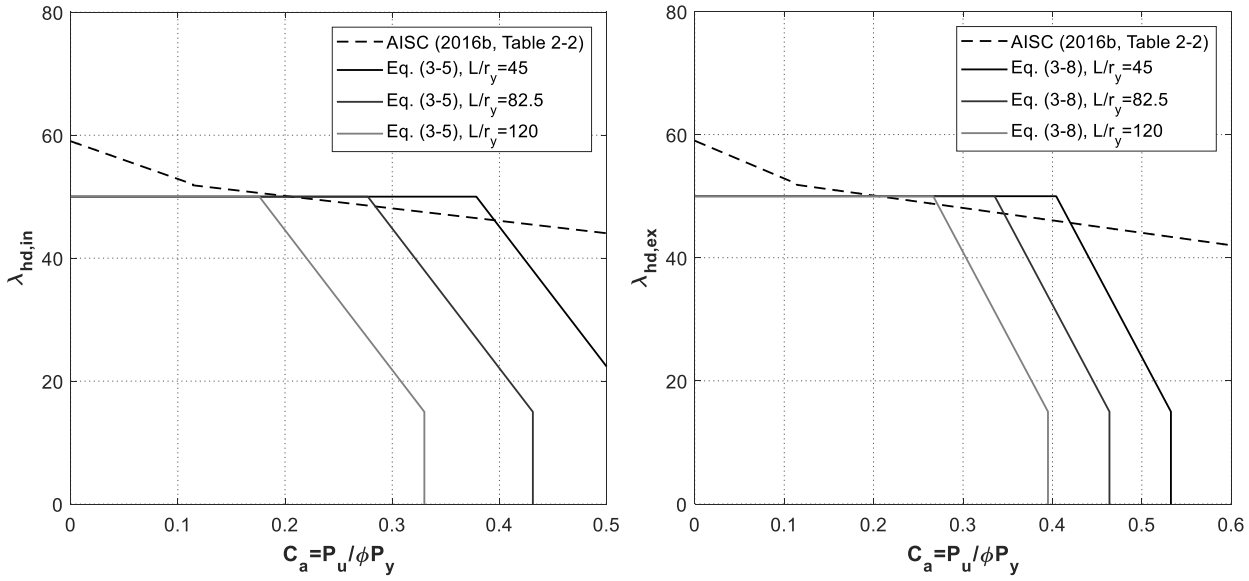

(a) (b)

Figure 3-18. Proposed highly ductile limits for (a) interior columns ($\lambda_{hd,in}$) and (b)exterior columns under P_g/P_y = 0.3 ($\lambda_{hd,ex}$)

The proposed highly ductile limits, i.e. Equation (3-5) and (3-8), are plotted in Figure 3-18 with current limits in AISC seismic provisions, where P_u is P_g and $(2P_g + P_r)/3$ in Figure 3-18(a) and Figure 3-18(b) for interior columns and exterior columns under P_g/P_y = 0.3, respectively. As can be seen, the proposed limits approximately match the current AISC limits for interior columns with $L/r_y < 80$ and $h/t_w = 50$ when $C_a = 0.3$ but penalize columns with larger L/r_y or under higher axial loads. The proposed limits for exterior columns are less stringent than the ones for interior columns as they penalize the exterior columns with $L/r_y > 105$ and $h/t_w = 50$ when $C_a = 0.3$ because of less in-plane rotational restraint at the column top end.

To assess the effectiveness of the proposed equations, two W24, W27, and W30 columns each (not considered in the calibration process) are analyzed using the finite element (FE) models developed earlier and their capacities are compared to the values obtained from the proposed

predictive functions (Equations (3-1) and (3-2) based on which Equations (3-5) and (3-8) are proposed). The properties of these columns and their performance parameters as well as predicted strength values are listed in Table 3-3. As can be seen, the predictive functions give comparable CCALR and PDSR values to the FE results for all columns with differences within 12% showing that the proposed guidelines are reasonably accurate and broad.

Table 3-3. Evaluation of linear predictive functions for CCALR and PDSR

						PDSR					
				CCALR		P_g/P_y = 0.2		P_g/P_y = 0.3		P_g/P_y = 0.4	
Section (in. × lb/ft)	$b/2t_f$	h/t_w	L/r_y	FE	Eq. (3-1)	FE	Eq. (3-2)	FE	Eq. (3-2)	FE	Eq. (3-2)
W24×94	5.18	41.9	93.9	0.25	0.28	0.53	0.54	-------[a]		-------[a]	
W24×146	5.92	33.2	67.8	0.40	0.38	0.82	0.78	0.76	0.68	-------[a]	
W27×94	6.70	49.5	107.5	0.20	0.20	0.43	0.39	-------[a]		-------[a]	
W27×307	3.46	20.6	73.9	0.40	0.42	0.86	0.88	0.81	0.78	0.65	0.68
W30×173	7.04	40.8	66.7	0.35	0.35	0.73	0.71	0.58	0.61	-------[a]	
W30×292	4.12	26.2	55.3	0.45	0.45	0.92	0.92	0.85	0.82	0.77	0.72

[a]Not computed because P_g/P_y is larger than CCALR in Equation (3-1).

3.7 Conclusions

The collapse response of individual deep columns is investigated using a validated computational modeling scheme. To ensure that the loading and boundary conditions applied to the individual column models are realistic, collapse analyses of a four-story SMF are first performed to develop representative loading protocols and boundary conditions for first-story columns in earthquake-induced collapse scenarios, including both sidesway and vertical progressive collapse situations. The effects of the developed loading and boundary conditions on column behavior as compared to those used by others are highlighted and discussed. Using the developed loading protocols and boundary conditions, the collapse behavior of a variety of deep columns that cover a wide range of global and element slenderness ratios is studied. The key variables that influence response are

identified and quantified through a regression analysis. Based on the limits of the parameters studied, the following conclusions can be drawn:

- The first-story drift histories in the system analyses show a cyclic ratcheting behavior, where the frame keeps leaning further and further until it collapses. While this behavior is seen in both sidesway and vertical progressive collapse modes, the overall characteristics of the histories are different. In vertical progressive collapse, the drift history does not increase as quickly as in sidesway collapse and collapse occurs at smaller drift levels, e.g. 2% to 6% versus about 10%.

- The performance of columns with a fix-pinned (FP) top end is substantially worse than columns with other boundary conditions. This behavior is because this particular type of boundary condition has essentially longer out-of-plane effective buckling length and is more prone to accumulation of local buckling at the top end, which reduces the end restraint and further increases the effective buckling length. On the other hands, columns with a spring-fixed (SF) top end generally have the highest drift capacities because they suffer less local buckling at their top ends and hence do not see as rapid a degradation in the top restraint as in their FP counterparts.

- Columns under the symmetric cyclic loading protocol (SC) show much worse drift capacity than other loading protocols. The lateral strength of the SC-loaded column at 4% drift was seen to be as low as 40% of that for columns with other loading protocols. The SC protocol tends to cause substantial local buckling at both sides of the column end, significantly degrading the ends restraints and thereby reducing the buckling strength of the columns and hence their axial loading capacity.

- Under the selected loading and boundary conditions, the web slenderness ratio, h/t_w, global slenderness ratio, L/r_y, and initial constant axial load ratio, P_g/P_y all have a significant effect on collapse capacity of deep columns. Generally, the effect of h/t_w on post-drift strength is larger than L/r_y, and the effect of P_g/P_y increases the higher it becomes. The simulation results also clearly show that current highly ductile limits specified in AISC seismic provisions cannot guarantee that deep columns can reach 4% drift without failure.

- Both simulation results and recent experimental results show that the amount of column shortening is minimal for small drifts associated with the immediate occupancy performance level. While column shortening increases significantly at 4% drift and may cause some nonstructural damage, columns still have capacity to support the required axial load in accord with the collapse prevention performance level. Column shortening is therefore a serviceability issue rather than safety concern.

Based on the comprehensive understanding developed in this Chapter, design-oriented expressions are proposed to compute the compressive capacity of deep columns that are highly ductile in the AISC (2016b) sense. The proposed expressions are put into a familiar format to facilitate their adoption into future design provisions. These guidelines were developed using a limited set of sections and parameters. Therefore, additional work is needed to ensure that they are more generally applicable and incorporate appropriate resistance factors.

CHAPTER 4

COLLAPSE RESISTANCE OF STEEL SPECIAL MOMENT FRAMES WITH DEEP COLUMNS

4.1 General

This chapter presents a computational study of seismic collapse of steel special moment frames (SMFs) designed with deep columns. The study considers four- and eight-story prototype frames and their variants to understand three key factors affecting the frame collapse potential: (1) column lateral bracing; (2) level of column gravity load; and (3) column section properties (Section 4.3 and 4.4). High fidelity models of frames are developed to capture local and global instabilities and explicitly represent both sidesway and vertical collapse behaviors (Section 4.5). The simulation results are used to propose improved seismic provisions for collapse capacity of SMFs and investigate the shortening behavior of deep columns at the system level (Section 4.6).

4.2 Motivation

While early studies indicated that the vulnerability of deep steel columns to torsional demands resulting from the formation of adjacent beam plastic hinges were generally unfounded (Chi and Uang 2002; Shen et al. 2002; Zhang and Ricles 2006), more recent studies confirmed that current limits for element slenderness ratio cannot guarantee highly ductile behavior for deep columns, especially when the axial load is larger than $0.2P_y$ (Elkady and Lignos 2015a; Fogarty and El-Tawil 2015; Ozkula et al. 2017b). However, as identified in Section 3.2, this concern may have

been exacerbated by some of the assumptions used in those original studies. For example, Elkady and Lignos (2017), Fogarty et al. (2017), and Wu et al. (2018a) noted that symmetric drift loading, which is commonly used in experimental research involving moment connections and utilized in more recent deep column studies, can be unrealistically severe. Based on an investigation of individual column behavior, Wu et al. (2018a) proposed modified web slenderness ratio limits that consider the effect of axial load and global slenderness ratio(L/r_y) to ensure highly ductile behavior of such members under meaningful drift protocols.

Unlike the member level at which many researchers have conducted studies, there are only a handful of studies that investigated the effects of deep column behavior on overall response of SMF systems. Reyes-Salazar et al. (2014) and Elkady and Lignos (2014, 2015b) conducted system-level studies of SMFs with deep columns. However, they employed beam-column elements to model column response. The elements used could not capture the full range of instabilities that occur in deep columns, especially the formation of local buckling and interactions between local and global buckling. Using detailed finite element models, Wu et al. (2017) explicitly considered the effect of local and global instabilities in deep columns on SMF behavior, but only with a limited set of variables.

The survey above shows that there is insufficient information about how SMFs with deep columns behave under severe seismic loading. The computational study presented in this chapter looks to deepen the understanding of the interaction between column instability and frame collapse and propose improved seismic provisions based on the findings.

4.3 Prototype Frames

This study uses four-story and eight-story SMFs as prototype frames. The four-story one is the same as that used in Chapter 3 to develop the lateral drift protocol for individual columns. Details of the design can be found in NIST (2010) where response spectrum analysis (RSA) was used with seismic design category D_{max} for the same building plan configuration and tributary gravity loads shown in Figure 3-1(a). Perimeter SMFs are assumed to resist all of the seismic loading on the building. The frames are both designed with W24 columns and reduced beam sections (RBS) using ASTM A992 steel per AISC (2005a, 2005b) and ASCE (2005). The beam and column sections used in the four-story and eight-story frames are listed in Figure 4-1. The columns are spliced every two stories.

Although the frames were designed in accordance with 2005 codes, the four-story frame also satisfies the latest specifications, i.e. AISC (2016a, 2016b) and ASCE (2016). On the other hand, the eight-story frame does not fulfill the strong-column/weak-beam requirement in AISC (2016b):

$$\sum Z_c \left(F_{yc} - P_{uc}/A_g\right) / \sum C_{pr} R_y F_{yb} Z_b + M_{uv} > 1.0 \qquad (4\text{-}1)$$

where Z_c and Z_b are the plastic section modulus of columns and beams, respectively, F_{yc} and F_{yb} are the specified minimum yield stress of columns and beams, respectively, P_{uc} is the required compressive strength using LRFD load combinations, C_{pr} is the factor to account for peak connection strength, R_y is the ratio of the expected yield stress to the specified minimum yield stress, and M_v is the additional moment due to shear amplification from the location of the plastic hinge to the column centerline, based on LRFD load combinations. The reason is that, unlike in AISC (2005b), the determination of P_{uc} in AISC (2016b) incorporates the overstrength seismic

load. The inclusion of the overstrength seismic load significantly reduces the moment capacity of the columns. Key properties of the prototype four- and eight-story frames are listed in Table 4-1 (labeled S4-L1-T2-C1 and S8-L1-T2-C2, respectively). The table lists the fundamental period (T_1) along with slenderness properties of the first-story exterior columns.

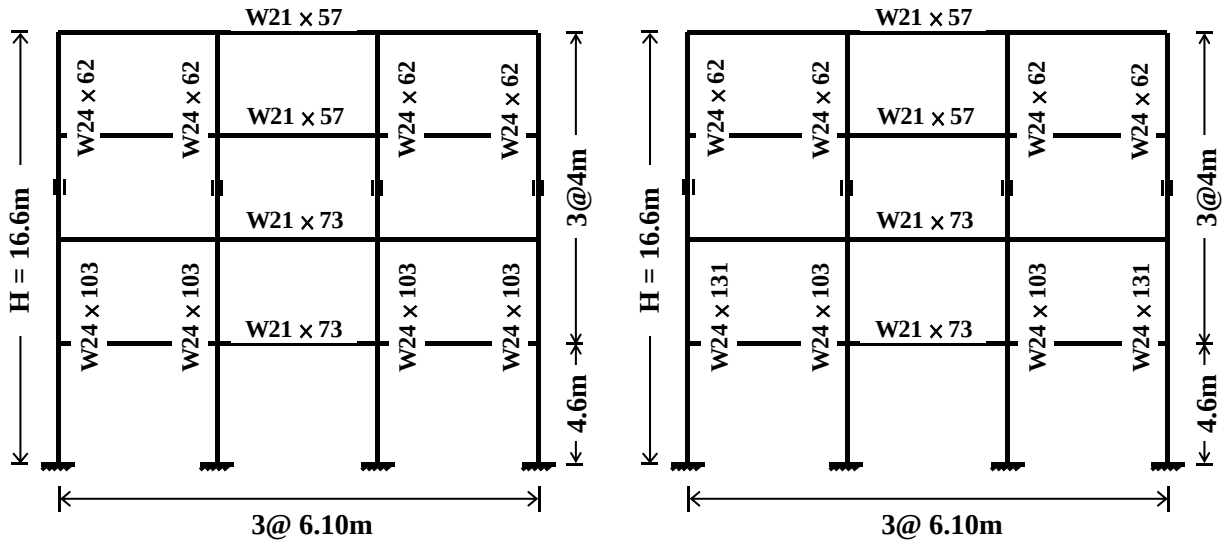

(a) (b)

Figure 4-1. Elevation view of (a) the four-story prototype SMF and (b) the four-story variant SMF (S4-L1-T3-C2)

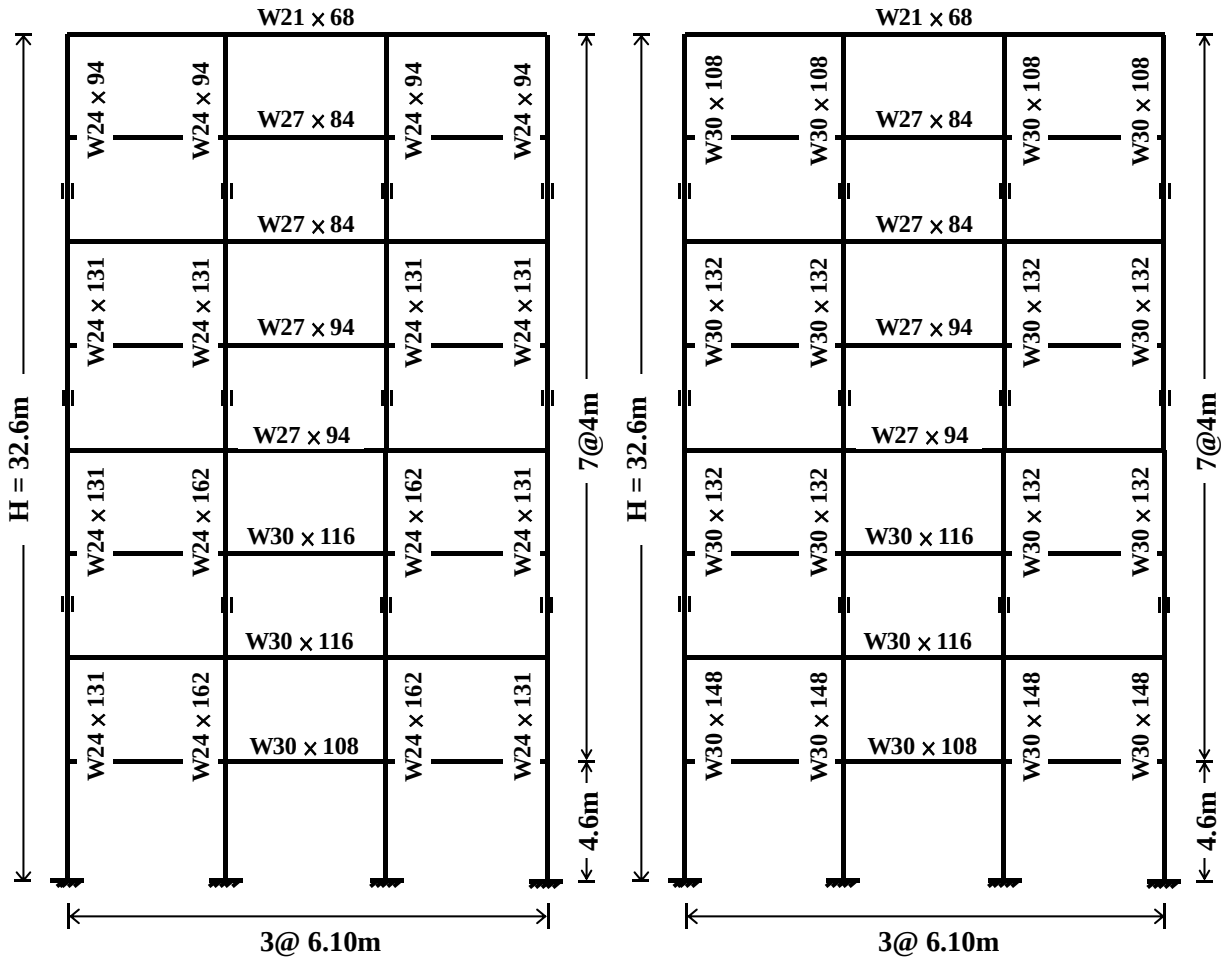

(a) (b)

Figure 4-2. Elevation view of (a) the eight-story prototype SMF and (b) the eight-story variant SMF (S8-L1-T2-C3)

Table 4-1. Properties and collapse analysis results of prototype frames and variants

Frame ID	Lateral Bracing	Gravity Loads	Column Section[a]	h/t_w[a]	L/r_y[a]	P_g/P_y[a]	T_1 (sec.)	$\tilde{S}_{a,C}(T_1, 5\%)$ (g)	$S\tilde{D}R_{max,C}$ (%)	λ_c	# of Records	
											SC[b]	VC[b]
4-story												
S4-L1-T1-C1	LBC1	TGL1	W24×103	39.2	79.8	0.11	1.67	0.68	8.0	4.18e-4	11	0
S4-L1-T2-C1	LBC1	TGL2	W24×103	39.2	79.8	0.18	1.67	0.65	7.5	4.43e-4	10	1
S4-L1-T3-C1	LBC1	TGL3	W24×103	39.2	79.8	0.27	1.67	0.50	4.2	7.02e-4	3	8
S4-L2-T1-C1	LBC2	TGL1	W24×103	39.2	90.5	0.11	1.67	0.68	8.0	4.20e-4	11	0
S4-L2-T2-C1	LBC2	TGL2	W24×103	39.2	90.5	0.18	1.67	0.64	7.0	4.63e-4	9	2
S4-L2-T3-C1	LBC2	TGL3	W24×103	39.2	90.5	0.27	1.67	0.42	3.0	9.99e-4	0	11
S4-L3-T1-C1	LBC3	TGL1	W24×103	39.2	19.9	0.11	1.67	0.70	8.2	3.87e-4	11	0
S4-L3-T2-C1	LBC3	TGL2	W24×103	39.2	19.9	0.18	1.67	0.67	7.7	4.12e-4	11	0
S4-L3-T3-C1	LBC3	TGL3	W24×103	39.2	19.9	0.27	1.67	0.62	7.3	4.83e-4	10	1
S4-L1-T3-C2	LBC1	TGL3	W24×131	35.6	53.5	0.21	1.64	0.67	7.4	4.09e-4	10	1
8-story												
S8-L1-T2-C2	LBC1	TGL2	W24×131	35.6	50.6	0.27	2.37	0.54	7.7	1.76e-4	11	0
S8-L1-T2-C3	LBC1	TGL2	W30×148	41.6	65.9	0.24	2.21	0.60	5.4	1.63e-4	3	8

[a]Properties of first-story exterior columns
[b]SC: sidesway collapse. VC: vertical collapse.

4.4 Frame Variants

Key parameters that influence member capacity and, in turn, system capacity, are (1) lateral bracing condition (LBC); (2) tributary gravity loads (TGL); and (3) column section properties. A number of frame variants are created in order to investigate the effect of these parameters on system behavior.

4.4.1 Lateral Bracing Condition (LBC)

One of the primary parameters that determines a column's buckling strength is the unbraced length, *L*, which depends on the spacing of lateral bracing. In current seismic provisions (AISC 2016b), beam-column connections require lateral bracing at the levels of both the top and bottom beam flanges unless a column is shown to remain elastic outside of the panel zone. If the column remains elastic, which can be assumed when the column-beam moment ratio at the connections is larger than 2.0, the connection is permitted to be laterally braced only at the level of the top beam flanges. This typically happens for exterior columns, where the beam moment resistance contribution comes from only one beam. The limit on the column-beam moment ratio is described as a "reasonable cutoff" (AISC 2016b) and its effect on overall system behavior is not yet well studied.

Three different lateral bracing conditions are considered for the four-story frames: (1) beam-column connections are laterally braced at the levels of both the top and bottom beam flanges regardless of column-beam moment ratios at the connection (designated LBC1); (2) similar to the LBC1 condition, except that the lateral bracing of beam-column connections at the level of the bottom beam flanges is removed when the column-beam moment ratios at the connection are greater than 2.0 (designated LBC2); and (3) similar to the LBC1 condition, except that additional lateral bracing is applied at quarter points along the column height (designated LBC3).

Frames with LBC2 are compared to those with LBC1 to study the effect of removing lateral bracing at the bottom beam flanges allowing for evaluation of the "reasonable cutoff" comment in the current provisions (AISC 2016b). LBC3 is meant to greatly reduce the possibility of out-of-plane flexural buckling and lateral torsional buckling of columns in order to understand the general influence of column instabilities on frame collapse capacity. It is acknowledged that LBC3 is an impractical condition to achieve, but it nevertheless provides important insight into the effects of bracing on system behavior. The three LBC conditions are shown in Figure 4-3.

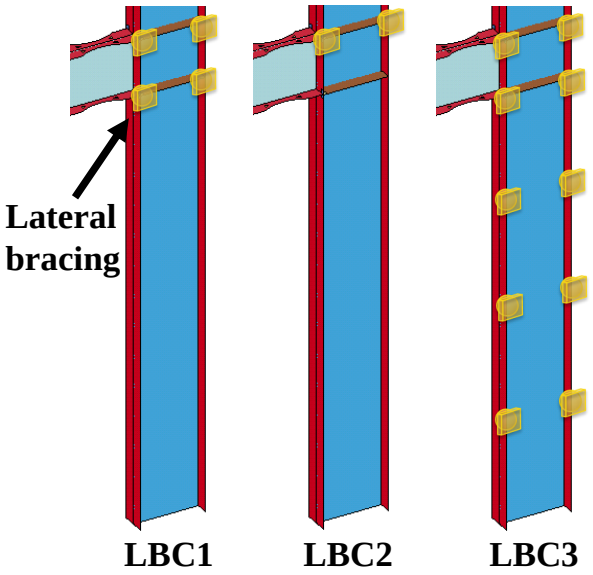

Figure 4-3. Lateral bracing conditions

4.4.2 Tributary Gravity Loads (TGL)

Wu et al. (2018a), Fogarty et al. (2017), Fogarty and El-Tawil (2015), Ozkula et al. (2017b) and Elkady and Lignos (2015a) showed that the initial column axial force, which results from gravity loading, plays an important role in determining the cyclic responses of deep columns. Therefore, the axial load ratio induced by the tributary gravity loads (TGL), P_g/P_y, for first-story exterior

columns is also selected as a key parameter in this study. P_g is the gravity load and P_y is the yield capacity of the cross-section of the column. As described in Section 3.3.2, the P_g/P_y ratio under the TGL indicated in Figure 3-1(a) using the load combination of 1.05D+0.25L per FEMA P695 (2009) is 0.18 for the four-story frame. The level of axial load caused by this tributary area is designated as TGL2. To explore the effect of TGL on the collapse capacity of the SMF, a lower level (P_g/P_y = 0.11, TGL1) and a higher level (P_g/P_y = 0.27, TGL3) are employed to reflect smaller and greater tributary areas, respectively. The TGL1 and TGL3 cases are considered to be reasonable and could correspond to feasible design situations. The seismic weight of the SMF in the three TGL cases remains unchanged to maintain the same seismic force.

To account for all possible combinations of LBC and TGL conditions, eight variants of the four-story frame are created in addition to the prototype frame. A descriptive naming scheme is utilized in order to facilitate discussion of the key parameters. For example, the prototype four-story frame is designated S4-L1-T2-C1, where S4, L1, and T2 stands for four-story, LBC1, and TGL2, respectively, and C1 refers to W24×103 section as the first-story exterior columns. Following the same designation, the variant S4-L3-T2-C1 is the four-story frame with LBC3 and TGL2 conditions and W24×103 exterior columns. Details of the variants are listed in Table 4-1.

4.4.3 Column Section Properties

Aside from the initial axial load, the web slenderness ratio (h/t_w) and global slenderness ratio (L/r_y) have also been shown to be significant factors affecting deep column capacity (Fogarty and El-Tawil 2015; Wu et al. 2018a). To study their potential influence on frame capacity, another variant is created by replacing the first-story exterior columns of the S4-L1-T3-C1 frame with a W24×131 section, which has a slightly smaller h/t_w and much smaller L/r_y than the original W24×103 section.

The variant is designated S4-L1-T3-C2, as shown in Figure 4-1(b), where C2 refers to W24×131 section.

To further investigate the effect of L/r_y, the prototype eight-story frame (S8-L1-T2-C2 in Table 4-1), is redesigned using W30 shapes as column sections in accordance with the latest specifications (AISC 2016a, 2016b and ASCE 2016). The redesigned frame, which has a larger exterior column L/r_y than the prototype, is shown in Figure 4-2(b) with the column sections in parenthesis. It is termed S8-L1-T2-C3 in Table 4-1, where C3 refers to W30×148 first-story columns. The larger L/r_y necessitates the use of a heavier section (W30×148) for first-story exterior columns in order to satisfy strength requirements. The W30×148 section is also used for interior columns. Even though it is lighter than that originally used (W24×162), it satisfies design requirements including the more stringent strong-column/weak-beam requirement in AISC (2016b). As a result, the S8-L1-T2-C3 frame has a similar weight compared to S8-L1-T2-C2, but higher system flexural stiffness, i.e. shorter fundamental period T_1.

4.5 Finite Element Modeling

4.5.1. Modeling Approach

The detailed finite element modeling and analysis scheme of the SMFs are the same as described in Section 3.3.2 except that column flanges are laterally braced at locations based on the SMFs' LBC shown in Figure 4-3. The material calibration is shown in Figure 3-2, and the frame model with the leaning column and the details of key parts of the model are shown in Figure 4-4 and Figure 4-5. The finite element models of the four-story and eight story frames consist of approximately 96,000 and 235,000 elements, respectively. The simulations run on a cluster with 16 processors. The simulation time to model 30 seconds of real time is about 30 and 57 hours for

the four-story and eight-story prototype frames, respectively. A total of 836 simulations are performed in this study.

4.5.2. Collapse Criteria

The collapse behavior of SMFs under seismic loading is commonly categorized into two mechanisms: sidesway collapse and vertical collapse. Sidesway collapse, which occurs when the lateral resistance of the SMF is overcome by P-Delta effects due to excessive lateral displacements, has been extensively studied in previous research (Zareian et al. 2010; Eads et al. 2013; Hamidia et al. 2014). On the other hand, vertical collapse, which is initiated by the inability of columns to support gravity loads, has not received as much attention as it deserves, particularly in the presence of deep wide flange columns. To thoroughly investigate the influence of column behavior on the collapse potential of SMFs, both collapse modes are considered in this study.

Two types of sidesway mechanisms are observed: first-story and multi-story mechanisms. Figure 4-6 shows the progression of a first-story mechanism for S8-L1-T2-C2 subjected to the ground motion record Northr/MUL009. The collapse process begins with extensive local buckling at the bottom ends of the first-story columns as well as the RBS regions in the beams at about 22 seconds. The local instabilities result in strength and stiffness deterioration of the columns and impair the lateral resistance of the frame, accelerating the drift response. At about 27 seconds, the P-Delta effect becomes large enough to overcome lateral resistance, triggering the formation of a first-story mechanism.

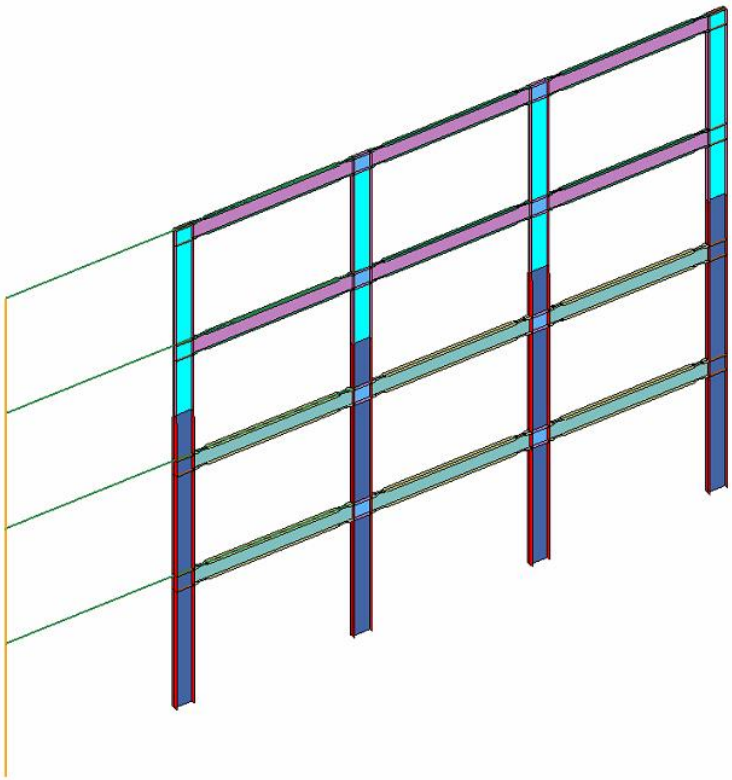

(a)

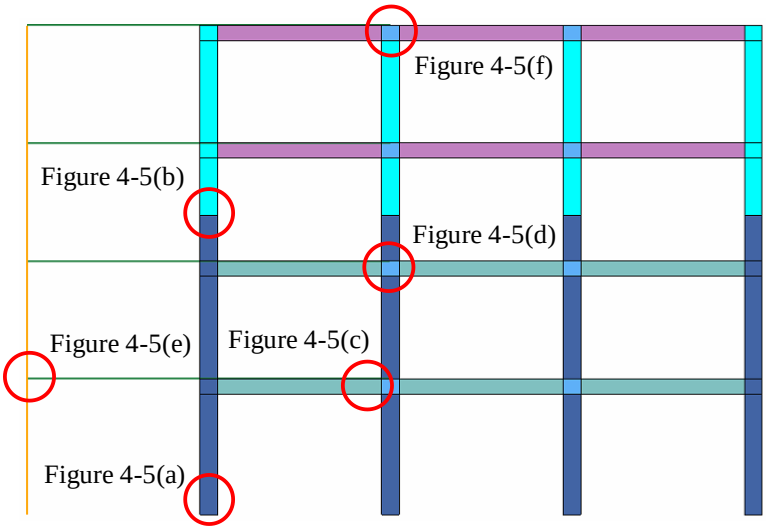

(b)

(c)

Figure 4-4. Finite element model of the prototype four-story frame. (a) 3-D view; (b) elevation view; and (c) top view

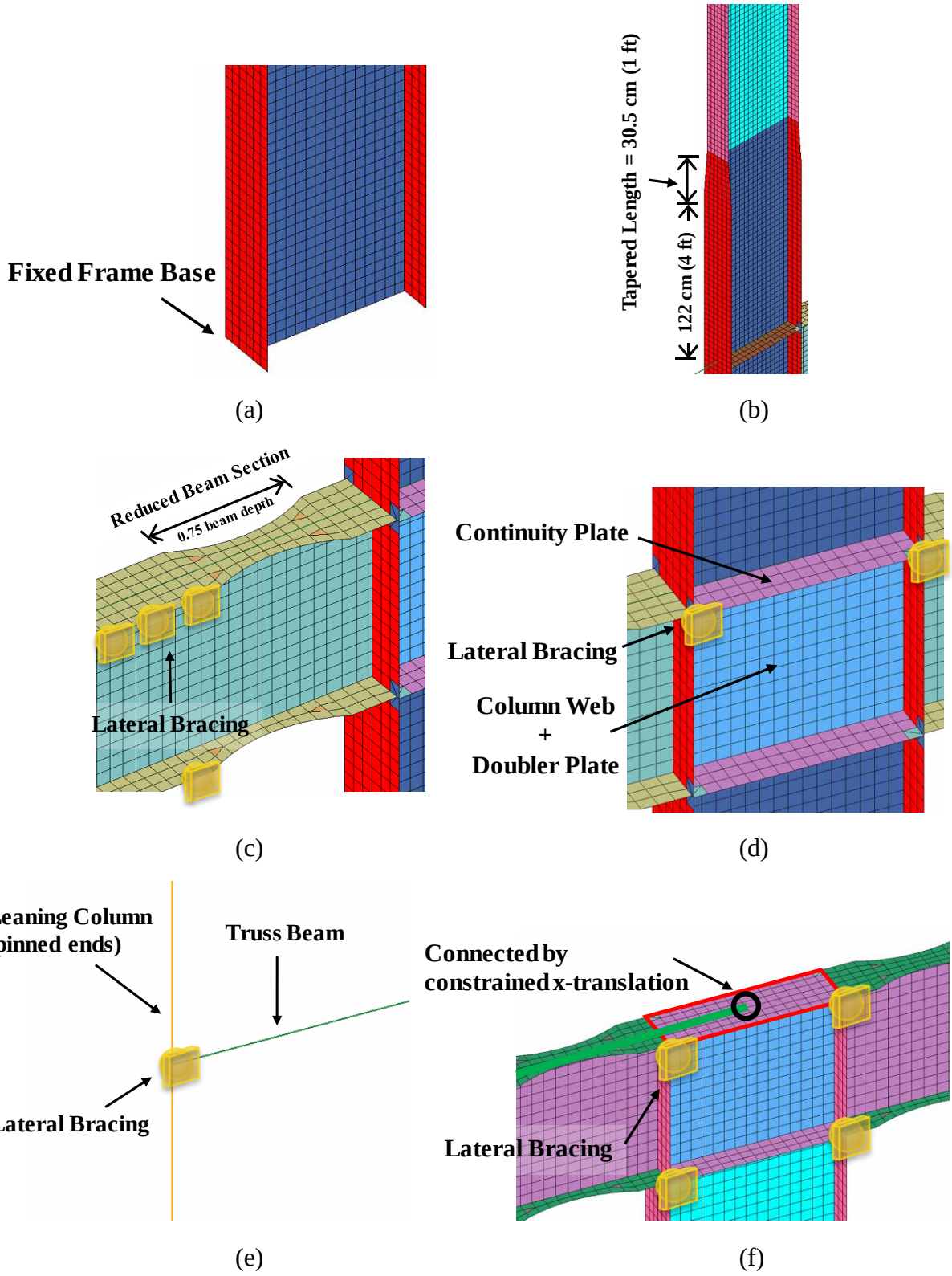

Figure 4-5. Details of the frame model. (a) frame base; (b) column splice; (c) reduced beam section; (d) beam-to-column connection; (e) leaning column and truss beam; and (f) connection between truss beam and the frame

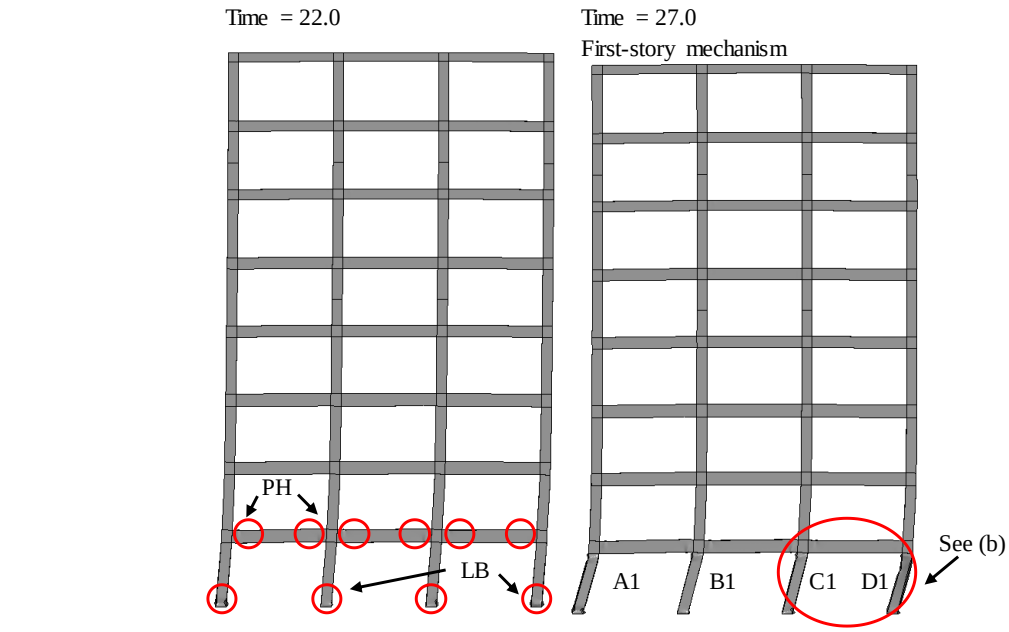

(a)

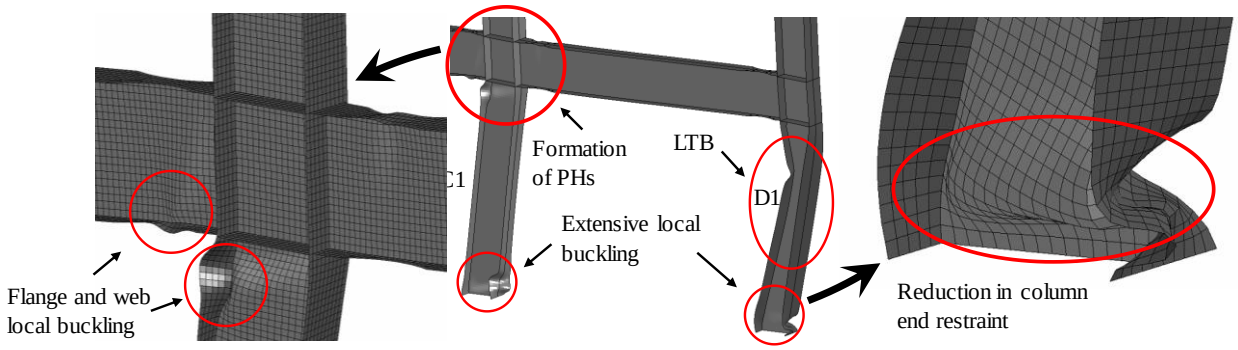

(b)

Figure 4-6. (a) Progression of first-story mechanism (PH: Plastic Hinges, LB: Local Buckling, LTB: Lateral Torsional Buckling); and (b) local instabilities at the bottom ends of the first-story columns as well as the RBS regions in the beams

Modeling the sidesway collapse process can be computationally expensive because in many cases, the SMF continues to lean over slowly after the end of the imposed seismic loading until it reaches equilibrium and stops or continues on to complete collapse. Therefore, to limit the computational effort, which is proportional to the simulated time in explicit integration schemes, as used herein,

the maximum simulated time is determined as the time needed for the Arias intensity to reach 95% (i.e. $t_{IA=95\%}$) (Arias 1970) plus 10 seconds. For example, the simulation is terminated at 27.64 second for the ground motion record Northr/MUL009 that has a $t_{IA=95\%}$ of 17.64 seconds. Sidesway collapse is assumed to occur during this time if: 1) the maximum story drift ratio surpasses 10%, 2) there is an increase of 2% or more in story drift ratio during the last 10 second window of simulated time.

The former criterion is a reasonable lateral deformation limit attributed to Vamvatsikos and Cornell (2002) and commonly used by others. The latter criterion is based on the observation that the closer the SMF is to collapse, the faster its rate of drift. This trend can be seen in Figure 4-7(a), which shows the first-story drift ratio history of the S4-L1-T1-C1 frame subjected to the ground motion record Hector/HEC000 scaled to increasing S_a (T_1, 5%), the 5% damped spectral acceleration at the fundamental period. The two vertical dashed lines represent the 10 second interval after $t_{IA=95\%}$. It is clear that as the spectral acceleration increases, the story drift history not only reaches a larger drift level, but also increases at a faster rate. This phenomenon can be better appreciated in Figure 4-7(b), which plots the relationship between S_a (T_1, 5%) and v_{SDR}, the story drift ratio rate (%/sec) averaged over the last 10 seconds of simulated time. It is obvious that v_{SDR} increases faster as S_a (T_1, 5%) increases, signaling that the SMF is on its way to sidesway collapse as the seismic intensity increases. Based on numerous simulations that explored how frames undergo sidesway collapse, it was found that the 2% threshold signaled eventual sidesway collapse.

Unlike sidesway collapse, vertical collapse can be clearly identified from the deformed shape of the frame. Vertical collapse usually begins with column failure followed by a redistribution of gravity loads, leading to successive failures of adjacent columns and eventually a vertical

progressive collapse scenario, as can be seen in Figure 4-8. The axial force in exterior column A1 fluctuates about its initial level (caused by gravity loads) due to the overturning moments caused by seismic shaking. As column A1 fails due to flexural buckling and loses its ability to carry the imposed axial load demands (time = 21.5 sec), the adjacent column B1 attempts to take over column A1's share of the load, but it is unable to (time = 24.0 sec). The successive loss of column axial capacity leads to vertical progressive collapse of the SMF at time = 24.5 sec.

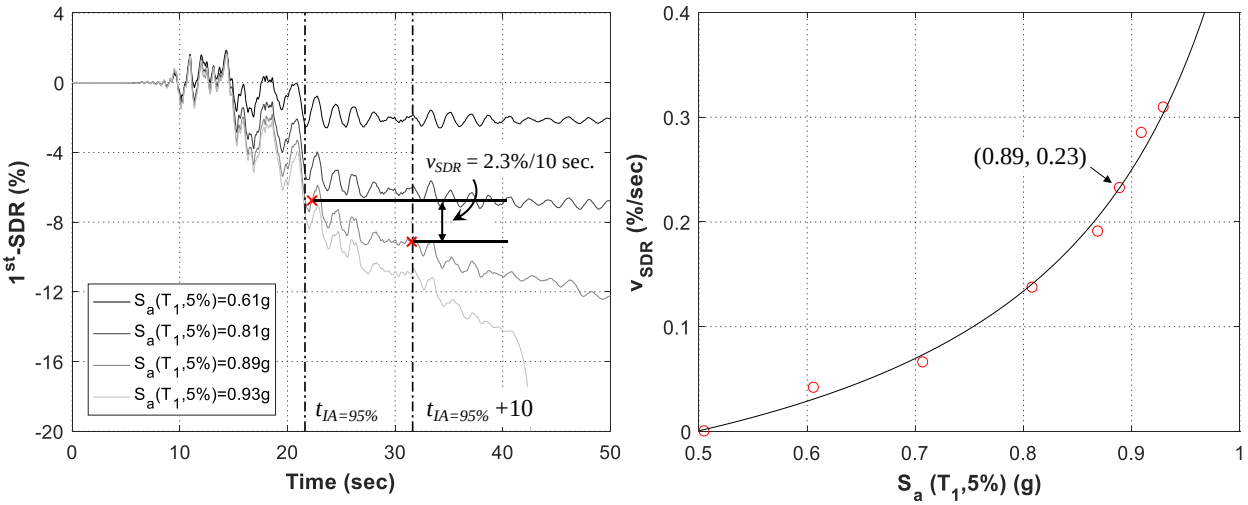

(a) (b)

Figure 4-7. (a) First-story drift ratio history; and (b) story drift ratio rate averaged over the last 10 second window (v_{SDR}, %/sec) of the S4-L1-T1-C1 frame subject to the Hector/HEC000 record with different $S_a(T_1, 5\%)$

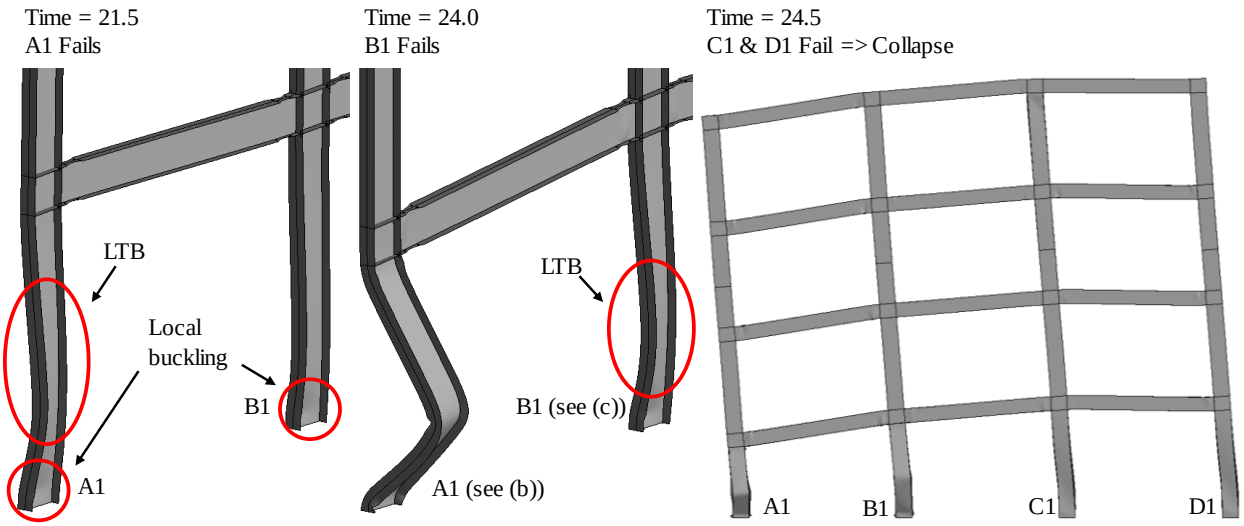

(a)

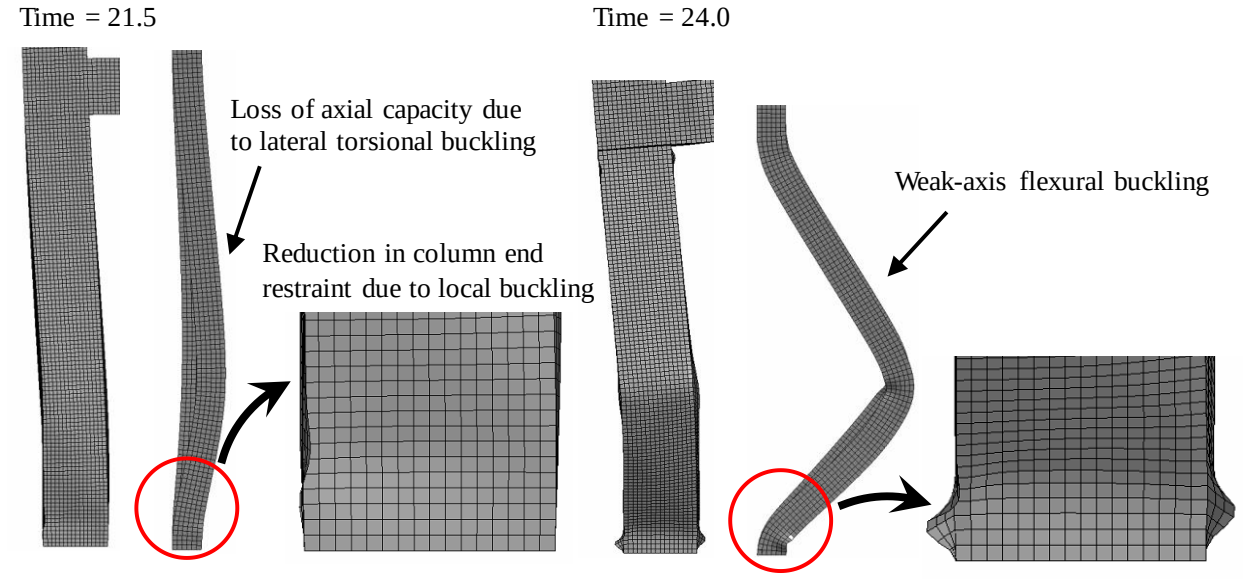

(b)

Figure 4-8. (a) Progression of vertical collapse for S4-L1-T3-C1 frame subject to the Hector/HEC000 record with $S_a(T_1, 5\%) = 0.71g$; (b) failure of column A1; and (c) failure of column B1

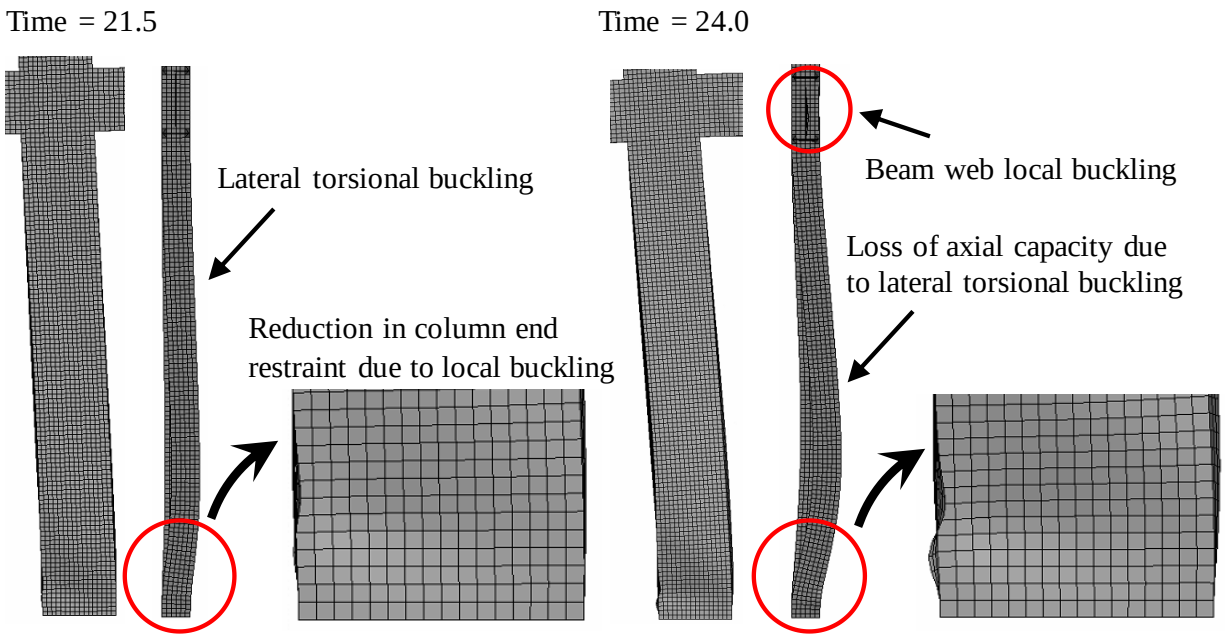

(c)

Figure 4-8 (continued). (a) Progression of vertical collapse for S4-L1-T3-C1 frame subject to the Hector/HEC000 record with $S_a(T_1, 5\%) = 0.71g$; (b) failure of column A1; and (c) failure of column B1

4.6 Simulation Results

The collapse capacities of the SMFs listed in Table 4-1 are evaluated through finite element analysis to study the influence of key parameters. FEMA P-58 (2012) suggests that 11 pairs of motions (i.e. 22 records) should be used to adequately capture variability in ground motion. However, the high computational cost associated with running the frame models makes complying with this recommendation prohibitive. As a compromise between computational expediency and accuracy, eleven ground motion records (one from each of 11 pairs) selected from the Far-Field record set in FEMA P695 (2009) are employed in the evaluation and listed in Table 3-1.

Incremental dynamic analysis (IDA) (Vamvatsikos and Cornell 2002) is applied to obtain the collapse parameters associated with each record, i.e. spectral acceleration, $S_{a,C}(T_1, 5\%)$, and maximum story drift ratio at frame collapse, $SDR_{max,C}$, when one of the collapse criteria is met under the scaled record. Figure 4-9 shows an example of the IDA curves for the S4-L1-T1-C1 frame with the identified collapses marked by circles, which represent the collapse parameters of the frame. The obtained $S_{a,C}(T_1, 5\%)$ and $SDR_{max,C}$ are used to determine the collapse fragility curves of each SMF by fitting the data to a lognormal distribution using the Collapse Fragility Tool provided in FEMA P-58 (2012). The mean annual frequencies of collapse, λ_c, are also computed by numerically integrating the collapse fragility curves with the seismic hazard curves as was done in Ibarra and Krawinkler (2005). It is assumed that the frames are located at Square Park in Seattle (47.600, -122.300) with Site Class D. Seismic hazard data is obtained from the Unified Hazard Tool on the USGS website (Conterminous U.S. 2008).

The analysis results are summarized in Table 4-1, which includes the collapse capacity of each frame, i.e. the fitted median values of $S_{a,C}$ and $SDR_{max,C}$, $\tilde{S}_{a,C}$ and $\widetilde{SDR}_{max,C}$, the mean annual frequencies of collapse, λ_c, and the number of records causing different collapse modes. The collapse fragility curves of the four-story and the eight-story SMFs are plotted in Figure 4-10 and Figure 4-11, respectively. As can be seen from Table 4-1, for the assumed frame location, both eight-story frames exhibit λ_c < 2.01e-4, which is the current limit imposed by ASCE (2016) to achieve a 1% probability of collapse in 50-years. However, all of the four-story frames exhibit λ_c > 2.01e-4, indicating that their risk for collapse is greater than that expected by current specifications. One key reason that the four-story frames exhibit higher λ_c values than eight-story frames is the higher seismic hazard associated with the fundamental period of the four-story frames versus the taller eight-story frames.

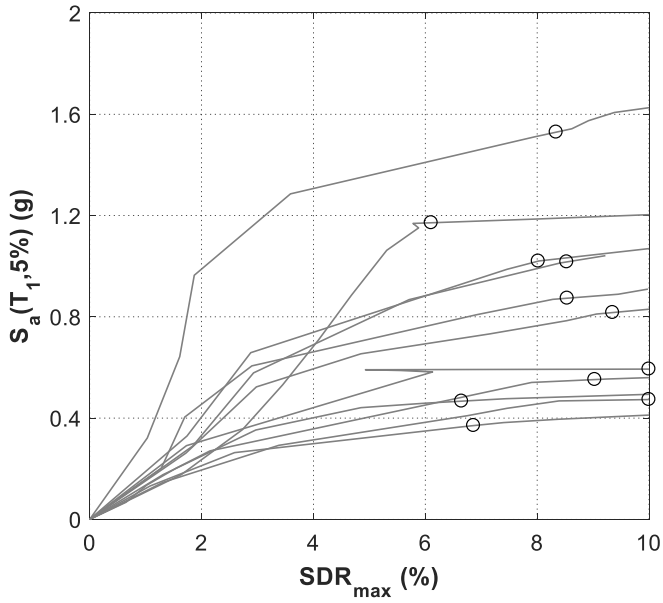

Figure 4-9. IDA curves for the S4-L1-T1-C1 frame

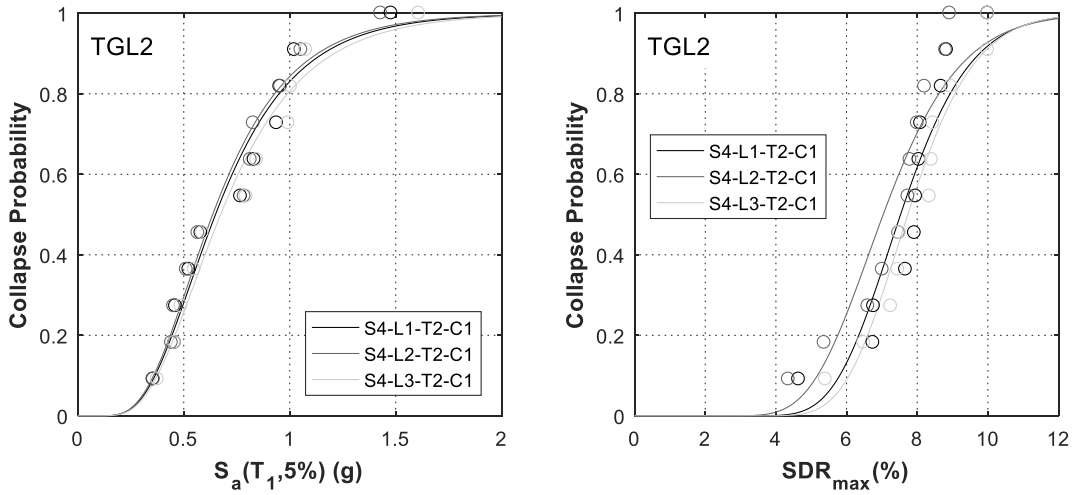

(a) (b)

Figure 4-10. Collapse fragility curves of the four-story SMFs with (a)(c)(e) spectral acceleration $S_a(T_1,5\%)$; and (b)(d)(f) maximum story drift ratio SDR_{max} along the x-axis

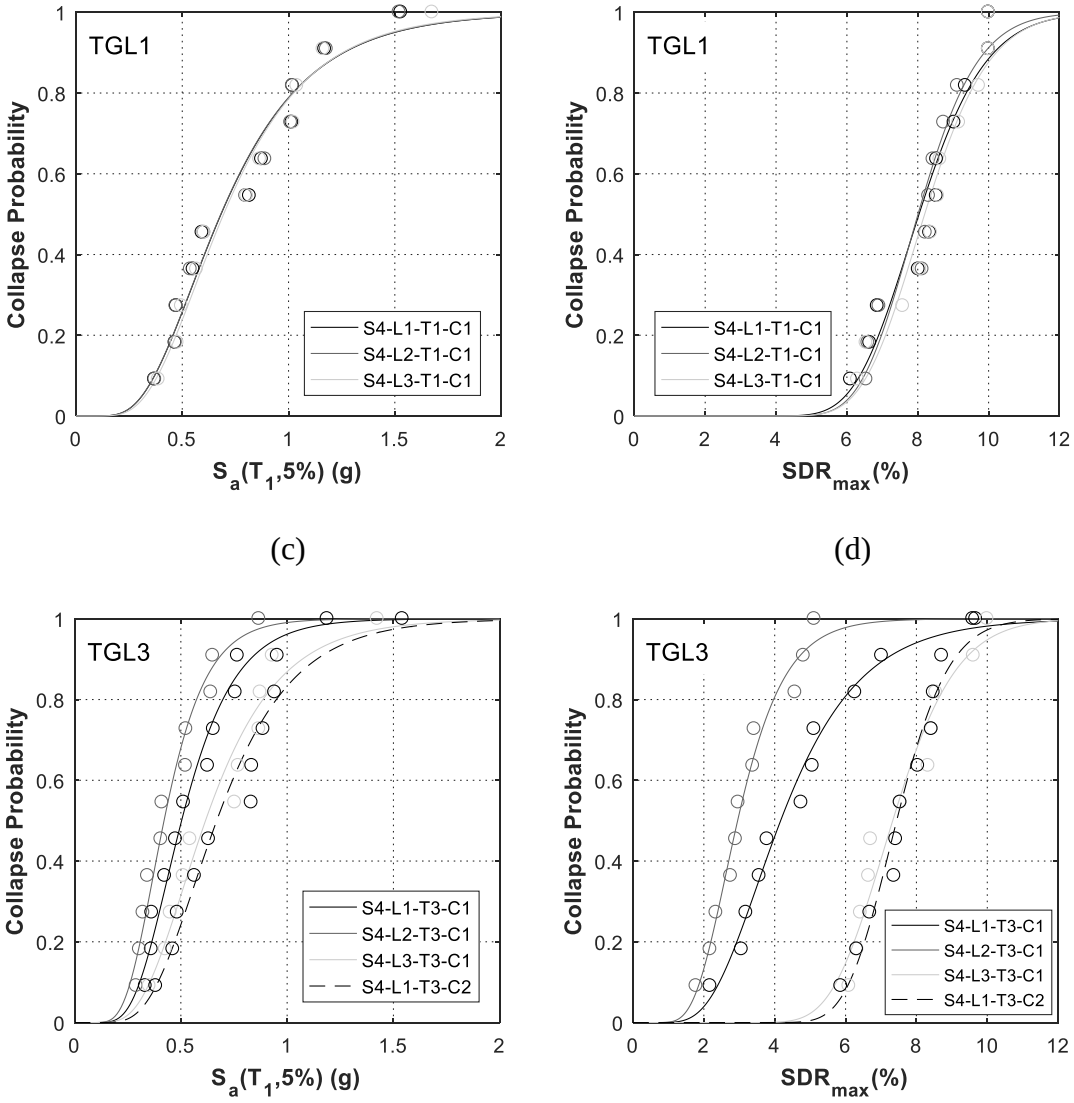

Figure 4-10 (continued). Collapse fragility curves of the four-story SMFs with (a)(c)(e) spectral acceleration $S_a(T_1,5\%)$; and (b)(d)(f) maximum story drift ratio SDR_{max} along the x-axis

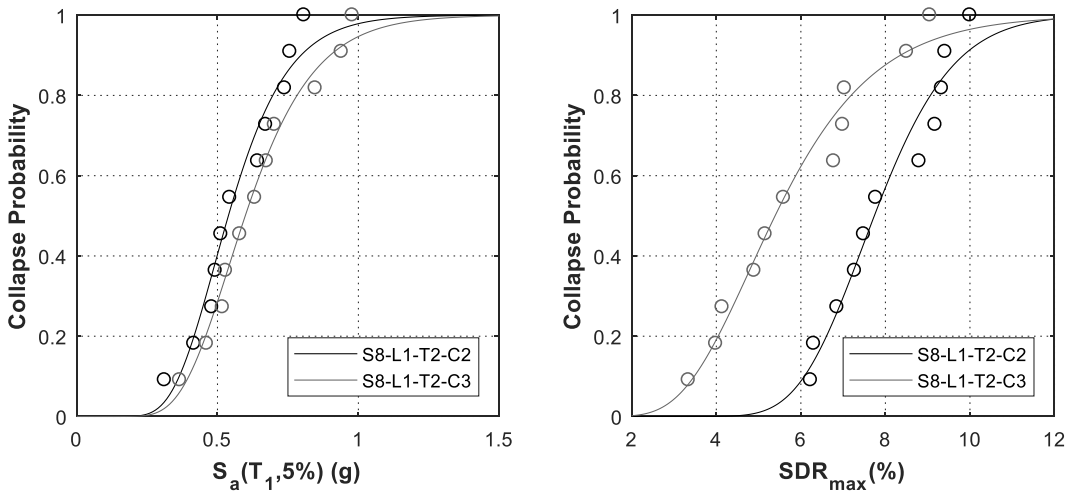

(a) (b)

Figure 4-11. Collapse fragility curves of the eight-story SMFs with (a) spectral acceleration $S_a(T_1,5\%)$; and (b) maximum story drift ratio SDR_{max} along the x-axis

4.6.1. Effect of LBC and TGL

It appears from Table 4-1 and Figure 4-10(a) that lateral bracing has little effect on collapse response for the TGL2 condition. For example, the collapse fragility curves in Figure 4-10(a) are nearly identical to each other and the median $\tilde{S}_{\mathrm{a,C}}$ and λ_c values in Table 4-1 are close to one another (0.65g and 4.43e-4 for S4-L1-T2-C1, 0.64g and 4.63e-4 for S4-L2-T2-C1, and 0.67g and 4.12e-4 for S4-L3-T2-C1). However, as shown in Figure 4-10(b), there is a subtle difference: the collapse modes differ as listed in Table 4-1. For example, none of the seismic records cause vertical collapse of the S4-L3-T2-C1 frame, which has LBC3 condition. On the other hand, one and two records for the S4-L1-T2-C1 and S4-L2-T2-C1 frames, respectively, lead to vertical collapse as the lateral bracing condition is eased.

Frames S4-L1-T2-C1, S4-L2-T2-C1 and S4-L3-T2-C1 also exhibit similar $\widetilde{SDR}_{\mathrm{max,C}}$ values (7.5% for S4-L1-T2-C1, 7.0% for S4-L2-T2-C1 and 7.7% for S4-L3-T2-C1, as shown in Figure 4-10(b)).

These levels of $SDR_{max,C}$ are substantially higher than the achievable drift ratios seen in previous member level studies, e.g. Fogarty and El-Tawil (2015), Elkady and Lignos (2015a), and Ozkula et al. (2017b). The discrepancy mainly results from that the fact that earlier studies employed symmetric cyclic loading protocols, which impose more severe demands on the columns than actually occurs in the frame undergoing collapse. As explained in Wu et al. (2018a) and observed in Elkady and Lignos (2017), the ratcheting behavior that occurs during collapse, which is obvious in Figure 4-7(a) and was discussed in Krawinkler (2009), is substantially more benign than symmetric cyclic loading.

The effect of lateral bracing on collapse capacity is also small for frames with TGL1 condition, i.e. the S4-L1-T1-C1, S4-L2-T1-C1, and S4-L3-T1-C1 frames. The $\tilde{S}_{\mathrm{a,C}}$, $S\widetilde{D}R_{\mathrm{max,C}}$, and λ_c values are almost identical for all three frames as well as the collapse fragility curves, as shown in Table 4-1 and Figure 4-10(c) and Figure 4-10(d). Unlike the TGL2 condition where there were a few instances of vertical collapse, the three frames fail by sidesway collapse under all ground motion records.

At the other extreme and as shown in Figure 4-10(e) and Figure 4-10(f), the TGL3 condition, which imposes higher axial loads, greatly exacerbates instabilities in the columns as evidenced by the substantial sensitivity to the lateral bracing conditions. For example, compared to the LBC1 conditions, $\tilde{S}_{\mathrm{a,C}}$ for the LBC2 condition decreases from $0.50g$ to $0.42g$ (S4-L1-T3-C1 versus S4-L2-T3-C1) and increases to $0.62g$ for the LBC3 case (S4-L1-T3-C1 versus S4-L3-T3-C1). The differences in λ_c also show the significance of lateral bracing as the λ_c of S4-L2-T3-C1 is 42% higher than the one of S4-L1-T3-C1, double of that of S4-L3-T3-C1. The effect is even more pronounced for $S\widetilde{D}R_{\mathrm{max,C}}$. For example, $S\widetilde{D}R_{\mathrm{max,C}}$ of S4-L1-T3-C1, S4-L2-T3-C1, and S4-L3-T3-

C1 is 4.2%, 3.0%, and 7.3%, respectively. The fact that $S\widetilde{D}R_{\max,C}$< 4.0% for S4-L2-T3-C1 and is just above 4.0% for S4-L1-T3-C1 is concerning because current specifications usually assume that a 4% drift level is achievable under design-level seismic loading. The reason for the comparatively poor performance under TGL3 condition is the vulnerability of deep columns to instability at higher axial loads, which compromises their ability to support axial load, promoting overall system failure.

The mode of failure for S4-L1-T3-C1 and S4-L2-T3-C1 changes from being primarily dominated by sidesway collapse under TGL1 condition to mostly vertical collapse under TGL3 condition (see Table 4-1). The effect of axial load is substantial enough that one of the S4-L3-T3-C1 cases underwent vertical collapse in spite of the extensive lateral bracing provided by the LBC3 condition. Under seismic record Duzce/BOL000, the S4-L3-T3-C1 frame collapsed in a vertical progressive manner because the columns suffered extensive local buckling as shown in Figure 4-12.

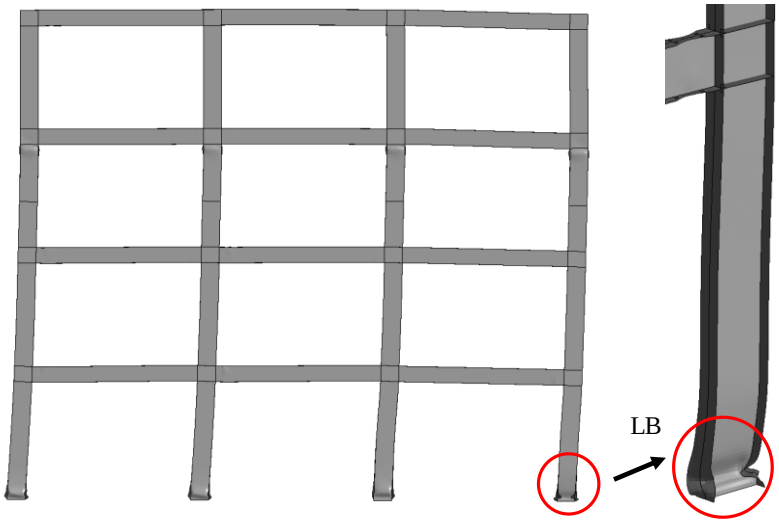

Figure 4-12. Vertical collapse induced by severe local buckling in the S4-L3-T3-C1 frame subject to the Duzce/BOL000 record with $S_a(T_1, 5\%) = 0.87g$

Another key point is that the effect of TGL increases the higher it becomes. For example, $\tilde{S}_{a,C}$ for S4-L2-T1-C1 (TGL1, P_g/P_y = 0.11) is 0.68g. This decreases slightly to 0.64g for S4-L2-T2-C1 (TGL2, P_g/P_y = 0.18) and significantly to 0.42g for S4-L2-T3-C1 (TGL3, P_g/P_y = 0.27). The sharp increase of λ_c from 4.63e-4 of S4-L2-T2-C1 to 9.99e-4 of S4-L2-T3-C1 also reflects the trend. This effect is further emphasized in Figure 4-13, which plots the relationship between P_g/P_y and SDR_{max} for LBC1 condition for various probabilities of collapse. Figure 4-13 clearly shows the negative relationship between P_g/P_y and SDR_{max} and that SRD_{max} decreases rapidly when P_g/P_y surpasses about 0.2. For example, the probability of collapse before 4% drift is 10% and 20% for P_g/P_y = 0.24 and 0.25, respectively. In other words, a 1% increase in the gravity load to yield strength ratio causes a disproportionate 10% increase in the probability of collapse. This high sensitivity to axial load level shows that an appropriate axial load limit should be specified in design specifications. The current AISC seismic provisions (2016b) do not include a limit, but CSA S-16 (2014) suggests a limit of 0.3P_y. However, based on the presented research results, 0.3P_y appears to be unconservative.

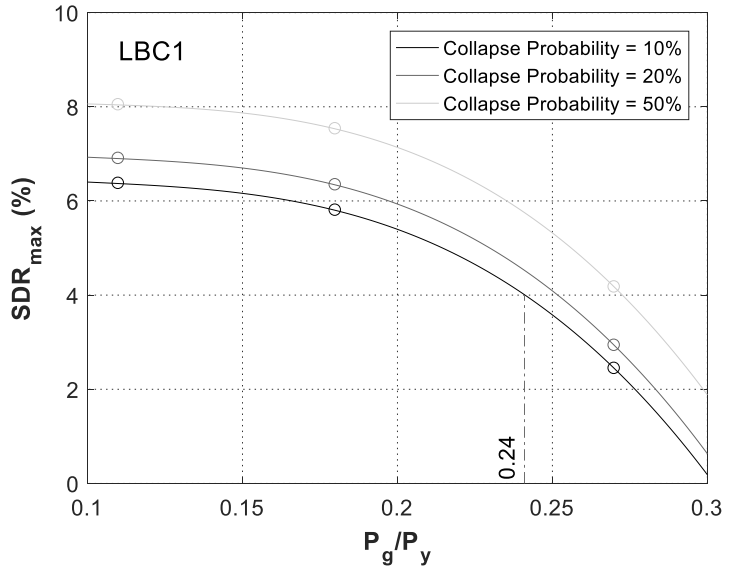

Figure 4-13. Correlation trend between the level of gravity loads and SDR_{max} with different collapse probabilities for the four-story frame with LBC1 condition

4.6.2. Effect of Column Section Properties

The first-story exterior columns of S4-L1-T3-C2 (W24×131) have a smaller h/t_w and significantly smaller L/r_y than those of S4-L1-T3-C1 (W24×103). Because these two frames are similar otherwise, as evinced by almost equal T_1, it is fair to compare their $S_{a,C}$ values directly. Figure 4-10(e) and Figure 4-10(f) show the collapse fragility curves of frames with TGL3 condition. As can be seen, S4-L1-T3-C2 is substantially better than S4-L1-T3-C1. For example, $\tilde{S}_{\mathrm{a,C}}$ increases from $0.50g$ for S4-L1-T3-C1 to $0.67g$ for S4-L1-T3-C2 and $S\tilde{D}R_{\mathrm{max,C}}$ increases from 4.2% to 7.4%. Moreover, the dominant collapse mode changes from vertical collapse (for S4-L1-T3-C1) to sidesway collapse (for S4-L1-T3-C2), as shown in Table 4-1. These results highlight the detrimental influence that a high L/r_y can have on overall system behavior.

While frames S8-L1-T2-C2 and S8-L1-T2-C3 cannot be compared directly using their $S_{a,C}$ and collapse fragility curves in Figure 4-11(a) due to their different fundamental periods, their λ_c values show that the two frames have comparable risks of collapse (1.76e-4 versus 1.63e-4) in terms of spectral accelerations. However, as shown in Figure 4-11(b) and Table 4-1, S8-L1-T2-C2 has a much better drift capacity and therefore a higher $S\tilde{D}R_{\mathrm{max,C}}$ (7.7%) compared with S8-L1-T2-C3 ($S\tilde{D}R_{\mathrm{max,C}}$=5.4%). Of particular concern is that one of the earthquake records causes collapse of S8-L1-T2-C3 at 3.3% drift. Moreover, as listed in Table 4-1, S8-L1-T2-C2 consistently collapses in sidesway mode, while S8-L1-T2-C3 collapses in vertical collapse under eight of the eleven ground motion records used. The above results suggest that S8-L1-T2-C2 has superior ductility to S8-L1-T2-C3 and a preferred failure mode.

The results above indicate that a SMF designed according to the latest seismic provisions does not necessarily have better seismic performance than that designed according to earlier AISC

provisions in 2005. Even though the first-story exterior column of S8-L1-T2-C3 (W30×148) has a slightly lower P_g/P_y than the one in the S8-L1-T2-C2 (W24×131), the W30×148 section has higher web and global slenderness ratios, h/t_w and L/r_y, which offset the benefits of the lower axial demand. These specific slenderness parameters have been identified as important factors for column capacity by Fogarty et al. (2017) and Wu et al. (2018a) and are the primary reason that S8-L1-T2-C3 performs worse than S8-L1-T2-C2 in spite of the heavier column section.

4.6.3. Axial Demands

Vertical collapse of SMFs is undesirable and results from global instability of column members. Table 4-2 shows P_{max} for frames with LBC1 condition, where P_{max} is the maximum axial force in the first-story exterior columns during each earthquake, averaged across all records. Also shown in Table 4-2 is the axial force that results from the capacity-limited seismic load effect, P_{cl}, as defined in AISC (2016b):

$$P_{cl} = \sum 2M_{pr,n}L_{h,n} \qquad (4\text{-}2)$$

where $L_{h,n}$ is the distance between plastic hinge locations at the nth-story and $M_{pr,n}$ is the maximum probable moment at the location of the plastic hinge at the nth-story as defined in AISC (2016a).

As can be seen from Table 4-2, the sum of axial forces induced by gravity loads and capacity-limited effects, i.e. P_g and P_{cl}, is generally slightly smaller than P_{max} for the four-story frame. The reason Equation (4-2) underestimates P_{max} is because the strain hardening that takes place is underestimated in the computation of P_{cl}. For example, while AISC (2016a) assumes that strain hardening is 1.15 in the computation of $M_{pr,n}$ of RBS connections made of A992 steel, values of about 1.25 are routinely seen in the four-story frame used in this research. An opposite trend occurs

in the eight-story frame, where the capacity-limited effect is substantially overestimated (17% to 19%) by Equation (4-2) for the eight-story frames. This is directly attributed to higher vibration modes, as evidenced by the deformed shape of the vibrating frames and suggests that even higher conservatism may be present for taller structures.

Table 4-2. P_{max} for first-story exterior columns

Frame ID	Column Section	P_g/P_y	P_{cl}/P_y	$(P_g+P_{cl})/P_y$	P_{max}/P_y
4-story					
S4-L1-T1-C1	W24×103	0.11	0.15	0.26	0.27
S4-L1-T2-C1	W24×103	0.18	0.15	0.33	0.35
S4-L1-T3-C1	W24×103	0.27	0.15	0.42	0.43
S4-L1-T3-C2	W24×131	0.21	0.12	0.33	0.35
8-story					
S8-L1-T2-C2	W24×131	0.27	0.48	0.75	0.64
S8-L1-T2-C3	W30×148	0.24	0.44	0.68	0.59

4.6.4. Column Axial Shortening

As identified in Section 3.5.3, several studies discussed the shortening behavior of deep columns subjected to combined axial and cyclic lateral loading (Elkady and Lignos 2015a, 2017; Ozkula et al. 2017b). Fogarty et al. (2017) showed that axial shortening is mainly attributed to flange and web local buckling and suggested that it can be controlled through compactness criteria. Elkady and Lignos (2017) noted that axial shortening is milder in a fixed-flexible column under collapse-consistent loading compared to a fixed-fixed column under symmetric cyclic loading. Based on the small values observed in the individual column study presented in Chapter 3, axial shortening is considered to be a serviceability issue. A common thread in all the above studies, which appear to have conflicting attitudes towards the importance of the axial shortening phenomenon, is that the results were derived from component studies.

The current study presents a unique opportunity to investigate this complex issue at the system level. To assess the extent of column shortening behavior during strong earthquake events, Figure 4-14 plots the maximum beam slope (MBS) versus drift level. MBS is the maximum of the vertical displacements (δ_{max}) at the top of the four first-story columns normalized by beam span length (L_s). Since the beams in the along-frame and transverse directions are equal in length (L_s = 6.10 m), MBS is essentially the maximum slope of the beams framing into the first-story columns assuming the other beam ends do not have vertical deformation. It is essentially a measure of axial shortening in the system and is computed for each record when the first-story drift first reaches drifts of 1% through 4% with 1% increments. The computed MBS values are plotted as circles in Figure 4-14. Frames that collapse at the next drift level up are plotted in red and circumscribed with an oval.

AISC (2016c) specifies a deflection limit of 1/300 of the span for architectural serviceability requirements and 1/200 of the span for the serviceability of equipment with moveable components. Figure 4-14(a) shows that the MBS levels for S4-L1-T2-C1 are well below 1/500 at 1% drift, which is commonly associated with the immediate occupancy performance level. Even at 4% drift (at the collapse prevention performance level), MBS values are mostly less than 1/200. At such a high lateral drift level, the priority is preserving integrity over violating serviceability. When the gravity load is increased in S4-L1-T3-C1, MBS is still small, and serviceability is not affected at 1% drift (Figure 4-14(b)). MBS grows beyond 1/200 at 3% drift. However, at such a high drift level, poor structural performance is of more concern than serviceability, as also noted for S4-L1-T2-C1.

The S4-L1-T3-C1 frames with the highest MBS at 3% drift (highlighted by an oval in Figure 4-14(b)) collapse before the next drift level is reached due to global buckling of exterior columns. Comparing the MBS range at 4% drift in Figure 4-14(a) (S4-L1-T2-C1: range is 0.2%-0.6%) and

that at 3% drift in Figure 4-14(b) (S4-L1-T3-C1: range is 0.2%-0.75%), it is clear that frames with similar column shortening have quite different collapse behaviors. This suggests that column shortening, in itself, does not play a direct role in collapse response. It is merely a symptom of local buckling. Excessive local buckling can be detrimental because it can reduce column end restraints, which can compromise column axial resistance and increase the potential for system collapse as the axial load demand increases.

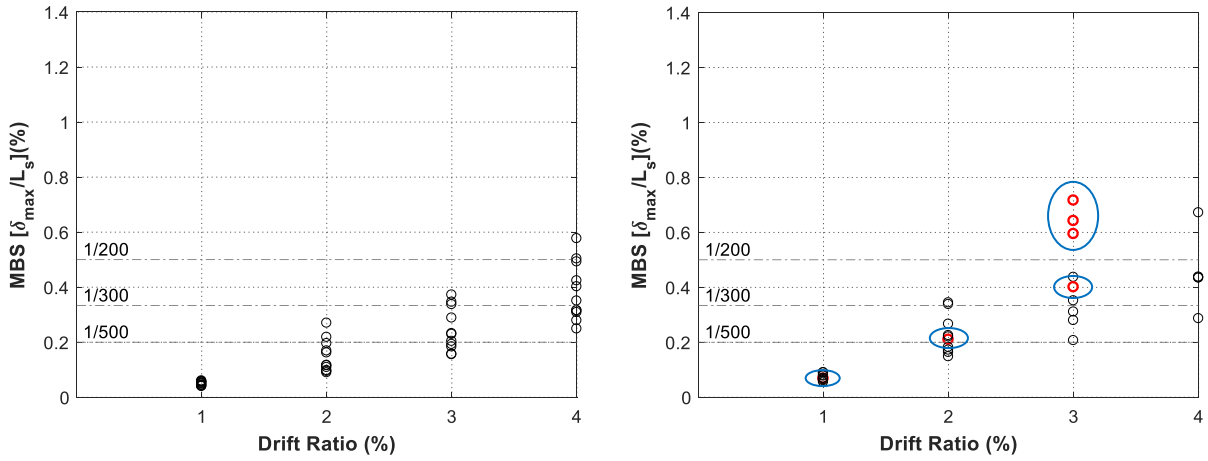

Figure 4-14. Maximum beam slope evolution of the beams framing into the first-story columns in the frames with LBC1 condition under collapse-induced records. (a) S4-L1-T2-C1; (b) S4-L1-T3-C1

4.7 Conclusions

The collapse behavior of steel SMFs was investigated using computational simulation. Unlike the majority of previous studies, this research employed validated models capable of simulating local and global member instabilities and explicitly representing the seismic collapse response of the entire system. The models were used to study the effect of three influential parameters on system response: (1) column lateral bracing; (2) level of gravity load on the columns; and (3) column

section properties. After defining clear collapse criteria, it was shown that frames can fail in either sidesway or vertical progressive collapse manners. Incremental dynamic analyses were conducted to compute the collapse fragility curves for a range of SMF designs.

The following conclusions can be drawn from the set of simulations conducted within the limitations and assumptions outlined earlier.

- Earlier component level studies have shown that web and global slenderness ratios of columns, h/t_w and L/r_y, have a considerable influence on the axial capacity of deep columns. The system level studies conducted herein confirm the importance of these parameters and suggest that they not only affect member response, but can also influence the collapse modes of SMFs. For example, by replacing first-story exterior columns in the TGL3 four-story frame (i.e. $P_g/P_y = 0.27$) with a stockier section (i.e. lower h/t_w and L/r_y), the frame collapse capacity is significantly enhanced (median values of $S_{a,C}$ and $SDR_{max,C}$ are increased by 34% and 76%, respectively) and the dominant collapse mode is shifted to sidesway collapse from vertical collapse. Similar observations can be made for the eight-story frame.

- The level of gravity load significantly influences the robustness of SMFs and their probability of collapse. For the particular four-story frame studied in this work, axial loads of $0.2P_y$ in first-story exterior columns appear to be a transition point between responses dominated by sidesway and vertical collapse. Given that the former is a more ductile mechanism and preferable to the latter, it is suggested that the permissible level of gravity load should be limited for exterior columns. Further research including a broader range of frames is necessary to select feasible values for a more general axial load limit.

- Comparing the performance of S4-L1-T3-C1 to S4-L2-T3-C1 suggests that additional lateral bracing at the level of beam bottom flanges for beam-to-column connections moderately improves the collapse capacity of SMFs (e.g. from 0.42g to 0.50g for $\tilde{S}_{a,C}$ when P_g/P_y = 0.27) and reduces the probability of vertical collapse from eleven to eight of the eleven records. As a result, it seems prudent to recommend that beam-column connections in SMFs should be braced at both the top and bottom of the beam flanges, regardless of the column-beam moment ratios at the connection.

- Frames with similar column shortening have quite different collapse behaviors suggesting that column shortening, in itself, does not play a direct role in collapse response. It is merely a consequence of local buckling. Excessive local buckling can be detrimental because it can reduce column end restraint, which can compromise column axial resistance and increase the potential for system collapse as the axial load demand increases. Local buckling can be controlled by limiting the element slenderness ratios and axial load demand.

CHAPTER 5

EFFECT OF SEISMIC DESIGN EVOLUTION ON RESILIENCE OF STEEL MOMENT FRAMES

5.1 General

This chapter systematically investigates how the evolution of seismic design provisions has changed seismic resilience of steel moment frame systems over the past half century. A thorough review of seismic design criteria and design practices is conducted to identify major differences in seismic provisions during the past fifty years due to enhancements proposed by researchers and engineers (Section 5.3 and 5.4). Three representative eras are selected based on the identified differences, and a set of steel perimeter moment frames with two-, four-, and eight-stories are designed for the selected eras (Section 5.5). High-fidelity frame models capable of explicitly capturing instabilities and fracture are developed using available experimental data (Section 5.6) and employed to determine the effect of the major design differences on seismic resilience of the frames using FEMA P-58 methodology (Section 5.7). The assessment results are used to propose strategies for improving the seismic resilience of communities with steel buildings (Section 5.8).

5.2 Motivation

Seismic design practices for buildings have experienced substantial changes over the past half century. Major changes to seismic codes typically happen in response to unexpected building damage as a result of earthquake events with the intent of achieving better building performance

during future events (SEAOC Seismology Committee 2006). For example, after the 1971 San Fernando earthquake, the number of seismic zones was increased from four to five and a coefficient, *S*, accounting for the effect of soil-structure interaction was introduced, leading to a better characterization of the seismic demands on buildings. After the 1985 Mexico City earthquake, requirements for irregular structures and building separation were added to the codes to ensure a more accurate strength distribution and to avoid pounding. Additional changes were made in the 1990s to consider soil liquefaction and near-fault effects due to the widespread ground failure and significant damage around the epicenter of the 1994 Northridge earthquake.

As with other types of construction, seismic design provisions for steel moment resisting frames (MRF) have evolved substantially during the past fifty years. MRFs have been widely used in areas of high seismicity for decades because of their architectural flexibility, large strength to weight ratio, and considerable ductility. The evolution of provisions for MRFs can be roughly split into three eras (Uang and Bruneau 2018): (1) prior to 1988; (2) 1988 - 1997; and (3) 1997 – present. The first era corresponds to early seismic practices. The second era incorporates lessons learned during the 1985 Mexico City earthquake, while the last era integrated knowledge gleaned from the 1994 Northridge earthquake.

It is naturally expected that steel buildings designed according to newer codes should have progressively better seismic performance than those designed to older codes. While many studies that have investigated how buildings designed in different eras have performed (e.g. FEMA 2010), it is difficult to confirm this expectation because the studies used different frame configurations and were done using computational tools with differing capabilities. To address these shortcomings, this study employs a set of moment frames designed with the same building configuration and site conditions to investigate how building codes influence seismic collapse

capacity and resilience of steel moment frames. High fidelity models of frames are developed to be capable of explicitly capturing instabilities and fracture to determine the effect of differences in the frame designs.

5.3 Evolution of Seismic Design Criteria for Steel MRFs

5.3.1 Seismic Design Forces

Prior to the 1960s, the seismic design force (a laterally applied load) was simply a function of the number of building stories and seismic zone where the building was located. Starting with the 1961 Uniform Building Code (UBC), (ICBO 1961), the spectral shape used to compute the design force became a function of fundamental vibration period (T_1) of the building. The applied force also was adjusted by other coefficients including the system factor in the 1961 UBC and soil profile coefficient in the 1976 UBC (ICBO 1976).

The spectral shape evolved as a function of the fundamental period, T_1. Functions in the form $1/{T_1}^{1/3}$, $1/{T_1}^{1/2}$, $1/{T_1}^{2/3}$, and $1/T_1$, were used in the 1961 UBC, 1976 UBC, 1988 UBC (ICBO 1988), and 1997 UBC (ICBO 1997), respectively. An upper limit on T_1 was not imposed until the 1988 UBC. In addition to the changes in spectral shape, the number of seismic zones, which are used to determine the magnitude of spectral shape, increased from four to five in the 1976 UBC then to six in the 1988 UBC. The concept of numbered zones was eventually replaced with seismic hazard contour maps starting with the 1998 version of ASCE 7 (ASCE 1998).

The effect of the soil profile at a building site on the design seismic force was first recognized in the 1976 UBC using equations representing soil-structure interaction. In the 1988 UBC, the equations were replaced with four site coefficients (S_1 to S_4) that depended on the soil properties:

the softer the soil, the larger the seismic demand on the building. These coefficients were eventually replaced with a set of earthquake-level dependent site classes (*A* to *F*) starting with the 1997 UBC.

The system factor (*K*) was used in the 1961 UBC to consider the effect of system ductility for four types of structural systems. The 1967 UBC (ICBO 1967) introduced ductile moment resisting space frames and specified additional requirements for buildings in high seismic areas. In the 1988 UBC, the system factor was succeeded by the response modification factor (R_w) and the number of structural systems increased to 29. Special moment frames were also introduced at this time along with special detailing, as described later. The R_w factor was replaced with *R* factor, which approximately equals to $R_w/1.4$, in the 1997 UBC because of the conversion from working stress design to strength design (SEAOC 2006). The number of structural types was increased to 41 in the 1997 UBC and 82 in the ASCE 7-05 (ASCE 2005).

Figure 5-1 shows a comparison of the equivalent static lateral forces as specified by different codes for steel moment frames (ductile or special) located in Santa Monica (34.000, -118.450). The site class is assumed to be *D* in the ASCE 7-05, which approximately corresponds to soil profile type S_2 in older codes (Dobry et al. 2000). The importance factor is assumed to be 1.0. While Figure 5-1 suggests that newer codes generally require larger seismic design forces, the ASCE 7-05 uses of a smaller response modification factor (i.e. *R*) due to the implementation of strength design. As a result, all codes have similar requirements of seismic demand on steel moment frames with slight differences due to the adoption of different spectral shapes and minimum required forces except the 1961 UBC that had a lower estimation of seismic hazard at this particular site.

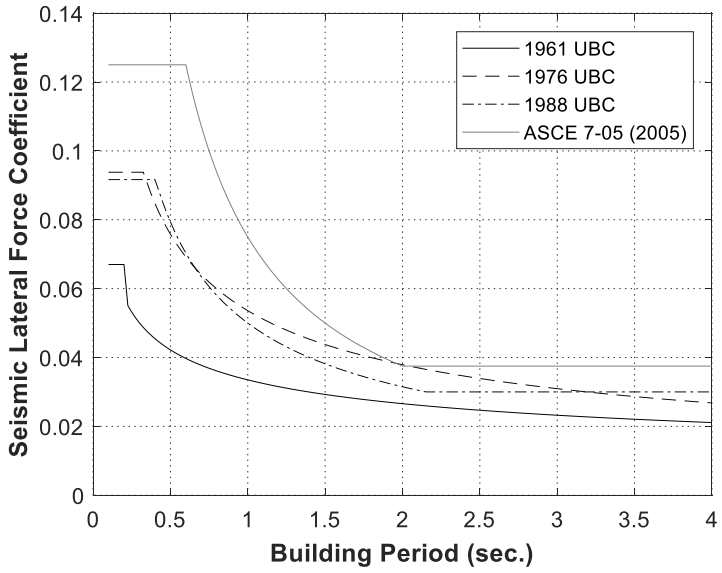

Figure 5-1. The minimum seismic lateral force required in different editions of the building codes

5.3.2 Design Principles of Steel Moment Frames

The 1961 UBC defined a moment resisting space frame as one able to resist 100% of a building's lateral force and that had a system factor $K = 0.67$. In 1967, a new term "ductile moment resisting space frame" was introduced to differentiate between frames with different levels of ductility. According to the 1970 UBC (ICBO 1970), these frames had: (1) moment connections capable of developing the full plastic capacity of the beams and (2) minimum slenderness ratios in plastic hinge zones to control local buckling. The 1988 UBC addressed "special moment resisting frames" for the first time and had a section specifying detailing requirements for this type of system, which is currently used in seismic zones worldwide. The term "special" implied compliance with criteria for (1) the strong-column/weak-beam (SCWB) design principle, (2) a specific panel zone design philosophy, and (3) stability bracing.

5.3.2.1 Strong-Column/Weak-Beam (SCWB) Design Principle

The purpose of the SCWB principle is to control inelasticity in columns and retain structural stability, while dissipating energy through beam yielding. This principle is achieved by requiring a flexural strength that is higher for columns than for beams for any moment connection, as stated in the 1988 UBC:

$$\sum Z_c \left(F_{yc} - P_{ac}/A_g\right) / \sum Z_b F_{yb} > 1.0 \qquad (5\text{-}1)$$

where Z_c and Z_b (or Z_{RBS} if reduced beam sections are used) are the plastic section modulus of the columns and beams, respectively, F_{yc} and F_{yb} are the specified minimum yield stress of the columns and beams, respectively, and P_{ac} is the required compressive strength using the allowable stress design (ASD) load combinations. As can be seen in Equation (5-1), material over-strength was not considered. This was a weakness of past seismic provisions because material overstrength was identified as one of the major issues in the 1994 Northridge earthquake. Equation (5-1) was subsequently modified in the 1997 AISC seismic provisions:

$$\sum Z_c \left(F_{yc} - P_{uc}/A_g\right) / \sum 1.1 R_y Z_b F_{yb} + M_{uv} > 1.0 \qquad (5\text{-}2)$$

where P_{uc} is the required compressive strength using LRFD load combinations, R_y is the ratio of the expected yield stress to the specified minimum yield stress, and M_{uv} is the additional moment due to shear amplification from the location of the plastic hinge to the column centerline, based on LRFD load combinations. The principle became even more stringent with the 2010 AISC seismic provisions (AISC 2010) as P_{uc} had to include the amplified seismic load.

In addition to the requirement for the ratio between flexural strength of columns and beams, the 1988 UBC had additional requirements on the column axial strength to address column failures observed in the 1985 Mexico City earthquake. After 1988, the columns were required to resist the estimated maximum axial force under extreme seismic events by considering the amplified seismic load in the design load combinations.

5.3.2.2 Panel Zone Design Philosophy

Panel zone design philosophy evolved considerably over the years. Prior to 1988, panel zones were designed to remain elastic during seismic events, i.e. a "strong panel zone". In this context, "strong" refers to the fact that the panel zones are stronger than the connecting beams, which mainly contribute to energy dissipation in this approach. As specified in the 1985 UBC, the shear strength of panel zones should be capable of developing the full plastic capacity of the beams:

$$0.55F_{yc}d_c t_p \geq \frac{Z_b F_{yb}}{0.95d_b} \tag{5-3}$$

where d_c and d_b is the depth of the columns and beams, respectively, and t_p is the thickness of the panel zone. The strong panel zone requirement was replaced in the 1988 UBC with a diametrically opposite approach: a weak panel zone, designed to allow most of energy dissipation to occur in the panel zones. This shift was based on findings from extensive research conducted since the 1970's (Krawinkler et al. 1975):

$$0.55F_{yc}d_c t_p\left(1+\frac{3b_c t_{cf}^2}{d_b d_c t_p}\right) \geq \frac{\min\left(M_g + 1.85M_e, 0.8Z_b F_{yb}\right)}{d_b - t_{bf}} \tag{5-4}$$

where b_c and t_{cf} are the width and thickness of the column flange, respectively, t_{bf} is the thickness of the beam flange, M_g and M_e are beam bending moments due to gravity loads and seismic forces,

respectively. Weak panel zones, however, proved problematic during the 1994 Northridge earthquake. The kink in the column flanges that resulted from excessive panel zone distortion was widely thought to be one of the reasons for the widespread connection failures that occurred during that event. This outcome led to the development and specification of a new approach: "balanced panel zone design", which first appeared in the 2002 AISC seismic provisions (AISC 2002). This new approach focused on sharing inelastic behavior between panel zones and beams:

$$0.60F_{yc}d_c t_p\left(1+\frac{3b_c t_{cf}^2}{d_b d_c t_p}\right) \geq \frac{1.1R_y F_{yb} Z_{RBS} + M_{uv}}{d_b - t_{bf}} \qquad (5\text{-}5)$$

5.3.2.3 Stability Bracing

It was not until in the 1988 UBC, column flanges at beam-to-column connections had to be laterally braced at the top and bottom beam flanges unless the column remained elastic. In such cases, lateral bracing had to be provided at only the top beam flanges. In the 1988 UBC, columns were assumed to remain elastic when the ratio in Equation (5-1) was greater than 1.25. This sufficient condition became much stricter in the 2002 AISC seismic provisions as the ratio in Equation (5-2) needed to be greater than 2. Beam bracing criteria also evolved. Beam flanges were required to be laterally supported with a maximum unbraced length (L_b) of $96r_y$ in the 1988 UBC, where r_y is the radius of gyration about the minor axis. In the 1990 AISC provisions (AISC 1990), L_b was decreased to $2500\ r_y/F_{yb}$, a value that has been used since.

5.4 Evolution of Practices for Steel MRFs

In addition to the changes in design criteria, design practices also evolved, influenced by developments in manufacturing and construction technology and a push to minimize design effort

and construction costs. Key changes occurred in the properties of structural steel, type of connections and structural systems, and column section selection.

5.4.1 Material Properties

As can be seen in Figure 5-2, steel material strength has increased significantly since the 1940s, when mild structural steel was sold as A7 steel with a specified minimum yield stress F_y = 228 MPa (Roeder 2000). Starting in 1961, A36 steel with F_y = 248 MPa was incorporated in the AISC specification (AISC 1961) and dominated the market until around the 1994 Northridge earthquake. A572 Grade 50 steel with F_y=345 MPa, which was also a popular option, was sold after the 1969 AISC specification (AISC 1969). A36 steel fell out of favor because its actual yield strength was much higher than its nominal yield strength due to the use of recycled scrap steel, as can be seen in Figure 5-2. This increase in strength changed the seismic performance of structures, leading to the adoption in the late 1990s of A992 steel with F_y = 345 MPa (50 ksi). A992 steel became widely used because its yield to ultimate strength ratio was constrained.

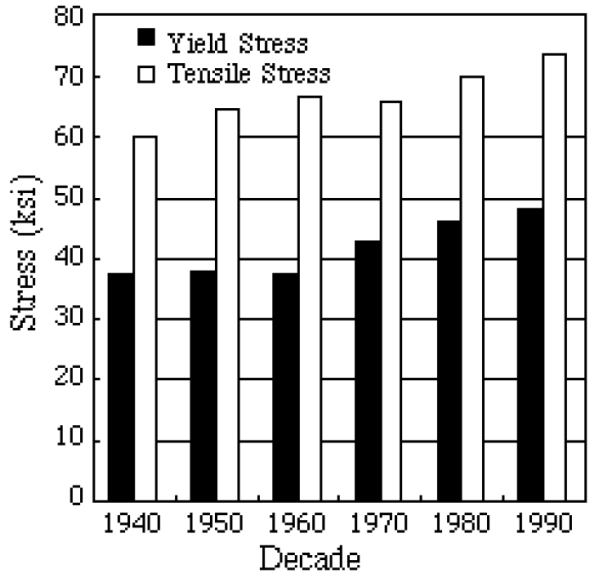

Figure 5-2. Variation in the measured strength properties of structural steel (Coons, 1999)

5.4.2 Connection Types

Connection types as well as weld details changed significantly after the 1994 Northridge earthquake. These changes were documented in the FEMA 350 series of documents (FEMA 2000). Unlike the welded-flange-bolted-web (WFBW) connections, i.e. pre-Northridge connections from the 1970s, post-Northridge connections incorporated recommendations to avoid early brittle fracture in welds and provide sufficient plastic rotational capacity. Key requirements pertained to the use of filler metal with sufficient Charpy V-Notch (CVN) toughness, removal of the bottom weld backing bar, improved geometry of the weld access hole, and new connection types other than WFBW connections. The most popular type of post-Northridge connection is the reduced-beam-section connection (RBS). This connection type enables beams to yield in the reduced area located at a distance from the column face to reduce the demands on beam-column welds and protect the connection.

5.4.3 Structural Systems and Column Section Selection

Significant changes in the structural system for steel buildings occurred around the mid-1970s. Before the mid-1970s, most of the connections in steel buildings were moment connections. A drawback to these connections is the cost of fabrication and erection. In particular, field welded moment connections are expensive to construct. In a quest to reduce the number of field welded moment connection, and hence reduce overall construction costs, structural practice evolved toward perimeter moment frames, where only a few frames with a few bays are used for seismic resistance. The concentration of lateral force resistance on perimeter moment frames resulted in both lower structural redundancy and the use of heavier structural members for the moment frames. Coupled with the stringent design provisions developed after the 1994 Northridge earthquake,

current practice evolved towards selecting deep, wide flange columns instead of the W14 sections commonly used in frames before the Northridge earthquake (Elkady and Lignos 2015a; Ozkula et al. 2017b; Wu et al. 2018a, 2018b).

5.5 Representative Steel Moment Frames

Three eras that can represent the major differences in seismic design and practices are chosen to study the effect of the design evolution over the past century: mid-1970s, early 1990s, and mid-2000s. The early 1990s and mid-2000s are selected to represent the design prior to the 1994 Northridge earthquake, which caused significant changes in the detailing of special moment frames, including material properties, welding practices, connection types, and panel zone design philosophy. The mid-1970s is chosen because during this era, the lateral force was calculated simply as a function of the seismic zone (Z), the system factor (K), and the fundamental vibration period (T_1), without consideration of the soil profile effect. Specifically, there was no upper limit on estimation of fundamental period (T_1), which combined with the vague drift requirement at the time can result in a design of a building with very high lateral flexibility.

A set of steel perimeter moment frames with two-, four-, and eight-stories are designed per seismic design codes and practices for the three selected eras. The designs are for an office building configuration described in NIST (2010), as shown in plan in Figure 3-1(a) and with the site condition used to plot Figure 5-1. The eras are designated E75 (for mid-1970s designs), E90 (for early 1990s design), and E05 (for mid-2000s design) to facilitate referral to them. The frames are designated S2, S4, and S8 where the appended number is the number of stories.

E05 frames are designed with RBS connections and W24 columns (i.e. deep columns) using A992 steel, while the older frames employ WFBW connections and W14 columns with A36 and A572

Grade 50 steel for beams and columns, respectively. The yield strength of the A36 steel used in E75 and E90 frames is 296 MPa (43 ksi) and 338 MPa (49 ksi), respectively, based on the survey in Figure 5-2. The major differences in seismic design and practices among the eras are summarized in Table 5-1, and the main characteristics of the designed frames are listed in Table 5-2. Full frame designs are shown in Figure 5-3 to Figure 5-5 with the employed beam and column sections. Note that a drift limit of 0.5% in the 1976 UBC is applied to E75 designs, but without the system factor modification. In addition, the design of the frames in this study aims to satisfy the minimum requirements specified in the building codes, although structural engineers might have a more conservative design in practice.

Table 5-1. Summary of major differences of the seismic design and practice between the three studied eras

Design Era	mid-1970s (E75)	early 1990s (E90)	mid-2000s (E05)
Frame Type	Perimeter Ductile MRF	Perimeter Special MRF	Perimeter Special MRF
Connection Type	WFBW	WFBW with supplemental web welds	RBS
Material	A36 (beams, F_y = 296 MPa) A572 Grade 50 (columns)	A36 (beams, F_y = 338 MPa) A572 Grade 50 (columns)	A992
Design Codes	1969 AISC and 1973 UBC	1989 AISC ASD and 1991 UBC	AISC 360-05 (LRFD), AISC 341-05, AISC 358-05, and ASCE 7-05
Drift Limit	0.5%	0.25%	0.45%
SWCB Principle	N.A.	Equation (5-1)	Equation (5-2)
Panel Zone Design	Strong: Equation (5-3)	Weak: Equation (5-4)	Balanced: Equation (5-5)
Lateral Bracing for B/C Connections	Only at level of top beam flanges	At levels of both beam flanges except for Equation (1) > 1.25	At levels of both beam flanges except for Equation (2) > 2.0
Lateral Bracing for Beams	Only for top beam flanges	$L_b = 96r_y$	$L_b = 2500\ r_y/F_{yb}$
Column Compressive Strength	N.A.	$1.0P_D + 0.7P_L + 4.5P_E$	$1.2P_D + 0.5P_L + 3P_E$

*P_D, P_L, and P_E: axial loads due to dead load, live load, and seismic loads, respectively.

Table 5-2. Characteristics and collapse analysis results of representative steel moment frames

Frame ID	Design Era	1st-story Column Section	1st-floor Beam Section	Steel Weights (kN)	T_1 (sec.)	$\widehat{\boldsymbol{S}}_{a,C}(\boldsymbol{T_1}, \mathbf{5\%})$ (g)	β	λ_c	$P_{c,50yrs}$
2-story									
S2-E75	mid-1970s	W14×74	W21×50	59.2	1.30	0.65	0.47	1.40e-3	6.78%
S2-E90	early 1990s	W14×82	W24×62	68.5	1.18	0.78	0.48	1.17e-3	5.69%
S2-E05	mid-2000s	W24×76	W21×44	59.2	1.01	1.06	0.31	4.82e-4	2.38%
4-story									
S4-E75	mid-1970s	W14×82	W21×44	109	2.46	0.23	0.28	2.61e-3	12.3%
S4-E75-NF	mid-1970s	W14×82	W21×44	109	2.46	0.28	0.29	1.59e-3	7.67%
S4-E90	early 1990s	W14×132	W27×84	187	1.77	0.53	0.44	1.09e-3	5.29%
S4-E90-NF	early 1990s	W14×132	W27×84	187	1.77	0.61	0.45	7.73e-4	3.79%
S4-E05	mid-2000s	W24×103	W21×73	142	1.67	0.64	0.45	8.02e-4	3.93%
8-story									
S8-E75	mid-1970s	W14×145	W24×62	297	3.74	0.12	0.28	3.67e-3	16.8%
S8-E90	early 1990s	W14×211	W30×108	507	2.67	0.44	0.23	3.91e-4	1.94%
S8-E05	mid-2000s	W24×162	W30×108	428	2.37	0.54	0.31	3.57e-4	1.77%

*NF: Fracture in pre-Northridge connections is not modeled.

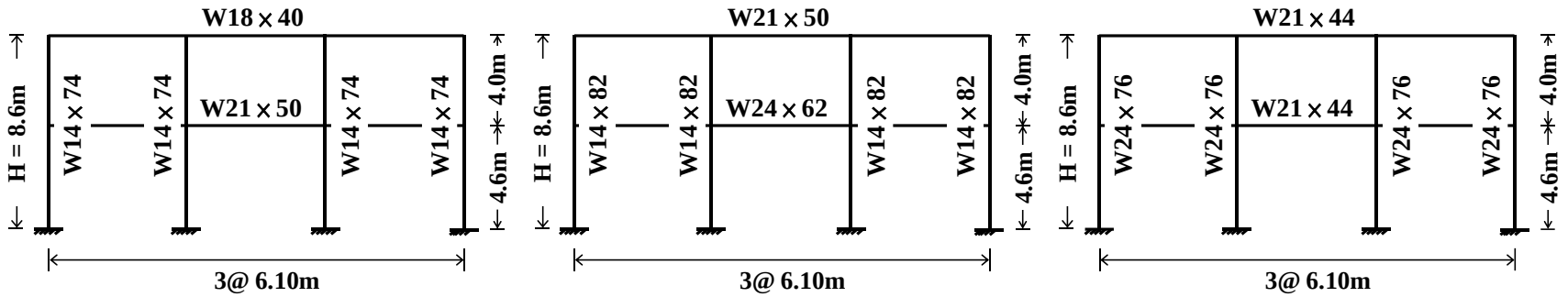

Figure 5-3. Elevation view of 2-story representative frames (a) S2-E75 frame; (b) S2-E90 frame; and (c) S2-E05 frame

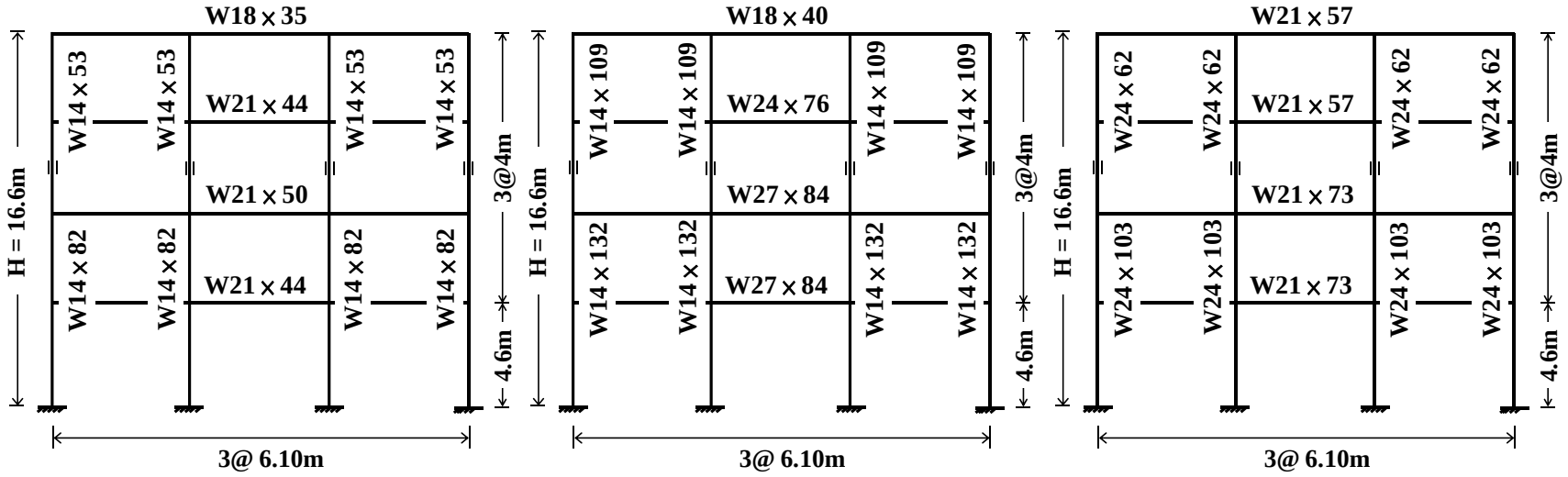

Figure 5-4. Elevation view of 4-story representative frames (a) S4-E75 frame; (b) S4-E90 frame; and (c) S4-E05 frame

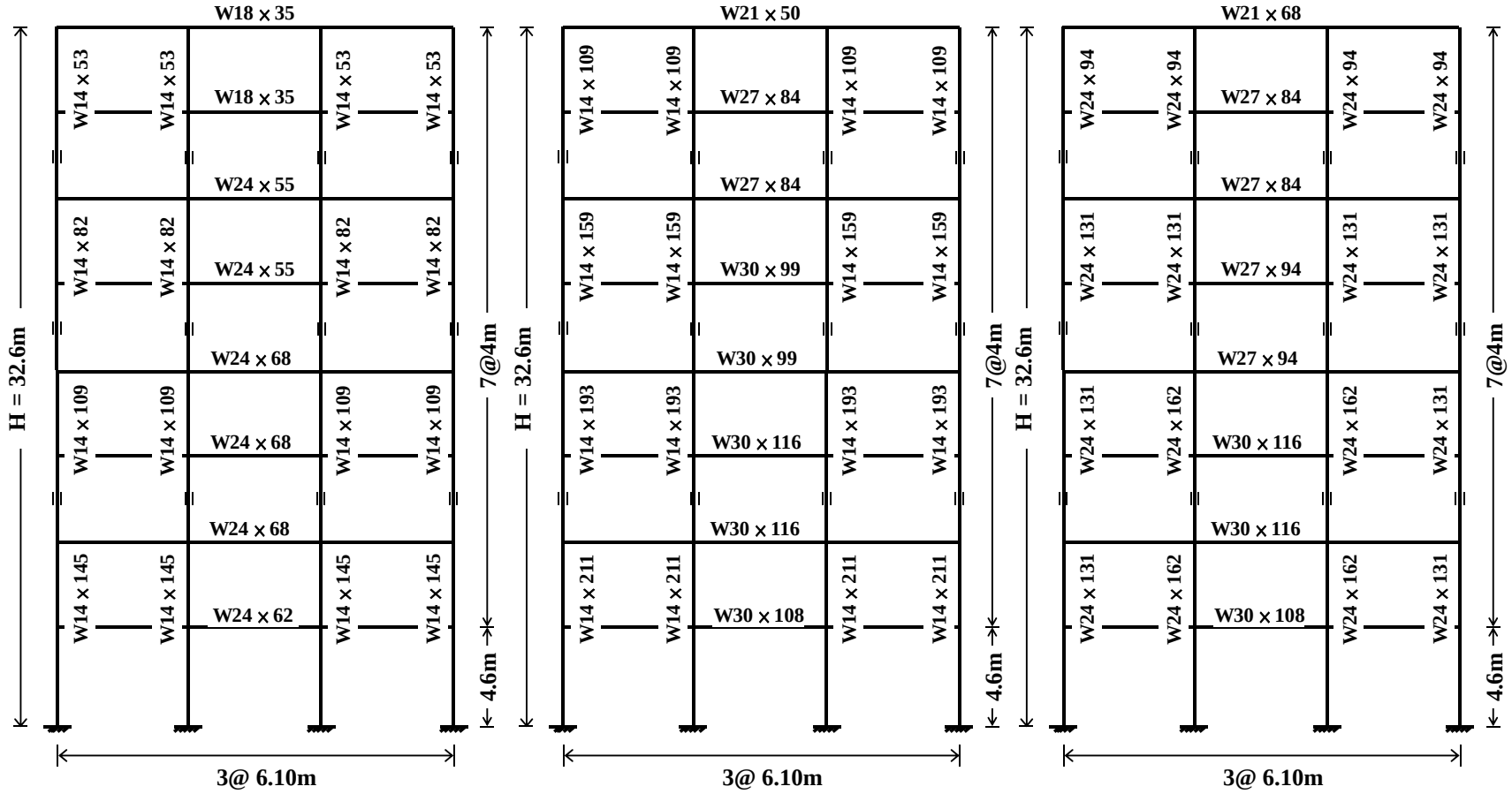

Figure 5-5. Elevation view of 8-story representative frames (a) S8-E75 frame; (b) S8-E90 frame; and (c) S8-E05 frame

5.6 Finite Element Modeling

5.6.1 Modeling Approach

Following Section 3.3.2, detailed finite element models (FEM) of the moment frames are created and analyzed using Hypermesh (2013) and the explicit solver implemented in LS-DYNA (2013), respectively, with the same element formulation, mesh size, and material model. The differences in the employed material model (MAT153) include (1) hardening moduli are calibrated using the steel material strength listed in Table 5-1 and (2) damage modeling is enabled to represent ultra-low cycle fatigue behavior in structural steel. The damage parameters are calibrated to the experimental data in Liu and Astaneh-Asl (2000) and Engelhardt and Husain (1992), as discussed later in Section 5.6.2.

The frame model with the leaning column and the details are the same as the one shown in Figure 4-4 and Figure 4-5, respectively, except that the discretization of welded flange-bolted web (WFBW) connections in the E75 and E90 is shown in Figure 5-6. Column flanges at the beam-to-column connections and beam flanges are laterally braced according to the requirements stipulated in the different eras, as listed in Table 5-1. All other modeling approaches are the same as described in Section 3.3.2.

As done in Section 4.5.2, two collapse criteria are used to detect sidesway collapse: (1) maximum story drift ratio surpasses 10% and (2) an increase of 2% or more in story drift ratio during the 10 second window immediately after the time needed for the Arias intensity to reach 95% ($t_{IA=95\%}$) (Arias 1970). Unlike sidesway collapse, vertical progressive collapse can be clearly identified from the deformed shape of the frame and no specific criteria are needed.

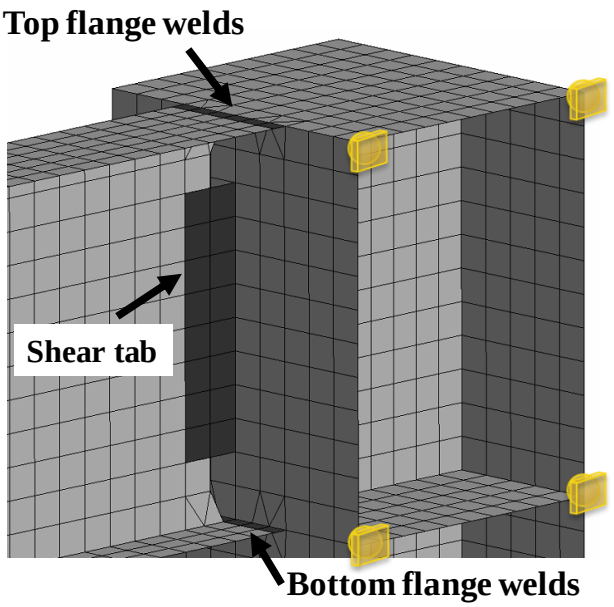

Figure 5-6. Discretization of welded flange-bolted web (WFBW) connections in finite element models of E75 and E90 frames

The finite-element models of the two-, four-, and eight-story frames consist of approximately 54,000, 110,000 and 240,000 elements, respectively. The simulations run on a cluster with 16 processors. The simulation time to model 30 sec of real time is about 18, 42, and 90 hours for the two-, four-, and eight-story frames, respectively. A total of 782 simulations are performed requiring about 6 months of run time.

5.6.2 Validation of Modeling Scheme and Calibration for Fracture Behavior

The general finite element modeling approach used in this study has been validated and detailed in Section 2.3 and 2.7.1. Additional calibration is sought because this study models the brittle fractures that occur in pre-Northridge connections. Unlike earlier efforts in the previous chapters where fracture usually occurs at extremely large drifts, the brittle connection failure in the pre-Northridge frames, i.e. E75 and E90 frames, can occur at a small drift of 1% to 2% and have a

great impact on frame responses. Parameters for brittle shear tab and beam flange weld fracture in the WFBW connections (see Figure 5-6) are calibrated to experimental data in Liu and Astaneh-Asl (2000) and Engelhardt and Husain (1992), respectively.

Liu and Astaneh-Asl (2000) tested sixteen steel beam-column subassemblages to study the cyclic behavior of typical shear connections with and without a slab. The specimens were cross-shaped subassemblages with cyclic loads applied at the column top. The structural members and connection plates were made with A572 Grade 50 and A36 steel, respectively. Specimen 2A, which utilized a typical strong-axis shear tab without a floor slab, is selected for calibrating the material model (MAT153) used for the shear tab in the moment connections. The specimen was subjected to symmetric cyclic drift loading as specified in the AISC seismic provisions (2002). Using a trial and error approach, the best calibration results are obtained when the material model is bilinear hardening, with F_y=124 MPa, tangent modulus (E_T) is 1% of the elastic modulus (E), and the critical damage value (D_c) is 0.5, as shown in Figure 5-7. It should be noted that these parameters represent the aggregate behavior of the shear tab, including the effect of bolts, and binding (contact between the beam and column flanges). The calibrated parameters are used to model the shear tabs in the E75 frames.

The parameters for modeling the beam flange welds and shear tabs in the E90 frames that have supplemental welds at the beam web connections are calibrated to the experimental data in Engelhardt and Husain (1992), who cyclically tested eight WFBW connections. The specimens were cantilever-type subassemblages with cyclic loads applied at the beam end. The beams and columns were made with A36 and A572 Grade 50 steel, respectively, and an E70 welding electrode was used for welding. Because the eight specimens showed highly variable performance, all

experimental results in the test program are utilized in the calibration to explore the range of D_c for beam flange welds. The calibrated results are shown in Figure 5-8 to Figure 5-10.

The calibration results suggest that MAT153 can still be used, but with a D_c of 0.025 to 0.04 (with an average of 0.034) and 0.002 to 0.037 (with an average of 0.021) to simulate the fracture behavior of top and bottom flange welds, respectively. The higher D_c for the top flange welds indicates better performance than the bottom flange and is consistent with the surveyed damage after the Northridge earthquake (Youssef et al. 1995). In spite of the large variability in D_c, which is expected given the brittle nature of the fractures, the average values are employed in the modeling scheme to represent the fracture response of the flange welds. Variability in D_c can be accounted for in future studies through a Monte Carlo-style study, for example.

Specimens 3 (Figure 5-8b) and 7 (Figure 5-10b) are used to calibrate the model for the shear tabs with supplemental web welds in the E90 frames. The calibration is identical to that for the Liu and Astaneh (2000) shear tabs, except for F_y, which is taken as 248 MPa (36 ksi).

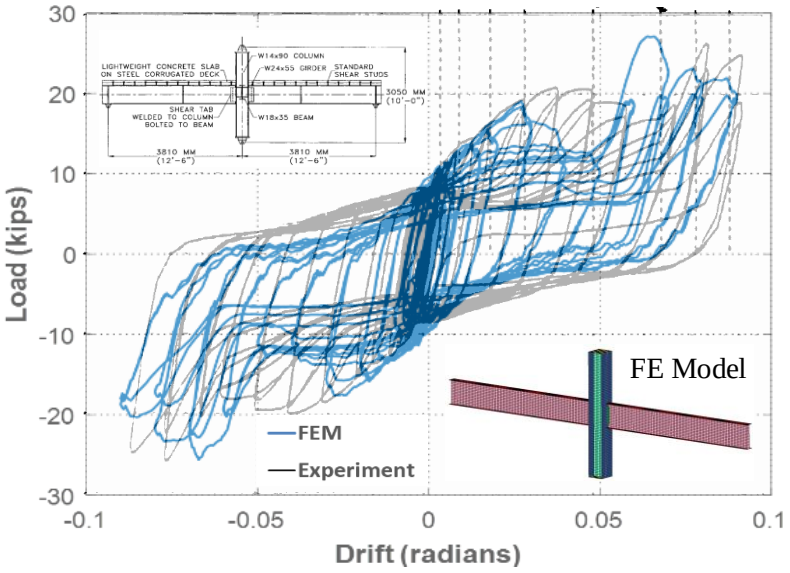

Figure 5-7. Fracture calibration results for the shear tab (Specimen 2A, Liu and Astaneh-Asl 2000)

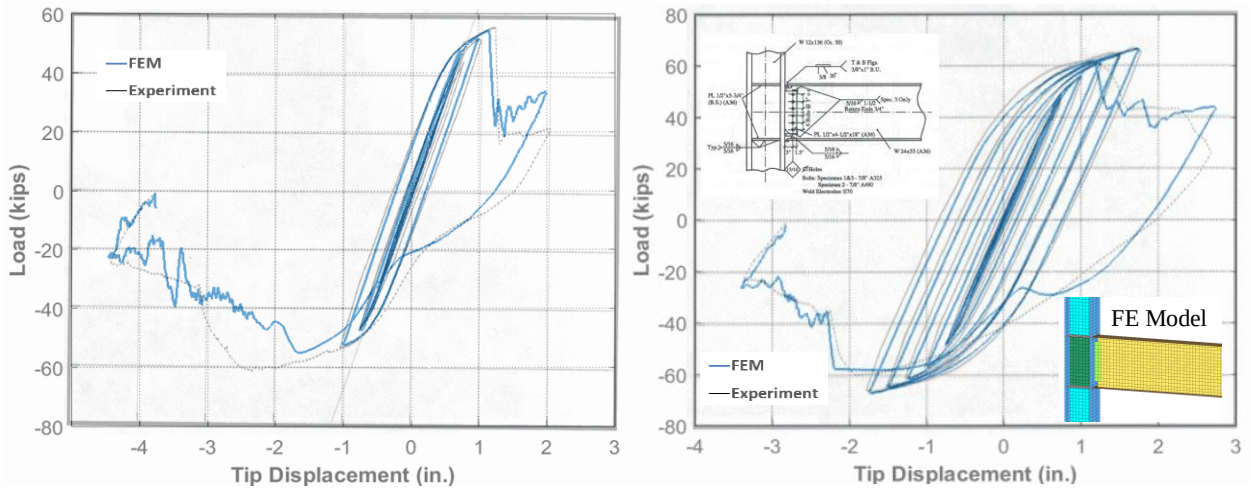

(a) (b)

Figure 5-8. Calibration results of flange welding of W24×55 beams tested in Engelhardt and Husain (1992). (a) Specimen 1 and (b) Specimen 3 (with supplemental web welds)

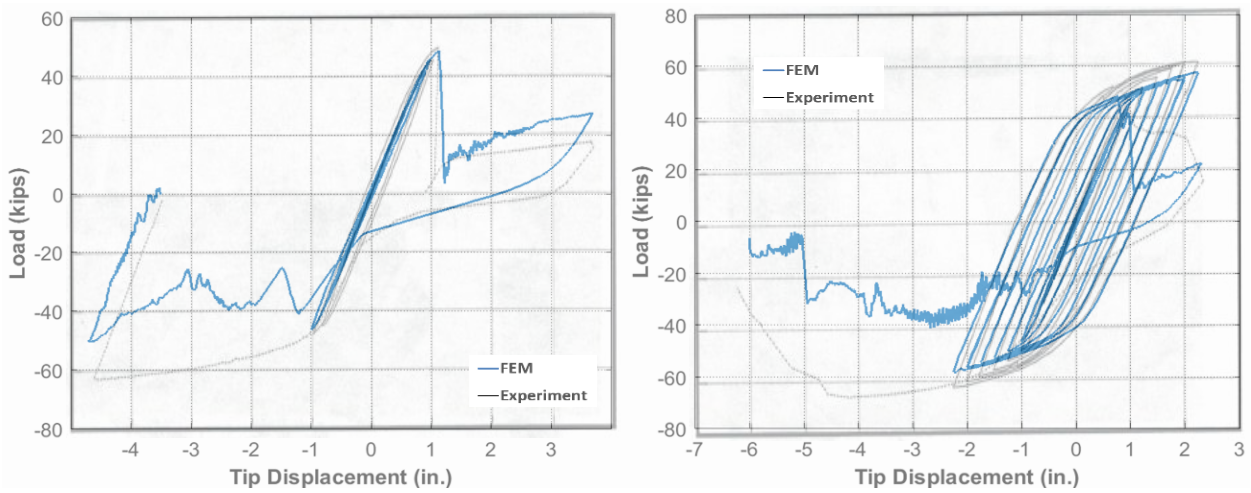

(a) (b)

Figure 5-9. Calibration results of flange welding of W18×60 beams tested in Engelhardt and Husain (1992). (a) Specimen 4 and (b) Specimen 5

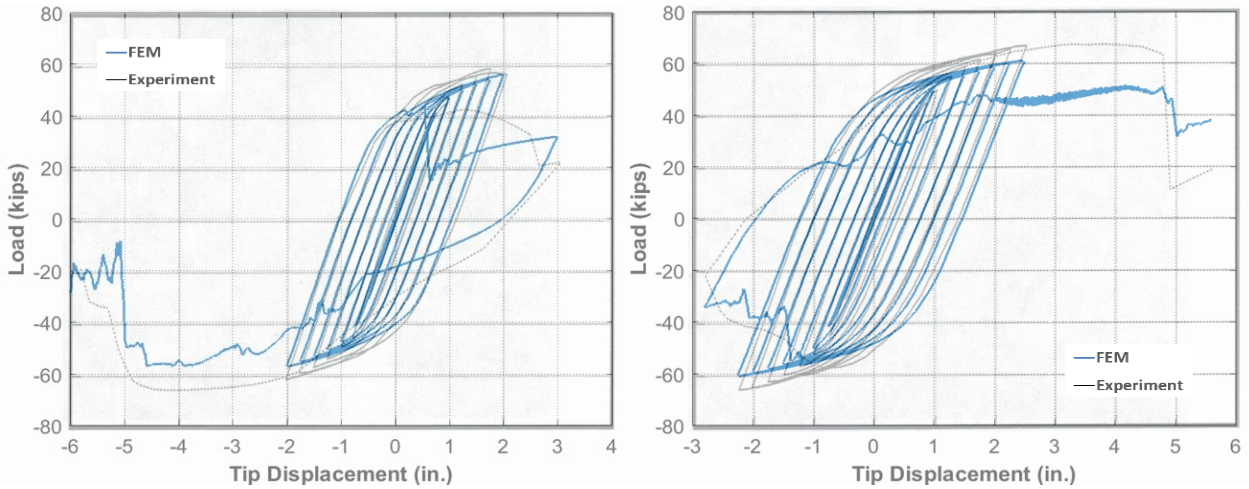

(a) (b)

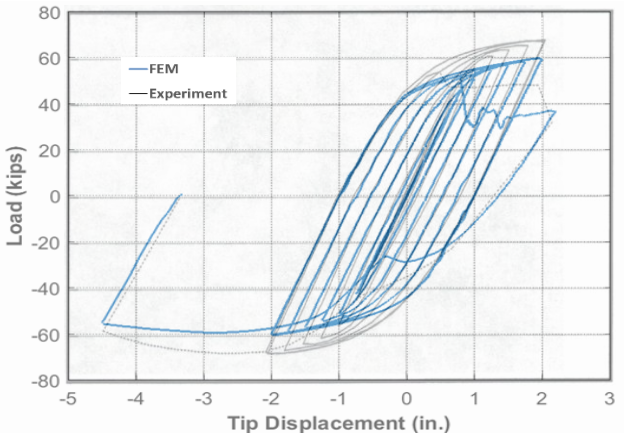

(c)

Figure 5-10. Calibration results of flange welding of W21×57 beams tested in Engelhardt and Husain (1992). (a) Specimen 6; (b) Specimen 7 (with supplemental web welds); and (c) Specimen 8 (with full web welds)

5.7 Simulation Results

Resilience assessment of the moment frames (listed in Table 5-2) is performed using the SP3 loss estimation software (Haselton Baker Risk Group 2019), which is based on the FEMA P-58 (2012) methodology. The data required for the assessment, including collapse fragilities of the moment

frames and building demands under earthquakes with a given intensity level, are obtained through detailed finite element analysis using the modeling scheme described above.

Figure 5-11 to Figure 5-13 shows common damage modes and collapse mechanisms of moment frames designed for different eras. The S4-E75 and S4-E90 frames mostly fail by a multi-story sidesway mechanism (Figure 5-11a and Figure 5-12a), while the S4-E05 frame is more likely to collapse by a first-story mechanism due to instability of the deep columns (Figure 5-13a). It can be also seen from Figure 5-11(b) and Figure 5-12(b) that the pre-Northridge connections suffer from brittle weld fracture and deteriorate beam moment capacity, which is slightly mitigated by the binding between column and beam flanges. On the other hand, the reduced beam sections in the S4-E05 frame can develop plastic hinges at the reduced region (Figure 5-13b). The difference in panel zone behavior due to different design philosophy can be also observed from Figure 5-11(b) to Figure 5-13(b), e.g. the kink in the column flanges due to the weak panel zone (Figure 5-12b). It is clear that the employed finite element analysis effectively captures key aspects of the designs, e.g. panel zone design philosophy, brittle fracture in pre-Northridge connections, and global buckling of deep columns.

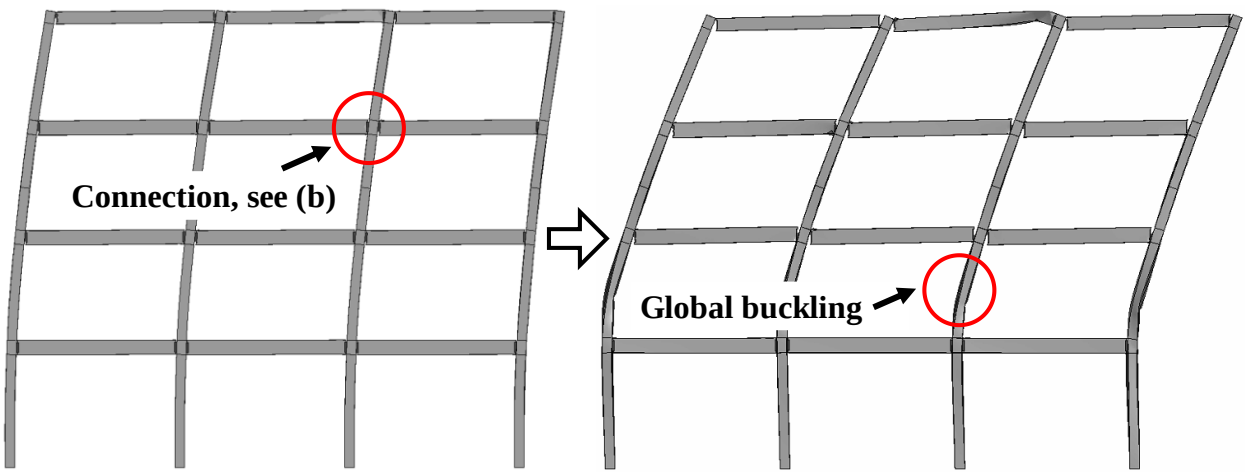

(a)

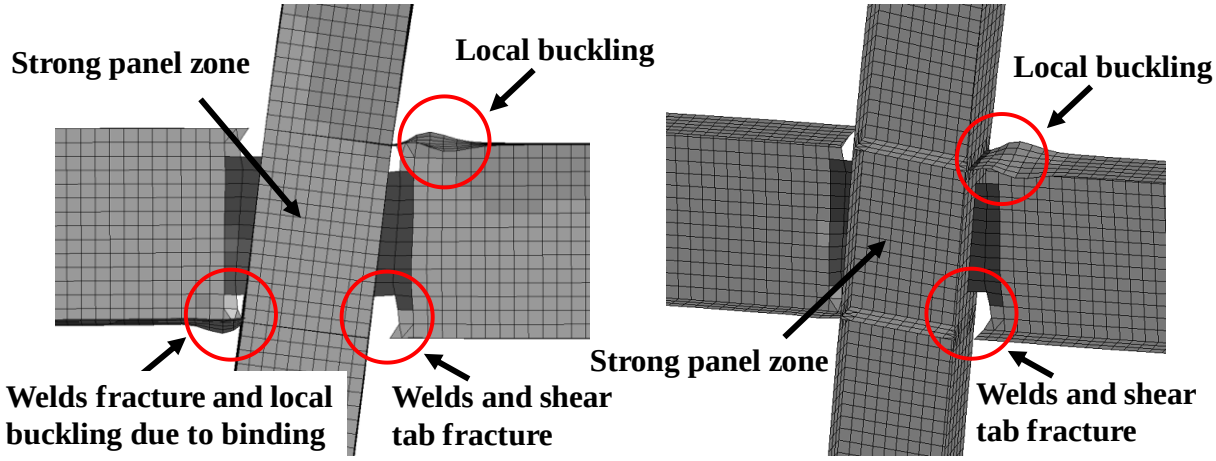

(b)

Figure 5-11. S4-E75 frame subject to Northr/MUL009 record with $S_a(T_1, 5\%) = 0.31g$. (a) multi-story sidesway collapse mechanism and (b) damage at the WFBW connections

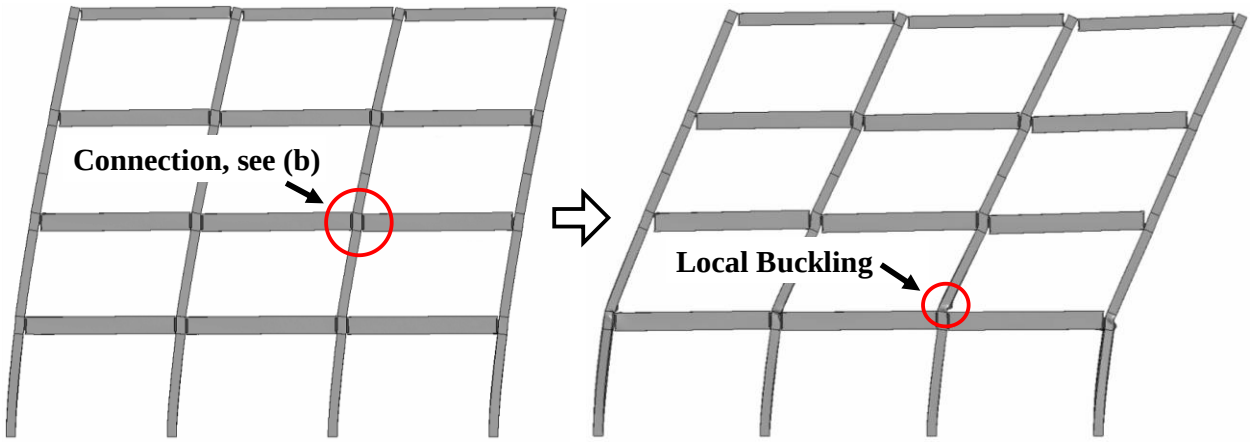

(a)

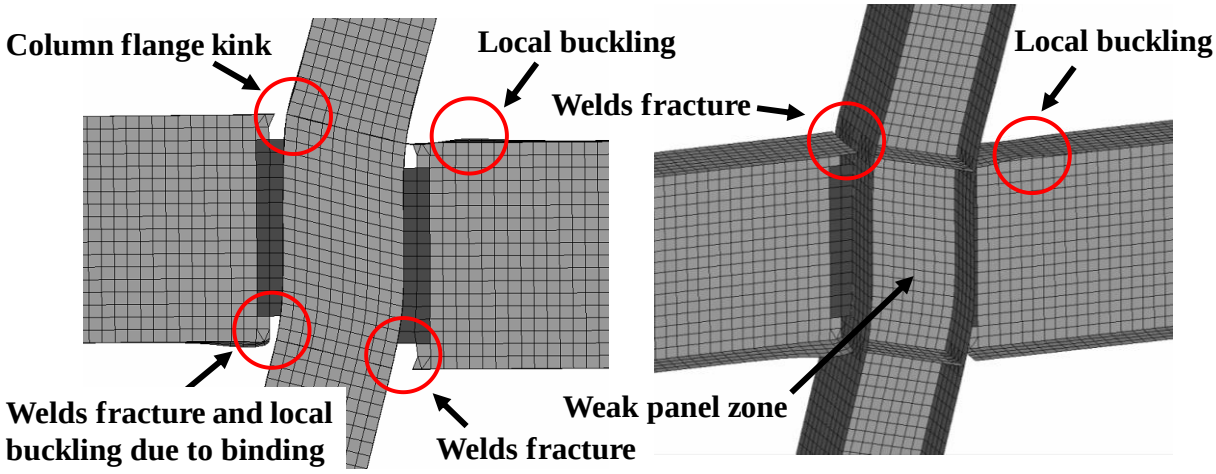

(b)

Figure 5-12. S4-E90 frame subject to Impvall/H-DLT262 record with $S_a(T_1, 5\%) = 0.47g$. (a) multi-story sidesway collapse mechanism and (b) damage at the WFBW connections

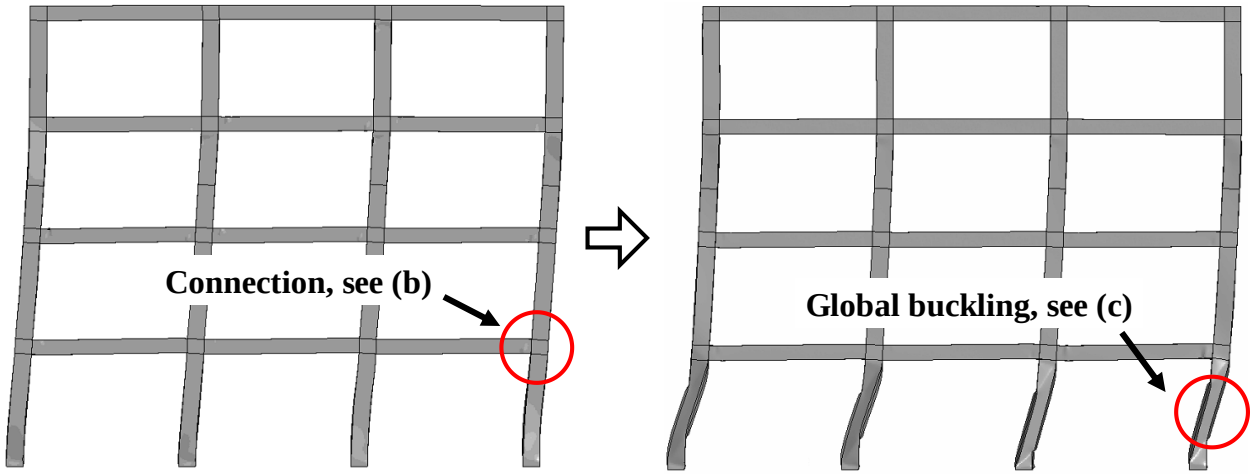

(a)

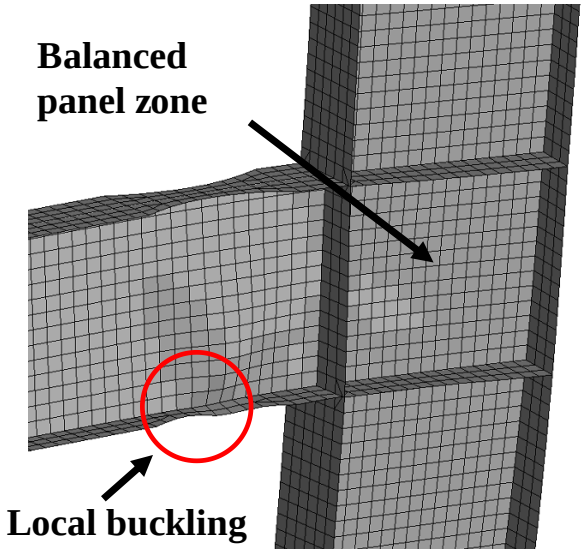

(b)

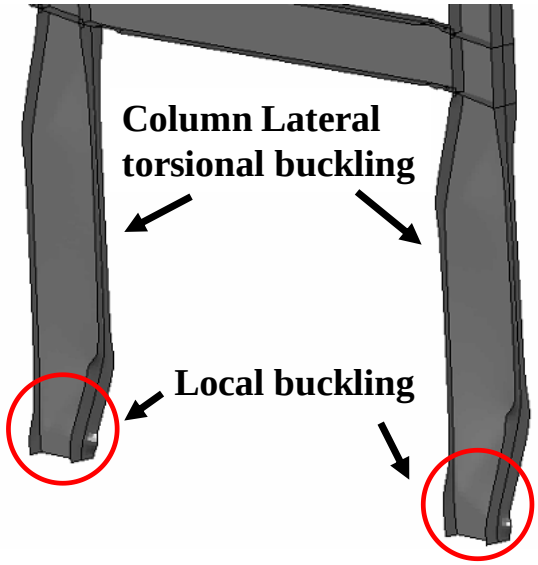

(c)

Figure 5-13. S4-E05 frame subject to Hector/HEC000 record with $S_a(T_1, 5\%) = 0.95g$. (a) first-story sidesway collapse mechanism; (b) local buckling at RBS connections; and (c) local and global instability of deep columns

5.7.1 Collapse Capacity

The collapse fragility analyses are based on eleven ground motion records selected from the Far-Field record set in FEMA P695 (2009) and listed in Table 3-1. As explained in Section 4.6, only

eleven records are used instead of the eleven pairs (i.e. 22 records) recommended in FEMA P-58 (2012) as a compromise between computational expediency and the need to adequately capture ground motion variability. The spectral acceleration associated with collapse ($S_{a,C}(T_1, 5\%)$) of each record is then obtained by incremental dynamic analysis (IDA) (Vamvatsikos and Cornell 2002), when one of the collapse criteria is met under the scaled record. The obtained $S_{a,C}(T_1, 5\%)$ values are fitted to a lognormal distribution using the Collapse Fragility Tool provided in FEMA P-58 (2012) to determine the collapse fragility curve for each moment frame. Each curve is characterized by a median value of $S_{a,C}$, $\hat{S}_{\mathrm{a,C}}$ and dispersion, β. The mean annual frequency of collapse (λ_c) of each moment frame is computed by numerically integrating its collapse fragility curve with the seismic hazard curve associated with the site condition from USGS (2018). The collapse probability over a time frame of 50 years, $P_{c,50yrs}$, for each frame is also computed by assuming a Poisson distribution. The analysis results are summarized in Table 5-2, and the collapse fragility curves of the frames are plotted in Figure 5-14 to Figure 5-16.

Table 5-2 shows that the collapse risk decreases as the seismic design codes evolved. Specifically, the E05 frames have a lower $P_{c,50yrs}$ than the corresponding E90 and E75 frames, regardless of building height. Although the E90 frames use more steel than the corresponding E05 frames (e.g. S4-E90 uses 32% more steel than S4-E05), primarily due to the use of stocky W14 sections, they have a higher collapse risk. This reflects the fact that the newest generation of codes and their associated practices are more efficient. On the other hand, the E75 frames are the set of frames using the least steel. However, these frames also have the highest collapse risk. The high collapse risk is primarily attributed to the fact that there is no cap on the fundamental period used in design. The lack of a bound on the period results in smaller section sizes, greater susceptibility to P-Delta effects, and greater vulnerability to sidesway collapse at smaller drifts, in the range of 4-5%.

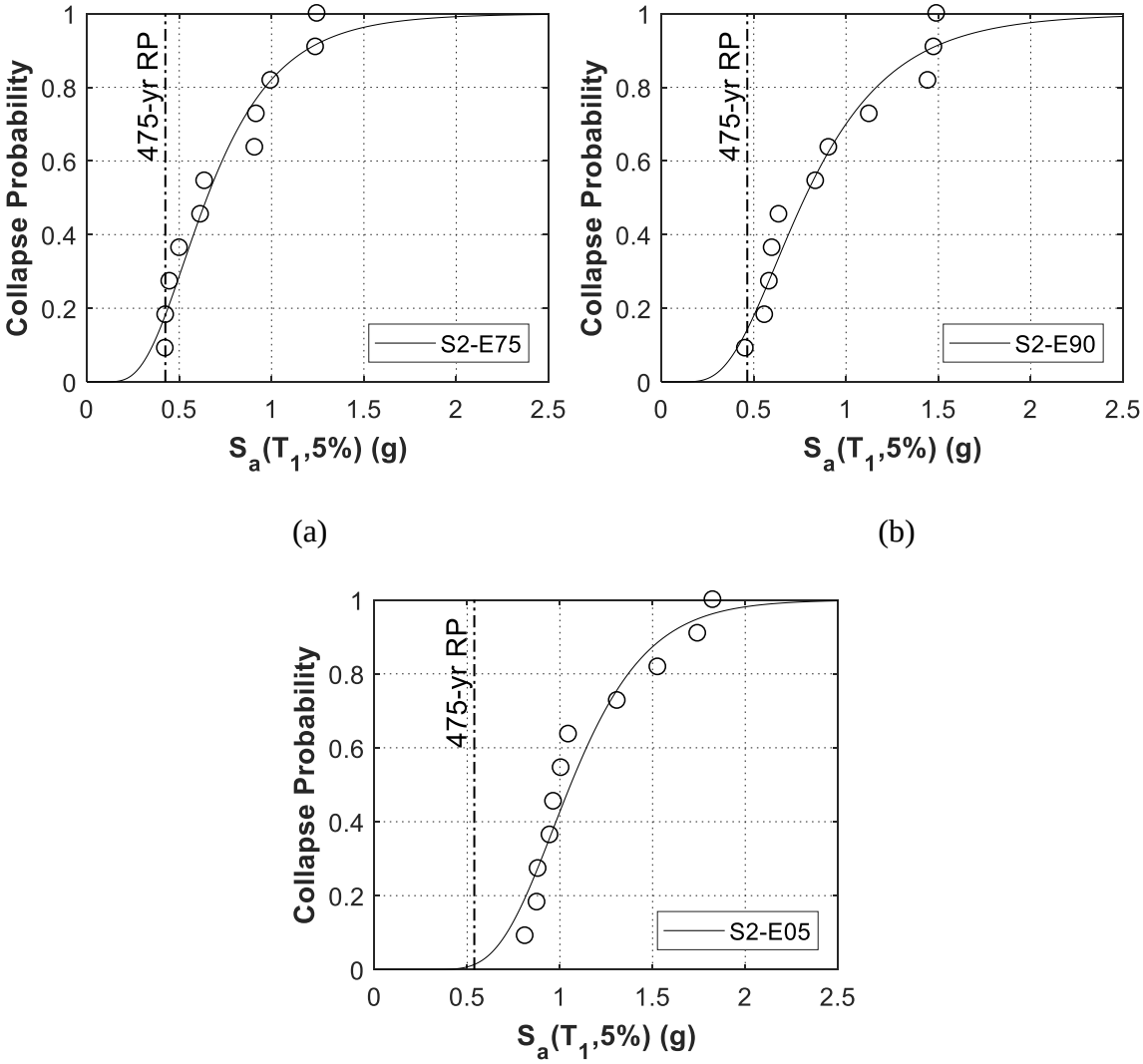

Figure 5-14. Collapse fragility curves of 2-story frames with spectral acceleration $S_a(T_1,5\%)$. (a) S2-E75 frame; (b) S2-E90 frame; and (c) S2-E05 frame

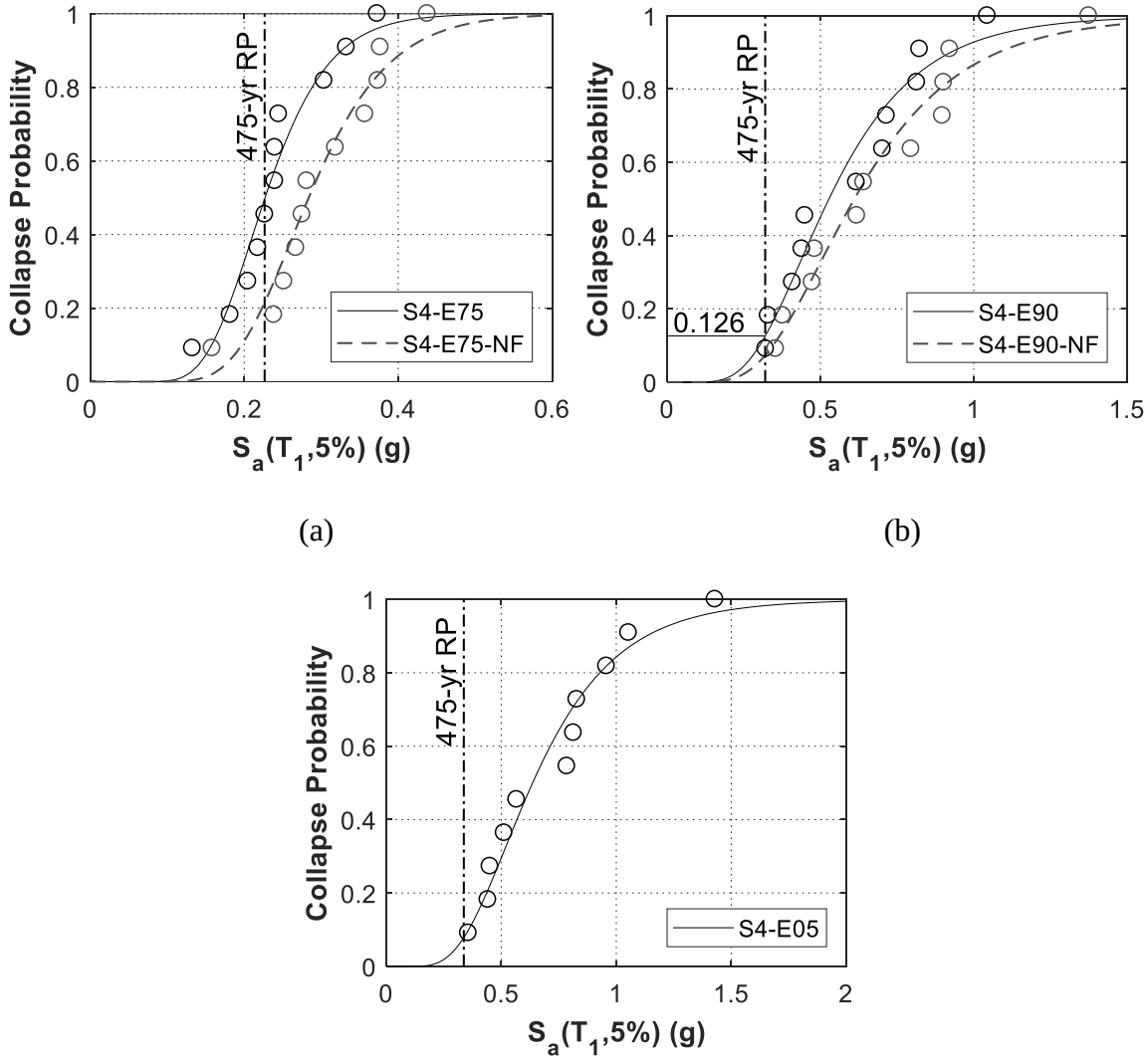

Figure 5-15. Collapse fragility curves of 4-story frames with spectral acceleration $S_a(T_1,5\%)$. (a) S4-E75 frame; (b) S4-E90 frame; and (c) S4-E05 frame

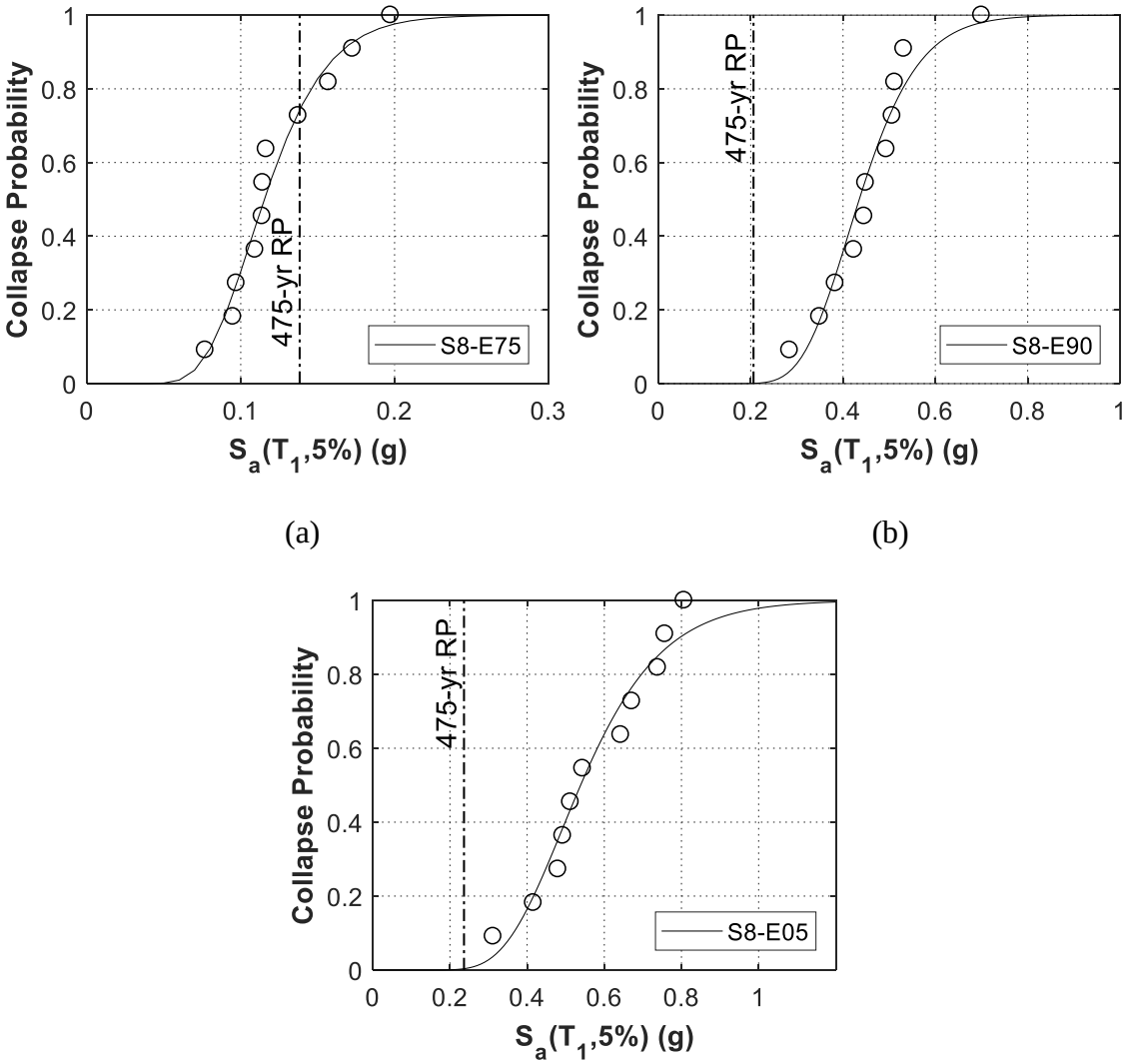

Figure 5-16. Collapse fragility curves of 8-story frames with spectral acceleration $S_a(T_1,5\%)$. (a) S8-E75 frame; (b) S8-E90 frame; and (c) S8-E05 frame

The collapse risk of E05 frames appears to be consistently low and independent of building height, where $P_{c,50yrs}$ ranges from 1.8-3.8%. The E90 frames, on the other hand, exhibit some dependence on building height, where $P_{c,50yrs}$ is lowest for the tallest building and highest for the shortest (1.9% for S8-E90 versus 5.7% for S2-E90). This dependence mainly results from the lower seismic hazard associated with the longer period at the assumed building site and the compromise of lateral

resistance of the S2-E90 frame due to connection fracture. Unlike the E90 frames, the E75 frames show an opposite and clear trend. The $P_{c,50yrs}$ of the S8-E75, S4-E75 and S2-E75 frames is 16.8%, 12.3%, 6.78%, respectively. These numbers are quite high, but comparable to $P_{c,50yrs}$ = 7.2% computed by Hutt et al. (2015) for a 40-story building designed per 1973 UBC. The high collapse risk is directly attributed to the large flexibility of the E75 frames, which increases P-Delta effects as the frames get taller.

Another set of models is developed to investigate the effect of rehabilitation on four-story frames with pre-Northridge connections (S4-E75 and S4-E90). These frames are not allowed to exhibit brittle weld fracture, although they still account for all other important aspects of the behavior, including local and global instability. The modified frames are appended with the letters NF (no fracture), e.g. S4-E75-NF. The results are shown in Table 5-2 along with the results for other frames, and the collapse fragility curves of the NF frames are shown in Figure 5-15(a)(b).

The simulation results show that the effect of brittle fracture in pre-Northridge connections is moderate and not as significant as expected in terms of collapse capacity. Not accounting for weld fracture caused the median collapse intensity, $\hat{S}_{a,C}$, to increase by about 20%, and $P_{c,50yrs}$ to decrease by about one-third for S4-75 and S4-90. One primary reason for the lower than expected effect is that even after weld fracture occurs, the connections are still able to retain some moment capacity, as shown in Figure 5-8 to Figure 5-10, attributed to the presence of the shear tabs and the contact between the column and beam flanges, as shown in Figure 5-11(b) and Figure 5-12(b). The reduction of frame lateral stiffness caused by connection fracture also diminishes the effect by reducing the seismic demands on the frame. Although S4-E90-NF has a lower $P_{c,50yrs}$ than S4-E05, it uses much more steel, reflecting the inherent inefficiency of the E90 seismic provisions and construction practices. A key observation from Table 5-2 is that none of the frames exhibit $P_{c,50yrs}$

< 1%, which is the current targeted uniform collapse risk specified by ASCE (2016) for buildings in the U.S. An immediate attention is required to address the non-uniform and high $P_{c,50yrs}$ associated with steel moment frames built in different eras in communities.

5.7.2 Repair Cost, Repair Time, and Casualties

Two thousand realizations are performed for each frame to determine key resilience measures under an earthquake with a return period of 475 years. The spectral acceleration corresponding to this intensity level, $S_{a,}(T_1, 5\%)_{475}$, for each frame is plotted as a dash-dot line in Figure 5-14 to Figure 5-16. Corresponding to each $S_{a,}(T_1, 5\%)_{475}$ is $P_{c, Sa475}$, the collapse probability of the frame under consideration. For example, $P_{c, Sa475}$ of S4-E90 is 12.6% as shown in Figure 5-15**(**b). $P_{c, Sa475}$ is used to determine if a frame has collapsed or not in a specific realization.

For realizations in which collapse does not occur, seven ground motion records from Table 3-1 are used to compute the peak story drift ratio (PSDR) and peak floor acceleration (PFA) demand parameters. These parameters are then used to estimate economic and social losses resulting from component damage. The structural and non-structural components considered in the assessment are listed in Table 5-3 with their fragility classification ID, name and category, demand parameter (PSDR or PFA that causes damage to the component), and number of possible damage states associated with the level of demand parameter. In the classification ID, the first letter and two numbers, the next two numbers, and the numbers after the decimal identify the category, a basic component, and variations in the basic component, respectively. For example, component B1035.011 and B1035.051 are post-Northridge RBS connection with welded web and pre-Northridge WFBW beam-column joints, respectively. Both joints are steel connections with W27 beams or smaller. Non-structural components are assumed seismically rated only in the E05 frames

because the detailed seismic design requirements of those components were not specified until the 2000 International Building Code (IBC) (ICC 2000).

For each frame, the computed losses include mean repair cost (direct economic loss), mean repair time (indirect economic loss), and mean casualties (social loss). The repair time is calculated by assuming that only one floor can be repaired at a time, i.e. serial repair time. The casualties in each realization are calculated by the population model combined with the casualty rate from falling hazard of components (if collapse does not occur) or building collapse (if collapse occurs). The mean casualties are normalized by the number of floors to facilitate comparisons between buildings with different heights. Irreparability due to residual drift is not considered. The loss estimation results, including $P_{c,\,Sa475}$, mean repair cost contributed by structural and non-structural components, and mean casualties contributed by falling hazard and collapse are summarized in Table 5-4 and shown in Figure 5-17, where it is clear that newer frames have better overall resilience indicators.

Table 5-3. Components considered in the resilience assessment of moment frames

Fragility Classification ID	Name	Category	Demand Parameter	Number of Damage States
B1031.001	Steel Columns	Super Structure	PSDR	4
B1031.011ab			PSDR	4
B1031.021ab			PSDR	3
B1035.001	Steel Connections	Super Structure	PSDR	3
B1035.002			PSDR	3
B1035.011			PSDR	3
B1035.012			PSDR	3
B1035.021			PSDR	3
B1035.031			PSDR	3
B1035.041			PSDR	5
B1035.042			PSDR	5
B1035.051			PSDR	5
B1035.052			PSDR	5
B2011.201a	Exterior Wall Construction	Exterior Enclosure	PSDR	2
B2011.201b			PFA	1
B2022.001	Curtain Walls	Exterior Enclosure	PSDR	2
C1011.011a	Fixed Partitions	Interior Construction	PSDR	3
C2011.001	Regular Stairs	Stairs	PSDR	3
C3011.001a	Wall Partitions Finishes	Interior Finishes	PSDR	1
C3032.001abcd	Suspended Ceilings	Interior Finishes	PFA	3
C3032.003abcd			PFA	3
C3034.001	Independent Pendant Lighting	Interior Finishes	PFA	1
C3034.002			PFA	1
D1014.011	Traction and Hydraulic Elevators	Conveying	PFA	4
D2021.012a	Potable Water Service	Plumbing	PFA	2
D2021.012b			PFA	2
D2021.013a			PFA	2
D2021.013b			PFA	1
D2021.022a			PFA	2
D2021.023a			PFA	2
D2021.023b			PFA	2

Table 5-3 (continued). Components considered in the resilience assessment of moment frames

Fragility Classification ID	Name	Category	Demand Parameter	Number of Damage States
D2022.012a	Hot Water Service	Plumbing	PFA	2
D2022.012b			PFA	2
D2022.013a			PFA	2
D2022.013b			PFA	1
D2022.022a			PFA	2
D2022.023a			PFA	2
D2022.023b			PFA	2
D2031.022a	Waste Piping	Plumbing	PFA	1
D2031.022b			PFA	2
D2031.023a			PFA	1
D2031.023b			PFA	1
D3031.011abcd	Chilled Water Systems	HVAC	PFA	1
D3031.013cfil			PFA	3
D3031.021abcd			PFA	1
D3031.023cfil			PFA	3
D3041.011c	Air Distribution Systems	HVAC	PFA	2
D3041.012c			PFA	2
D3052.011abcd	Package Units	HVAC	PFA	2
D3052.013cfil			PFA	4
D4011.022a	Sprinkler Water Supply	Fire Protection	PFA	2
D4011.023a			PFA	2
D4011.032a			PFA	2
D4011.053a			PFA	2
D5012.013a	Low Tension Service & Dist.	Electrical	PFA	1
D5012.013d			PFA	3
D5012.021abcd			PFA	1
D5012.023cfil			PFA	3

Table 5-4. Loss estimation of representative moment frames and retrofitted frames under an earthquake with a return period of 475 years

Frame ID	Seismically Rated Non-Structural Components	Total Replacement Cost (U.S. Dollars)	$P_{c,\,Sa475}$	Mean Repair Cost[a]			Mean Repair Time (days)	Mean Casualties (Number of People / floor)		
				Structural	Non-Structural	Total		Falling Hazard	Collapse	Total
S2-E75	N	7.06M	18.2%	8.2%	13.5%	39.9%	108	0.83	1.08	1.91
S2-E90	N	7.06M	14.2%	5.5%	12.8%	32.5%	86	0.63	0.88	1.52
S2-E05	Y	7.06M	1.4%	1.7%	8.7%	11.8%	22	0.06	0.08	0.14
S4-E75	N	14.1M	50.0%	3.2%	6.5%	59.7%	277	0.39	3.06	3.46
S4-E90	N	14.1M	12.6%	3.6%	10.8%	27.0%	114	0.69	0.76	1.45
S4-E05	Y	14.1M	7.9%	2.4%	7.0%	17.3%	74	0.08	0.48	0.56
S8-E75	N	28M	74.7%	0.9%	2.2%	77.8%	461	0.13	4.52	4.66
S8-E90	N	28M	0.7%	3.5%	10.5%	14.7%	104	0.92	0.04	0.97
S8-E05	Y	28M	0.3%	0.5%	5.2%	6.0%	44	0.02	0.02	0.04
S4-E75-NS	Y	14.1M	50.0%	3.2%	5.1%	58.3%	271	0.11	3.08	3.19
S4-E75-NF	N	14.1M	21.6%	3.8%	9.2%	34.6%	154	0.46	1.29	1.75
S4-E75-NF-NS	Y	14.1M	21.6%	3.7%	7.0%	32.3%	146	0.13	1.31	1.44
S4-E90-NS	Y	14.1M	12.6%	3.7%	7.9%	24.2%	106	0.10	0.78	0.88
S4-E90-NF	N	14.1M	7.3%	2.9%	11.1%	21.3%	85	0.67	0.44	1.11
S4-E90-NF-NS	Y	14.1M	7.3%	3.0%	8.3%	18.6%	76	0.10	0.44	0.54

[a]Expressed as a percentage of building total replacement cost.

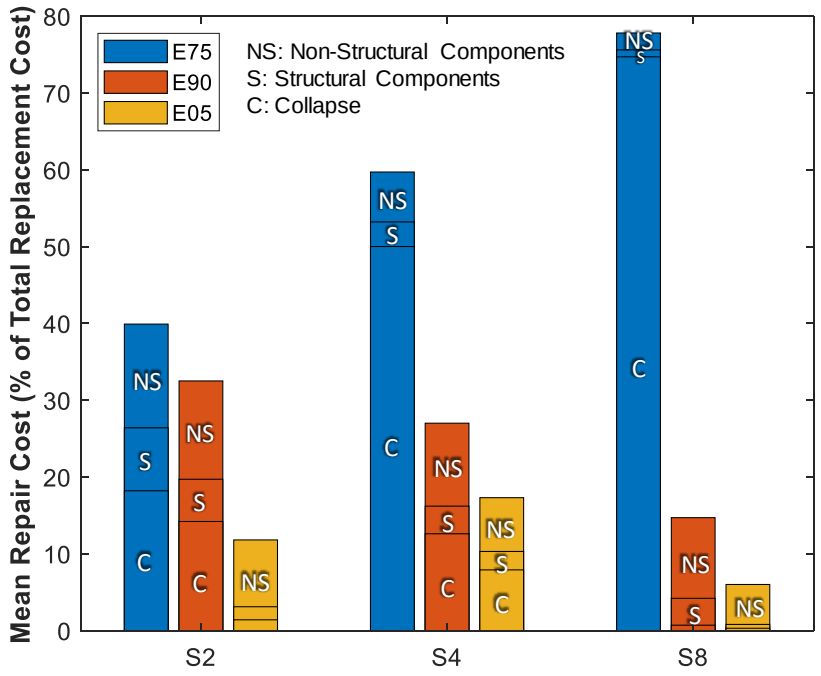

(a)

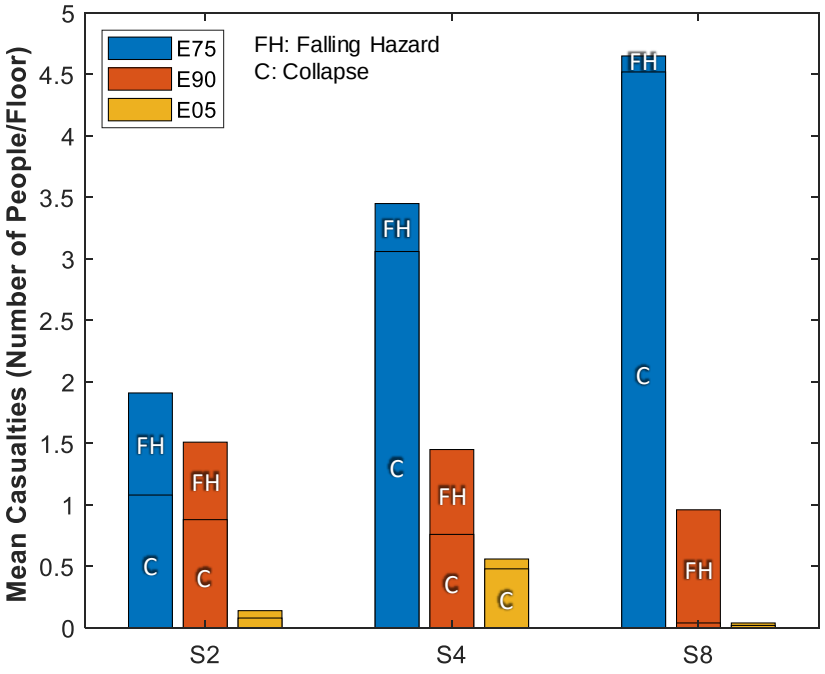

(b)

Figure 5-17. (a) Mean repair cost and (b) mean casualties of representative moment frames under an earthquake with a return period of 475 years

Table 5-4 shows that the E05 frames not only require much less repair cost and time to physically recover, but also have much less social impact on communities than their older counterparts. This result is not surprising since these frames, designed to the latest specification and practices, have the lowest collapse risk. Nevertheless, collapse risk paints only part of the overall resilience picture. Building size is another important consideration. For example, S8-E90 has the lowest $P_{c,\ Sa475}$ among all of the E90 frames, but the worst resilience indicators (specifically, economic and social losses) because of its size.

While the detailed assessment results are not shown, the major factors contributing to the estimated losses are collapse probability of the frames at the given intensity level, i.e. $P_{c,\ Sa475}$, fragility of the moment connections, and seismic rating of non-structural components. The influence of $P_{c,\ Sa475}$ on repair cost is evident in the proportional relationship between them. For example, the repair cost and $P_{c,\ Sa475}$ of S4-E75 frame is 50.0% and 59.7%, respectively, and the repair cost and $P_{c,\ Sa475}$ of S8-E75 frame is 74.7% and 77.8%, respectively. The effect of fragility of the moment connections and seismic rating of non-structural components can be observed by comparing the losses of S8-E90 to S8-E05. Although these two frames both have a low $P_{c,\ Sa475}$, S8-E90 has more than double the repair cost and time and much higher casualties than S8-E05. The former effects (repair cost and time considerations) are due to the fragile pre-Northridge connections and non-seismically rated non-structural components, while the latter effect (casualties) is attributed to the then-prevalent use of non-seismic pendant lighting, which are prone to fail during an earthquake. The above observation suggests that not only does the collapse fragility of older frames need to be improved, but also the seismic rating of its non-structural components in order to minimize the seismic losses incurred by communities.

5.8 Strategies to Improve Community Resilience

Seismic retrofit is expensive. As a result, most building owners will not embark on a rehabilitation program unless required to by authorities, e.g. through an ordinance. The results of the simulations conducted in this paper can provide insight into which retrofit strategies most influence the resilience of communities containing older steel moment frame buildings. A resilience assessment similar to that done above is performed on the S4-E75 and S4-90 frames by assuming that they have already been upgraded to have: (1) connection welds that are not prone to brittle fracture, and/or (2) seismically rated non-structural components in certain categories, specifically stairs, ceilings, lighting, piping, HVAC, and electrical equipment. In the following discussion, frames with upgraded non-structural components are designated with the letters NS, e.g. S4-E75-NS. As noted earlier, frames with upgraded connection welds are designated with NF. Frames with both NS and NF have been retrofitted along both fronts, e.g. S4-E75-NF-NS. Analyses are then conducted to shed light on how the NS, NF and combined NS/NF strategies affect the resilience indicators of the frames.

As shown in Table 5-4 and Figure 5-18, unlike its relatively moderate impact on collapse capacity, fracture of pre-Northridge connections can have a more severe effect on losses. For example, upgrading connections for S4-E75 (i.e. S4-E75-NF) can significantly decrease $P_{c,\,Sa475}$ from 50% to 21.6% and substantially lowers the total mean repair cost (drops from 59.7% to 34.6%). The mean casualties are also reduced by half (from 3.46 to 1.75) as the casualties due to collapse are largely avoided. The effect of upgraded connections on S4-E90 are much less significant because of the frame's lower $P_{c,\,Sa475}$ = 12.6% (versus 50% for S4-E75). For S4-E90, the total mean repair cost and casualties per floor decline from 27.0% and 1.45 to 21.3% and 1.11, respectively, when the NF repair is applied (i.e. S4-E90-NF).

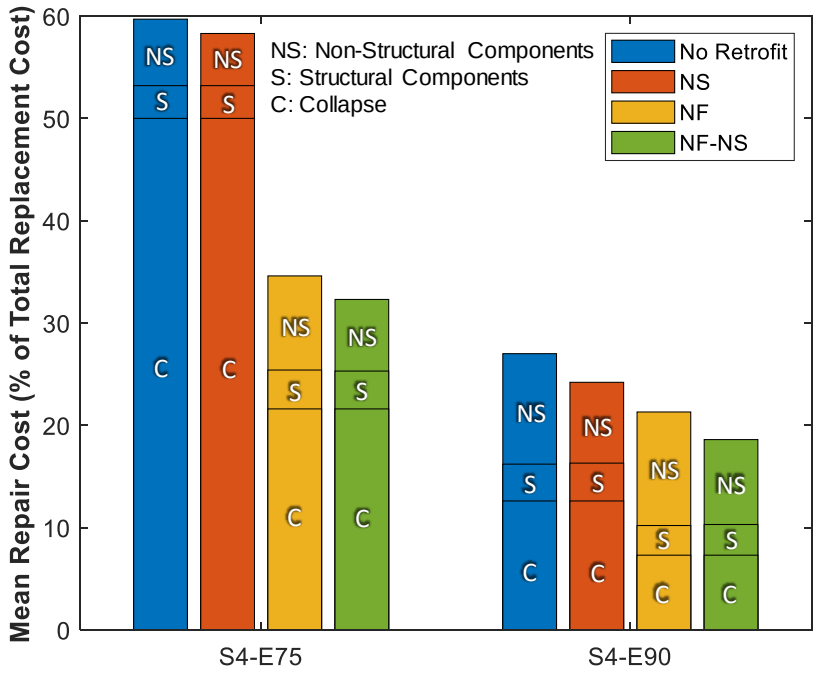

(a)

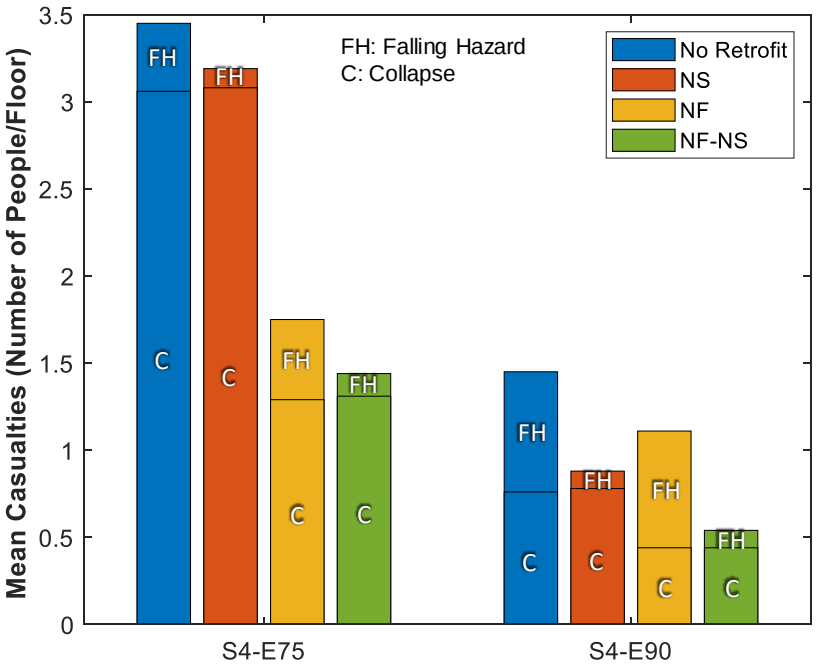

(b)

Figure 5-18. (a) Mean repair cost and (b) mean casualties of retrofitted moment frames under an earthquake with a return period of 475 years

The NS approach has only a small effect on the economic losses for S4-E90 (see Table 5-4) because the repair cost is mostly contributed by collapse and non-structural components that do not have the option for seismically rated upgrade. For example, the mean repair cost of S4-E90 drops from 27.0% to 24.2% by upgrading to seismically rated non-structural components (S4-E90-NS). Applying both approaches (S4-E90-NF-NS) is more effective and reduces the mean repair cost to 18.6%. The effect on casualties is more substantial, where applying both NF and NS reduces the mean number of casualties from 1.45 to 0.54. Similar trends can be seen for the S4-E75 frame, where the NS approach only reduces the mean repair cost by a small amount (from 59.7% to 58.3%) due to fact that half of realizations predict collapse, i.e. $P_{c,\ Sa475}$ = 50.0%. Applying NS and NF reduces the mean repair cost further to 32.3%. This number is still higher than the 30% maximum repair cost that owners would typically consider after major events before deciding to abandon a building (Kim 2015) and suggests that most owners would balk at a retrofit of this sort. However, a closer look at the effect of retrofit on mean casualties per floor suggests that rehabilitation could be quite effective if the resilience objective were just focused on saving lives (the mean casualties per floor drop from 3.46 to 1.44 for S4-E75 versus S4-E75-NF-NS, respectively).

A detailed analysis of the upgrade costs indicates that seismically upgrading certain components could be quite effective in improving resilience measures. For example, upgrading stairs and HVAC systems contribute to 89% of the reduction in mean repair cost between S4-E90 and S4-E90-NS (i.e. as shown in Table 5, 27.0%-24.2%=2.8% reduction). Non-seismic independent pendant lighting (C3034.001) is a key source of casualties due to the falling hazard and upgrading those in the S4-E90 frame can eliminate 40% of the mean casualties per floor.

The above discussion demonstrates the complexity of proposing and enforcing meaningful seismic upgrade policies and ordinances. It indicates that judiciously selected requirements can have a

substantial effect on resilience but with low to modest implementation cost. The study highlights that simulations of the sort done here can serve as a basis for cost-optimizing community-wide decisions regarding improvements in resilience through mandated policies.

5.9 Conclusion

This chapter presents a computational study that systemically investigates the effect of seismic design evolution on seismic risk of steel moment frames and their influence on seismic resilience of communities. A set of steel perimeter moment frames with three different heights are assumed in Santa Monica, California, and designed using seismic design codes from three eras spanning the past half century. The three eras, i.e. mid-1970s, early 1990s, and mid-2000s, represent the major differences in the evolution of seismic design and practice, including material properties, connection types, seismic design force, and panel zone design philosophy. High-fidelity finite element models capable of capturing fracture and instabilities in the steel structures are employed to reflect the differences. Within the limitations and assumptions of the study, the following conclusion can be drawn from the collapse analysis and resilience assessment of the set of steel moment frames:

- The collapse capacity of the moment frames increases as seismic design provisions evolved. Nevertheless, even the frames built according to the latest seismic provisions exhibit a collapse probability in 50 years larger than 1%, which is the expected collapse risk targeted by current seismic design maps. The non-uniform and high collapse risk posed to communities by steel moment frames built in different eras requires immediate attention.
- While the mid-2000s frames have consistently low collapse risk regardless of the building height, the collapse risk of mid-1970s and early 1990s frames are negatively and positively

affected by the height due to large flexibility and lower seismic hazard associated with longer period, respectively. These trends suggest that taller, older steel moment frames present higher seismic risk to communities. The fact that the early 1990s frames use 20% more steel than the mid-2000s frames but have a higher collapse risk suggests the inefficiency of the early 1990s design codes.

- Under an earthquake with a return period of 475 years, newer frames show better resilience and lead to less economic (repair cost and time) and social (casualties) losses experienced by communities. The tallest buildings have the largest estimated loss, even though they have the lowest collapse risk because of their great bulk.

- The key factors contributing most to the performance measures of steel moment frames are collapse probability at a given intensity level, fragility of moment connections, and seismic rating of non-structural components. The assessment results suggest that all three factors need to be improved to minimize the seismic losses incurred by communities.

- The effect of brittle fracture in the welds of pre-Northridge connections (E75 and E90 frames) on frame collapse capacity is moderate, but not as significant as expected. Even after fracture, the connections can still retain some moment capacity because of the presence of the shear tab and the contact between column flanges and beam flanges. Unlike with collapse capacity, weld fracture has a larger influence on losses. Rehabilitation of connection welds can reduce the losses by nearly half when the frame is vulnerable to collapse under a given earthquake.

- Applying both retrofit of pre-Northridge connections to prevent brittle weld fracture and upgrade of non-structural components is more effective and able to largely lower both

economic social losses as this strategy addresses three major factors, collapse probability, fragility of moment connections, and seismic rating of non-structural components. Among the upgraded non-structural components, stairs and HVAC system are more critical to reducing repair cost, while non-upgraded independent pendant lighting is a key source of casualties due to falling hazard.

The simulation results demonstrate the complexity of proposing and enforcing meaningful seismic upgrade policies and ordinances. It indicates that judiciously selected requirements could have a substantial effect on resilience but with low to modest implementation cost. The study also highlights that simulations of the sort done here can serve as a basis for cost-optimizing community-wide decisions regarding improvements in resilience through mandated policies.

CHAPTER 6

SUMMARY AND CONCLUSIONS

6.1 Summary

While deep steel columns have been widely used in the U.S. seismic zones after the 1994 Northridge earthquake, how their inelastic behavior affects collapse capacity of special steel moment frames is still not fully understood. Moreover, the effect of evolutionary changes in seismic design and engineering practice, e.g. the use of deep columns since late nineties, on seismic risk associated with steel moment frames has not yet been thoroughly examined and quantified. To address these problems, this dissertation investigated and provided new insights into the collapse capacity and resilience of steel moment frames, specifically those with deep columns under extreme seismic loading. A comprehensive experimental and computational research program was developed and conducted to identify key variables affecting cyclic flange local buckling, collapse response of steel deep columns under reversed cyclic loading, seismic behavior of moment frames with deep columns and seismic resilience of steel moment frames of various vintages. The findings were used to propose seismic design guidelines to reduce the collapse risk of steel moment frames with deep columns, in particular, and improve the seismic resilience of communities with steel buildings, more generally.

The effect of cyclic flange local buckling on the capacity of structural members in special moment frames was experimentally and computationally investigated. Nineteen half-scale T-section specimens were axially loaded to represent the flange/web subassembly in the plastic hinge region

of a wide flange section under combined axial and flexural loading. The specimens were selected to cover a wide range of slenderness ratios and subjected to three different loading schemes. The loading schemes included monotonic compression, meant to obtain the flange capacity without cyclic degradation, and two cyclic axial loading histories, one that reflected the axial demands on beam flanges and another for column flanges under cyclic drift loading. To further study the cyclic behavior of column flanges and justify the observations from the test results, a parametric computational study of the T-sections with different flange and web slenderness ratios was performed. The results of the simulations were used to evaluate the effect of element slenderness ratios on column compression capacity under cyclic loading.

The seismic collapse resistance of steel deep columns was then investigated using detailed finite element models. To realistically model the deep columns in special moment frames, collapse analyses of a four-story frame were performed to develop loading protocols representing drift demands on first-story columns in earthquake-induced collapse scenarios. The developed loading and boundary conditions were shown to be realistic in terms of deformed shape and hysteresis responses when compared to those obtained from full frame analyses. Parametric simulations of deep wide flange columns showed that the most influential variables affecting the seismic collapse resistance of deep columns are web slenderness ratio (h/t_w), global slenderness ratio (L/r_y), and sinitial axial load ratio (P_g/P_y). A regression analysis was conducted to quantify the effect of these variables and used to propose highly ductile limits for the web slenderness ratio as a function of other key variables.

Computational simulation was also used to investigate the influence of deep columns on the collapse performance of moment frames. Four- and eight-story prototype frames and their variants were used to study the following parameters on the collapse potential: (1) column lateral bracings,

(2) level of column gravity load, and (3) column section properties. The finite element models employed were capable of modeling local and global instabilities and could explicitly represent both sidesway and vertical collapse modes of behavior. After defining suitable collapse criteria, incremental dynamic analyses were conducted to compute collapse fragility curves of the studied frames. Simulation results confirmed the detrimental influence of high global slenderness ratios (L/r_y) on overall system behavior and indicated that the axial load level (P_g/P_y) on exterior columns should be limited to ensure good seismic response. The simulation results also suggested that column shortening, in itself, is a benign effect that does not compromise serviceability or contribute to the collapse of a well-designed frame.

The final phase of this work examined how the evolution of building design codes influenced the seismic resilience of communities with steel moment frames of different ages. The evolution of building codes and design practices for steel buildings in the U.S. over the past half century were thoroughly reviewed to identify major changes. Then, a set of two-, four-, and eight-story steel moment frames (with the same building plan) were designed according to provisions and practices conforming to three eras: mid seventies, early nineties and mid two thousands. Major design and practice variables included material properties, connection types, seismic design force, and panel zone design philosophy. High-fidelity finite element models capable of explicitly capturing instabilities and fracture were employed to determine the effect of the design differences on frame performance. The FEMA P-58 methodology was then used to assess the resilience of the designed frames. It was shown that, although the collapse capacity and resilience indeed increased as the codes evolved, the collapse probability of frames built according to the latest seismic provisions still exceed the expected standards. The assessment results were used to propose retrofit strategies for improving the seismic resilience of steel moment frames.

6.2 Conclusions

The following major conclusions can be drawn from the research completed toward this dissertation:

6.2.1. Cyclic Flange Local Buckling

- Most T-section specimens could reach a peak strength of P_y regardless of the value of $b/2t_f$, but $b/2t_f$ substantially influenced post-buckling behavior. Under monotonic (M) loading, the current value for λ_{hd} for a flange is a boundary between large buckling capacity and rapid degradation after reaching peak strength. The effect of the equivalent web slenderness $(h/t_w)_{eq}$, on the other hand, is secondary and becomes significant only when both $b/2t_f$ and $(h/t_w)_{eq}$ are large and negatively interact with each other.

- Specimens under the cyclic-beam (CB) loading protocol exhibited much more severe compressive strength degradation than the monotonic (M) protocol. Depending on a specimen's $b/2t_f$, the compressive strength dropped to as low as 0.53 P_y at deformation levels that corresponded to 4% beam rotation. For specimens under the cyclic-column (CC) loading protocol, although their backbone curves were much higher than those of specimens under CB protocol and quite close to the responses under M protocol, the degradation at 4% drift level is more significant than that under CB protocol and can compromise the axial and flexural capacities of the columns.

- The current non-slender limit (λ_r) is adequate for both beam flanges and column flanges under the monotonic and cyclic loading schemes considered in this work. The current highly ductile limit (λ_{hd}) is also reasonable for beam flanges under cyclic loading. However,

conclusions in regard to λ_{hd} for column flanges under cyclic loading are not definitive because the performance expectations of columns in the AISC seismic provisions are not as explicit as they are for beams.

6.2.2. Seismic Collapse Behavior of Deep Steel Columns

- The first-story drift histories in the frame analyses show a cyclic ratcheting (CR) behavior, which causes local buckling mostly on one side of the column end. This limits the amount of degradation in the boundary restraints and suggests that the symmetric cyclic loading protocol (SC), which has been commonly used to test columns to collapse, is unrealistically conservative and likely misleading. The SC protocol causes substantial local buckling on both sides of the column end, which significantly degrades column buckling strength in an unrealistic manner.

- The drift capacity of columns with a fixed-pinned (FP) top end is substantially worse than columns with other boundary conditions due to a longer out-of-plane effective buckling length. On the other hands, columns with a spring-fixed (SF) top end have the highest capacities because of less local buckling at top of the column and hence a milder degradation in the top restraint.

- By applying realistic loading and boundary conditions to individual column models, h/t_w, L/r_y, and P_g/P_y are all shown to have a significant effect on the collapse resistance of deep columns. Generally, the effect of h/t_w on post-drift strength is larger than L/r_y, and the effect of P_g/P_y increases the higher it becomes. The simulation results also clearly show that deep columns satisfying current λ_{hd} are not necessarily able to reach 4% drift without failure.

- From the linear regression of column axial capacity, highly ductile limits for both interior and exterior columns are proposed in a format that is suitable for adoption into AISC seismic specifications. The proposed limits approximately match the current limits for interior columns with $L/r_y < 80$ and $h/t_w = 50$ when $C_a = 0.3$ but penalize columns that have larger L/r_y or are under higher initial axial loads. For exterior columns, the proposed limits are less stringent than the ones for interior columns as they penalize the exterior columns with $L/r_y > 105$ and $h/t_w = 50$ when $C_a = 0.3$ because of less in-plane rotational restraint at the column top end.

6.2.3. Seismic Collapse Behavior of Steel Special Moment Frames with Deep Columns

- The collapse simulations of SMFs with deep columns confirm the importance of h/t_w and L/r_y and show that they are influential not only on member response but also on collapse capacity and collapse modes of SMFs. For example, replacing the original exterior columns (W24×103) under $P_g/P_y = 0.27$ in the studied four-story frame with a stockier section (i.e. lower h/t_w and L/r_y) (W24×131) increases the median collapse spectral acceleration by 34% and shifts the collapse mode from vertical to sidesway collapse.

- P_g/P_y is also shown to be influential on the robustness of SMFs and their probability of collapse. For the studied four-story frame, the median value of collapse maximum story drift ratio decreases rapidly when P_g/P_y surpasses about 0.2, which also appears to be a transition point between responses dominated by sidesway and vertical collapse. This high sensitivity to axial load level shows that the permissible level of gravity load should be specified in design provisions to prevent an undesired collapse mechanism.

- Additional lateral bracing at the level of the beam bottom flanges for beam-to-column connections moderately improves the collapse capacity of SMFs, e.g. the median collapse spectral acceleration of the studied four-story frame with P_g/P_y = 0.27 increased by 20%. It is prudent to recommend that beam-column connections in SMFs should be braced at the top and bottom of the beam flanges, regardless of the column-beam moment ratios at the connection.

- Both column- and frame-level studies presented in this dissertation show that the amount of column shortening is minimal for small drifts (i.e. 1%) and does not compromise building serviceability. For large drifts (i.e. 4%), because frames with similar column shortening have quite different collapse behaviors, it is suggested that the column shortening does not play a direct role in collapse response. In fact, column shortening is merely a consequence of local buckling, which can be controlled by limiting the element slenderness ratios and axial load demand.

6.2.4. Resilience of Steel Moment Frames in Communities

- The seismic collapse capacity and resilience of steel moment frames have improved as codes evolved during the past fifty years. However, even the frames built according to the latest seismic provisions exhibit a collapse probability in 50 years larger than the expected collapse risk of 1% targeted by current seismic design maps. The non-uniform and high collapse risk posed to communities by steel moment frames built in different eras has not yet been historically seen and requires immediate attention.

- The factors that contribute most to the resilience of steel moment frames are collapse probability at a given intensity level, fragility of moment connections, and seismic rating

of non-structural components. The assessment results suggest that all of these three factors need to be improved through a retrofit plan to minimize the seismic losses incurred by communities.

- The effect of brittle fracture in the welds of pre-Northridge connections on frame collapse capacity is moderate and not as significant as expected because the presence of the shear tab and the contact between column flanges and beam flanges help the connections retain some moment capacity. However, retrofitting the welds can be influential in improving seismic resilience of frames and decreasing economic and social losses when the frame is vulnerable to collapse under a given earthquake.

- Upgrading specific non-structural components can be effective in reducing seismic losses. For example, anchoring HVAC systems and providing an inter-story slip joint to stairs are more critical to reducing repair cost, while using seismically rated independent pendant lighting can avoid most casualties due to falling hazard.

6.3 Recommendations for Future Research

The work presented in this dissertation provides the groundwork for several different research directions to better understand the collapse resistance of steel structures and seismic resilience of communities:

(1) Using the same rationale for T-section specimens, channel sections can be used to study the cyclic local buckling of flanges in HSS sections and its effect on capacity of HSS beams or columns. In addition to symmetric cyclic drift loading, a more realistic loading protocol, e.g.

cyclic ratcheting (CR) protocol, could be applied to HSS members in the development of axial loading schemes on channel sections.

(2) The highly ductile limits (λ_{hd}) proposed in the column study of this work are based on the simulations of a limited number of W24 to W30 sections. Additional work using more and deeper sections is imperative to verify the proposed limits or adjust them if needed. On the other hand, while shallow sections have less concerns regarding instabilities, the applicability of current limits for these sections should be further examined using more realistic boundary and loading conditions.

(3) The frame study in this work makes use of only four- and eight-story three-bay SMFs. As the overturning moment effect on exterior columns is greatly dependent on height and number of bays of moment frames, future parametric studies that incorporate a set of SMFs with different building configurations is needed to determine the permissible level of axial load ratio due to gravity load (P_g/P_y) on exterior columns and to prevent undesired collapse mechanisms.

(4) For the sake of convenience, earthquake excitation is assumed to occur only along the frame direction in this work. The results obtained herein could be further generalized by considering the full three-dimensional building response under bi-directional earthquake excitation. This modeling can also consider the effect of slabs and shear connection failure to explore the low redundancy resulting from the use of perimeter moment frames.

(5) The study of seismic design evolution in this work only considered two retrofit options for steel moment frames and their effect on resilience. However, a community-wide retrofit plan relies on not only the effect of resilience, but implementation cost to optimize available resources. More retrofit options can be investigated for buildings with different occupancies and structural systems to help community planners design cost-optimized mandated policies.

APPENDIX A

FAILURE MODES AND HYSTERESIS RESPONSES OF T-SETION SPECIMENS

This appendix contains the failure modes and measured hysteresis responses of all tested T-section specimens presented in Chapter 2. The failure mode is the local buckling mode at the end of test or ductile fracture that ends the test. Recall that the applied axial load and axial displacement is measured by a load cell and an optical tracking system, respectively, and normalized by the yield strength of the cross-section and the original length of the members, respectively.

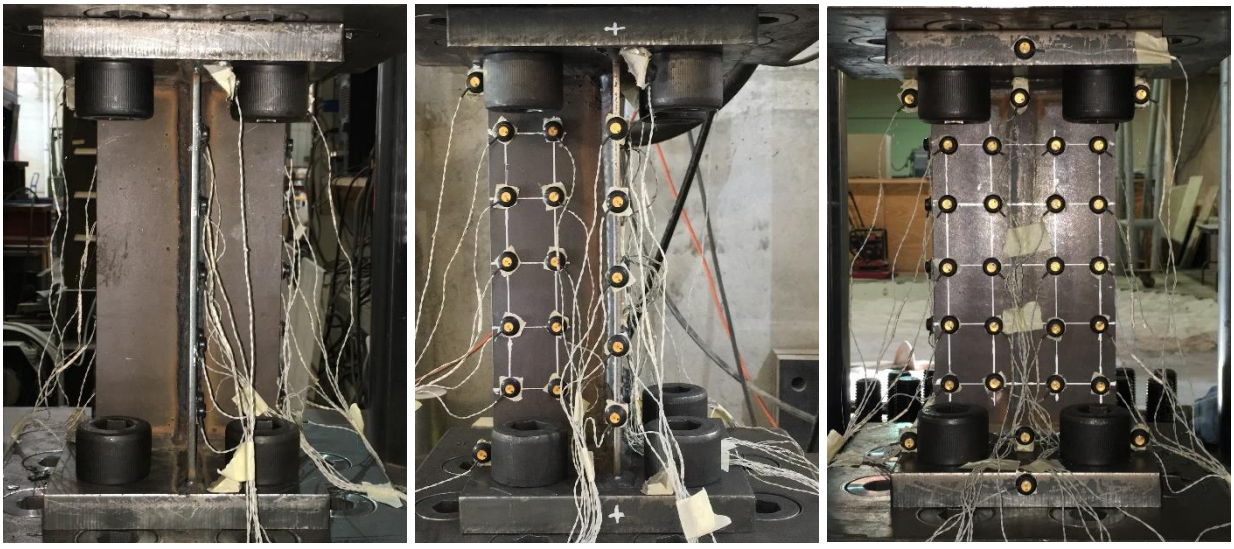

(a) (b) (c)

Figure A-1. Typical test setup: (a) side view (north) (b) front view (west); (c) side view (south)

(a)

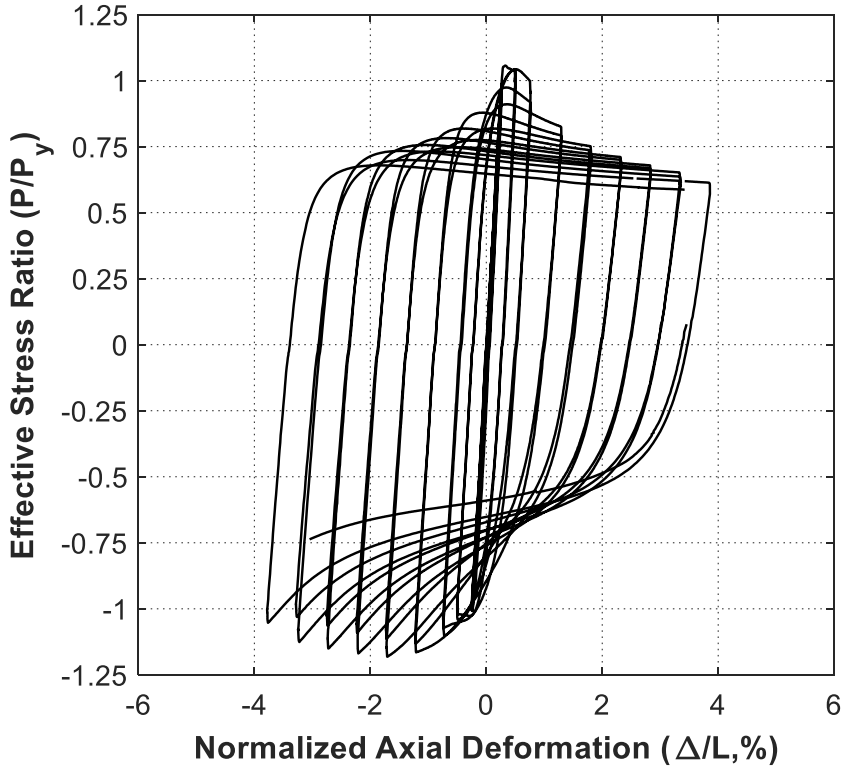

(b)

Figure A-2. Specimen W12×26-CB (a) ductile fracture (b) hysteresis responses

(a)

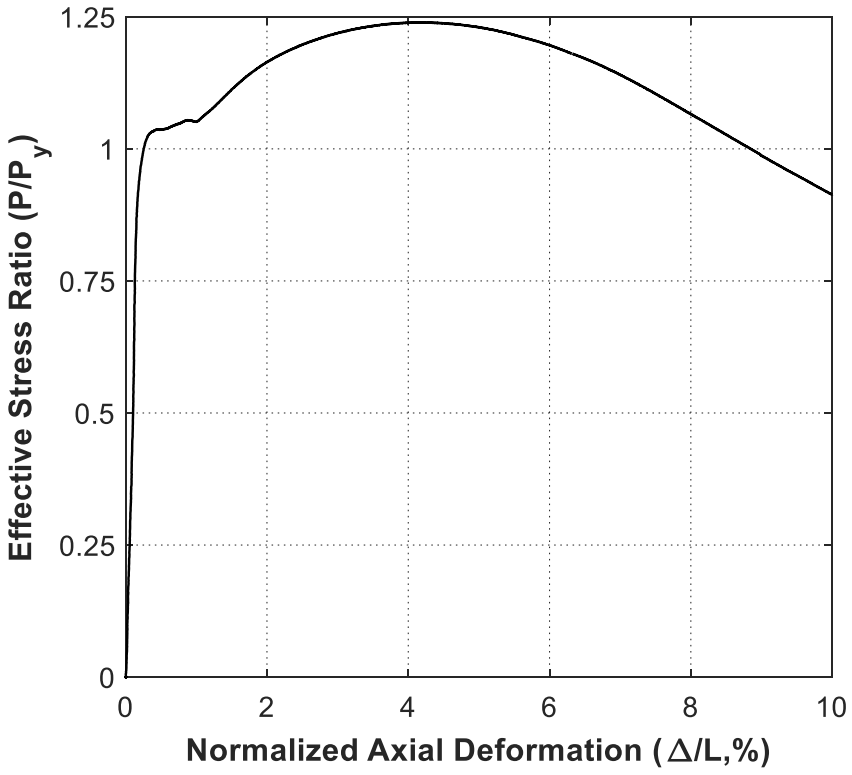

(b)

Figure A-3. Specimen F1W1-M (a) symmetric local buckling (b) hysteresis responses

(a)

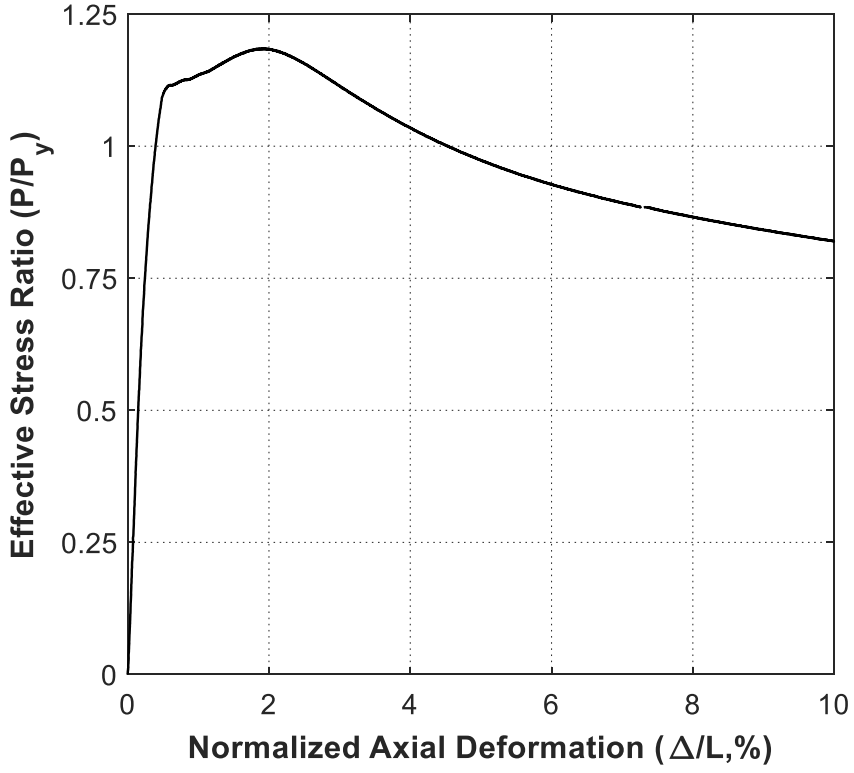

(b)

Figure A-4. Specimen F2W1-M (a) asymmetric local buckling (b) hysteresis responses

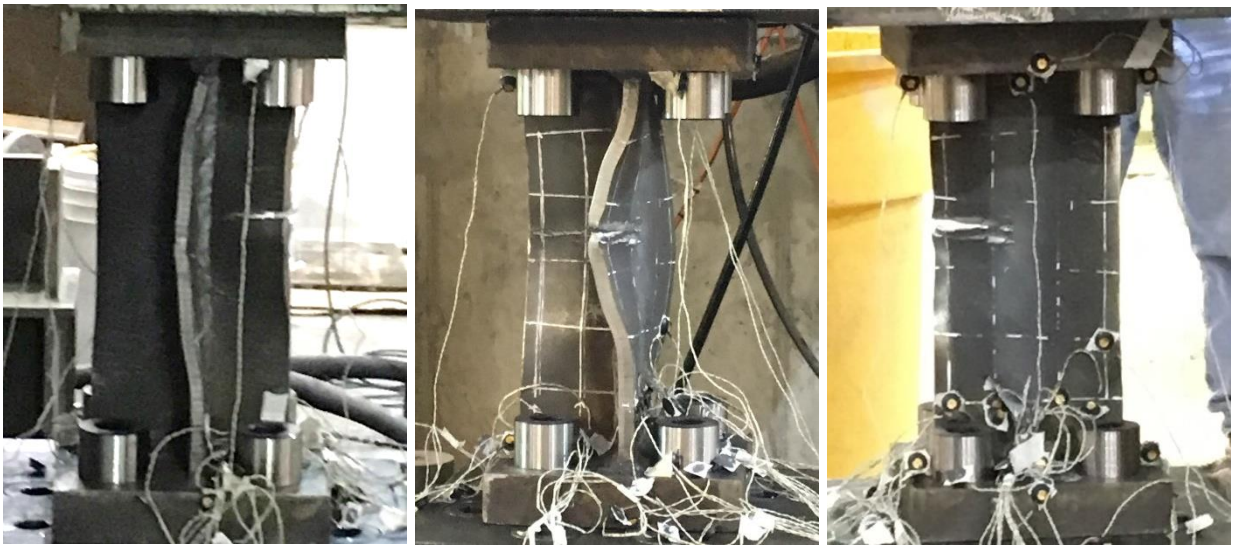

(a)

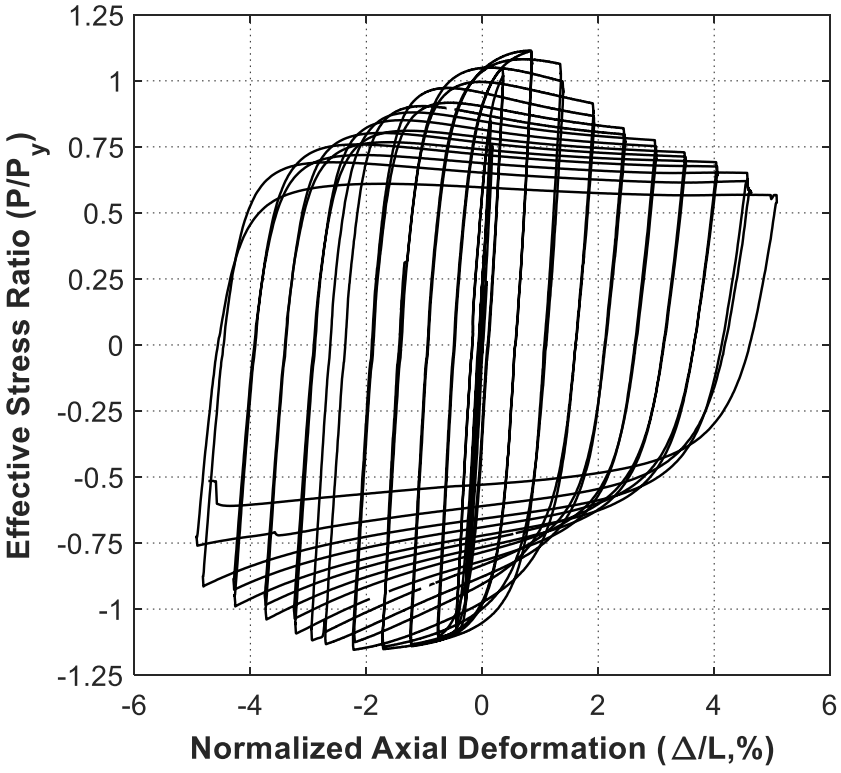

(b)

Figure A-5. Specimen F2W1-CB (a) ductile fracture (b) hysteresis responses

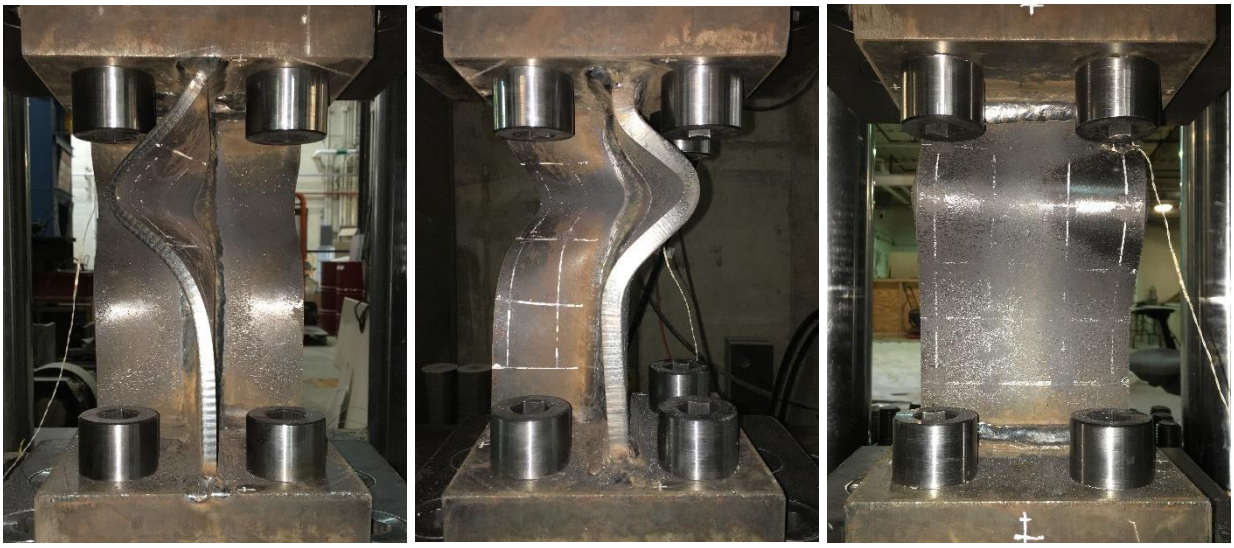

(a)

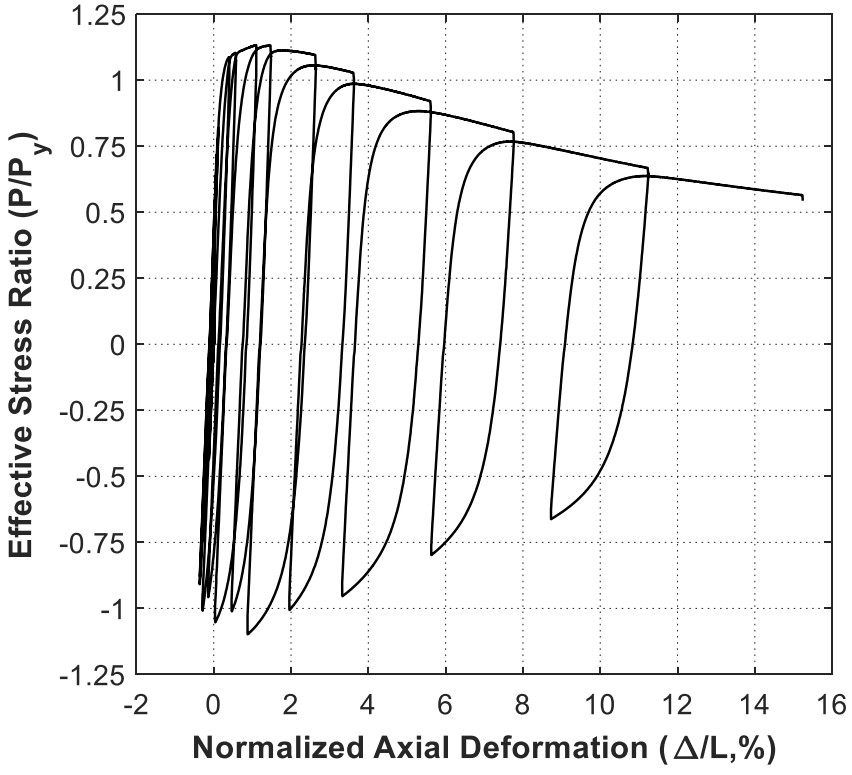

(b)

Figure A-6. Specimen F2W1-CC (a) symmetric local buckling (b) hysteresis responses

(a)

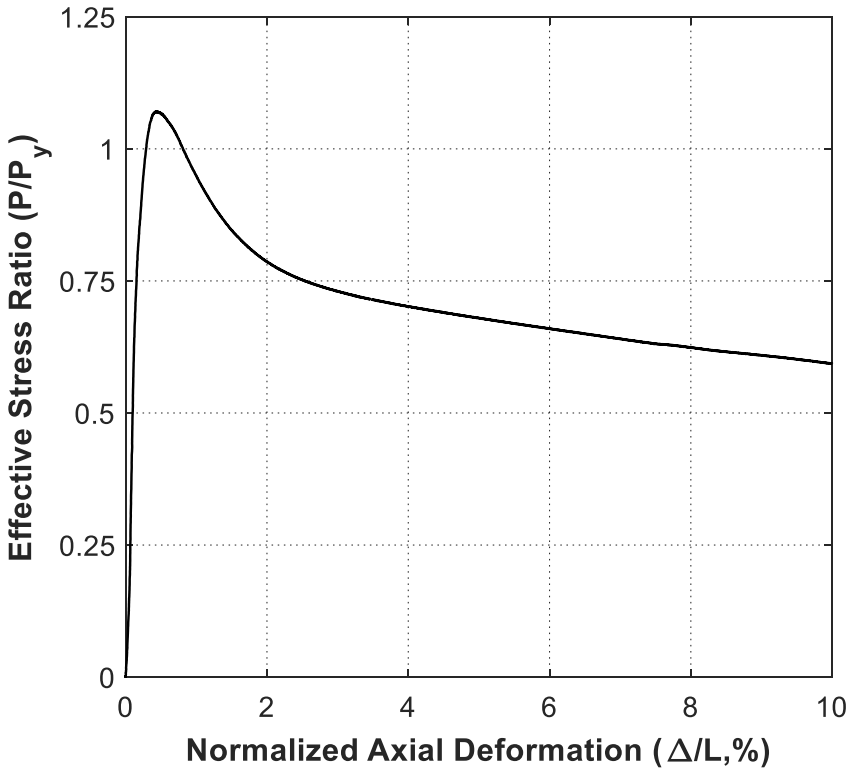

(b)

Figure A-7. Specimen F4W1-M (a) asymmetric local buckling (b) hysteresis responses

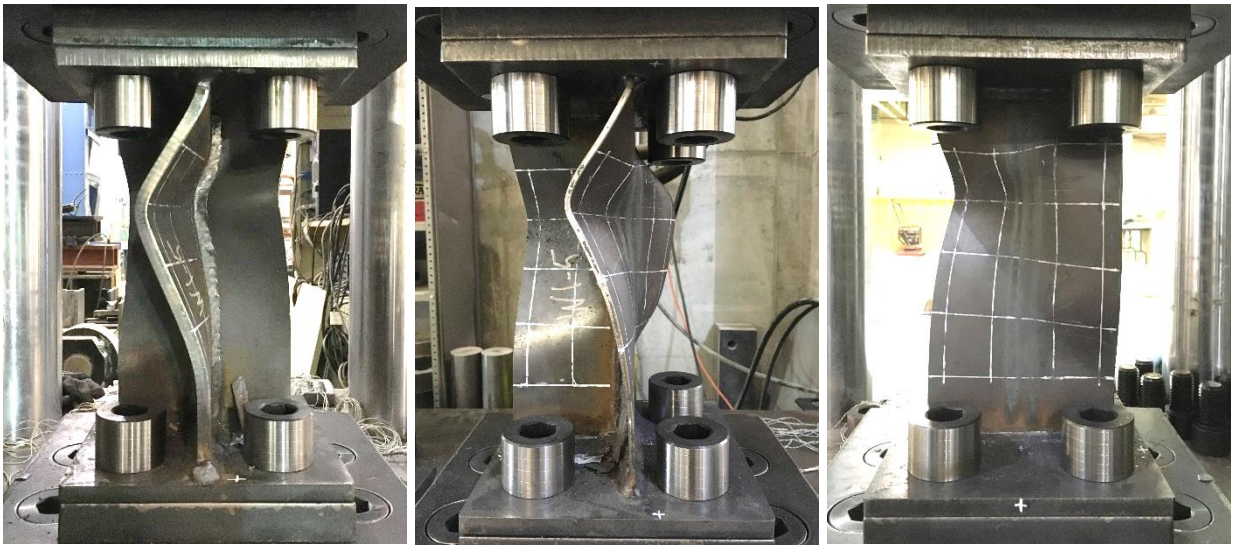

(a)

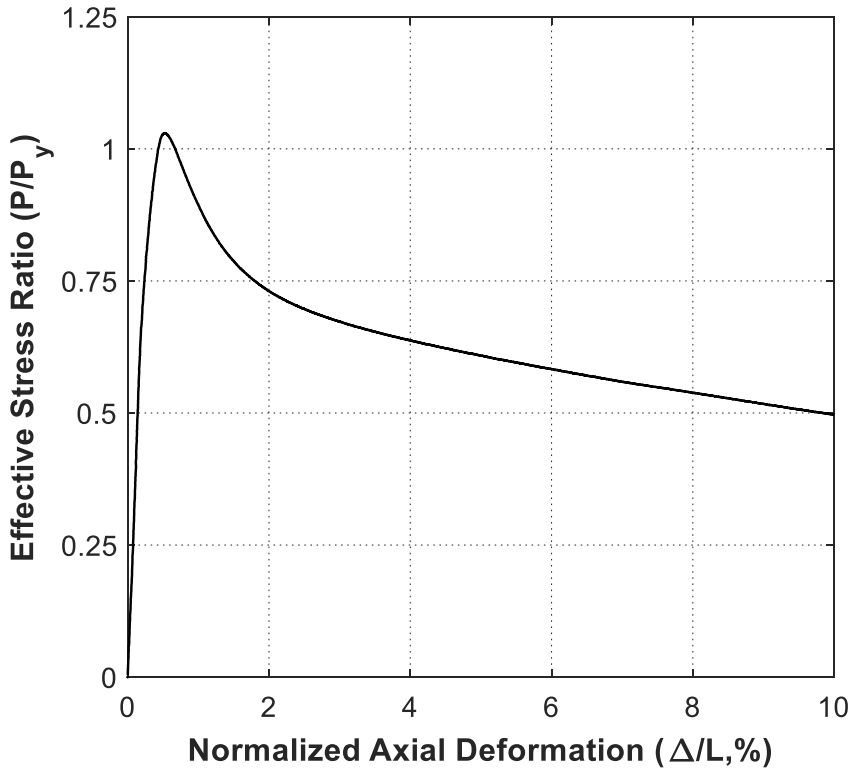

(b)

Figure A-8. Specimen F5W1-M (a) asymmetric local buckling (b) hysteresis responses

(a)

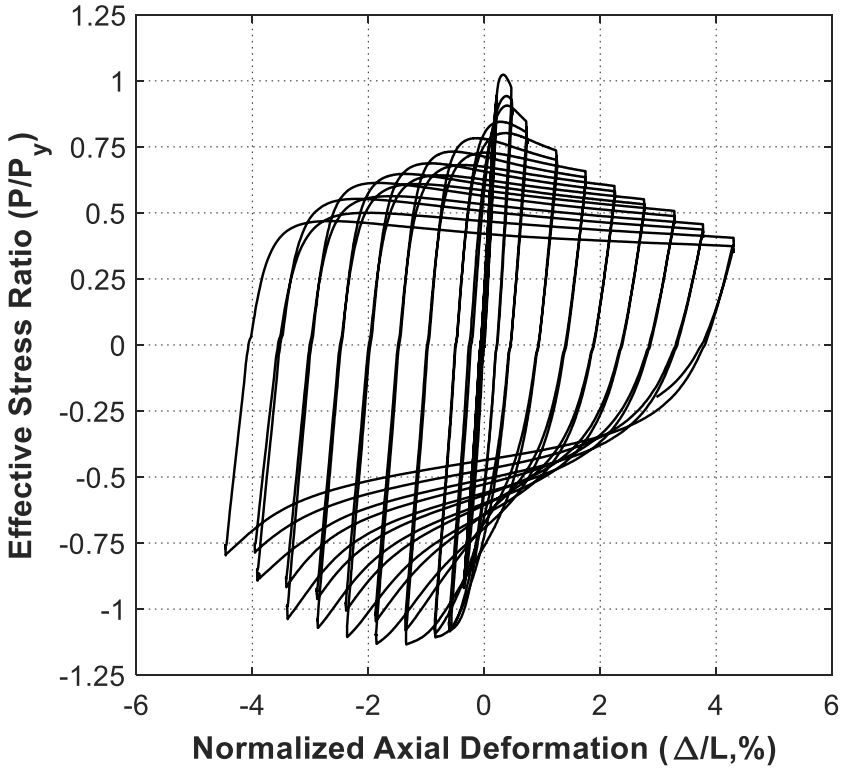

(b)

Figure A-9. Specimen F5W1-CB (a) ductile fracture (b) hysteresis responses

(a)

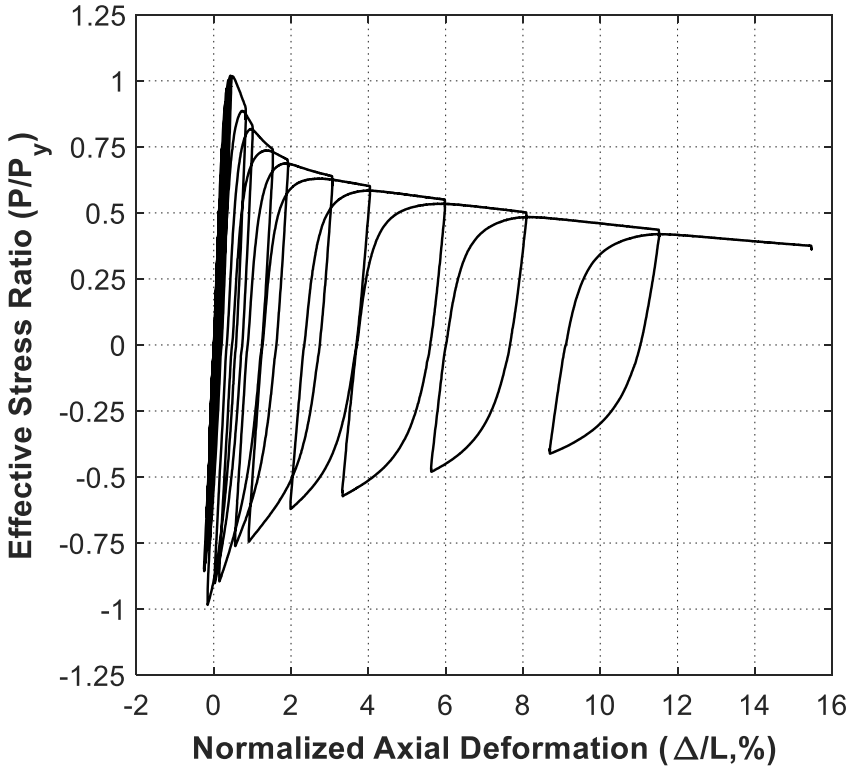

(b)

Figure A-10. Specimen F5W1-CC (a) asymmetric local buckling (b) hysteresis responses

(a)

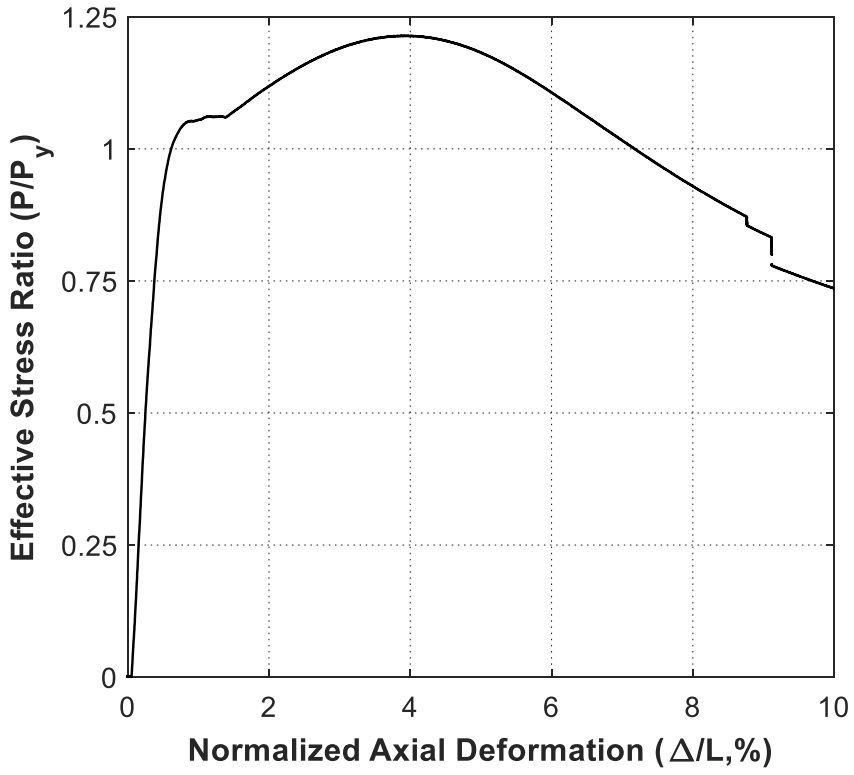

(b)

Figure A-11. Specimen F1W2-M (a) symmetric local buckling (b) hysteresis responses

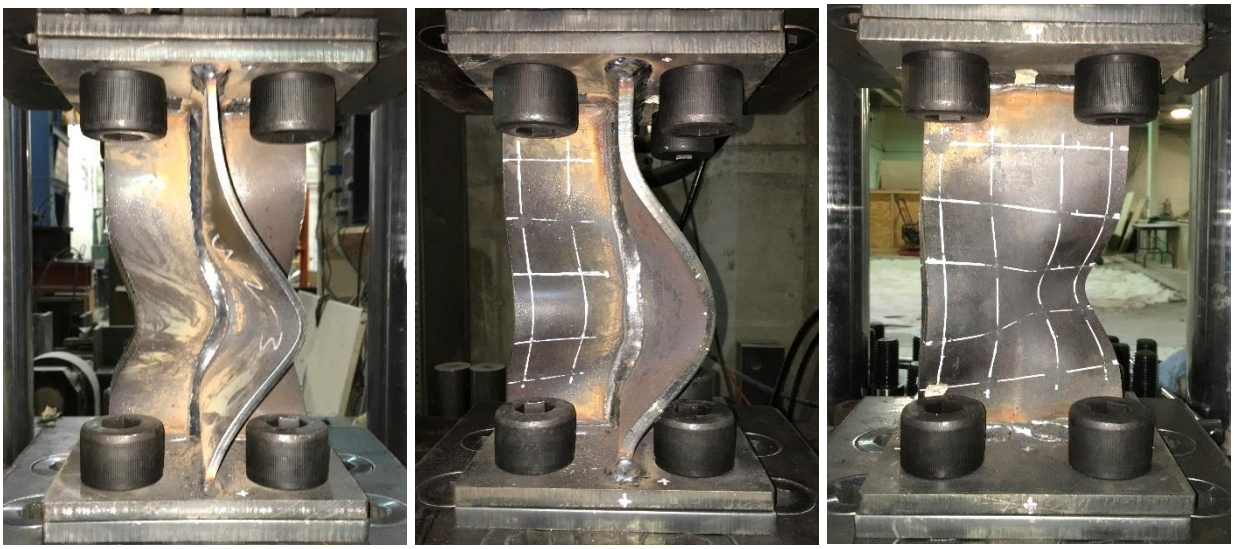

(a)

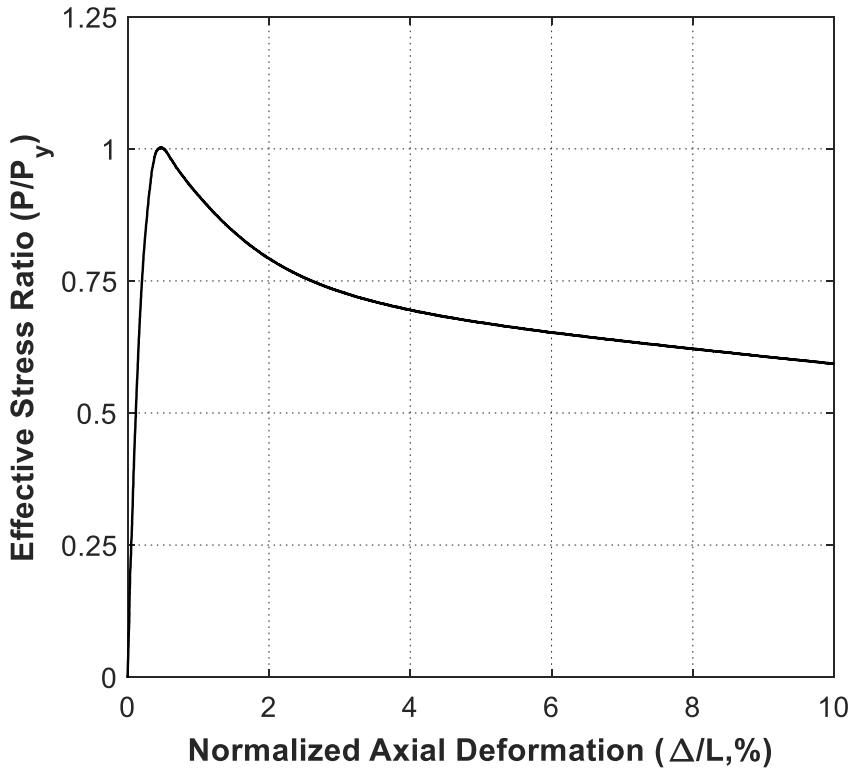

(b)

Figure A-12. Specimen F3W2-M (a) asymmetric local buckling (b) hysteresis responses

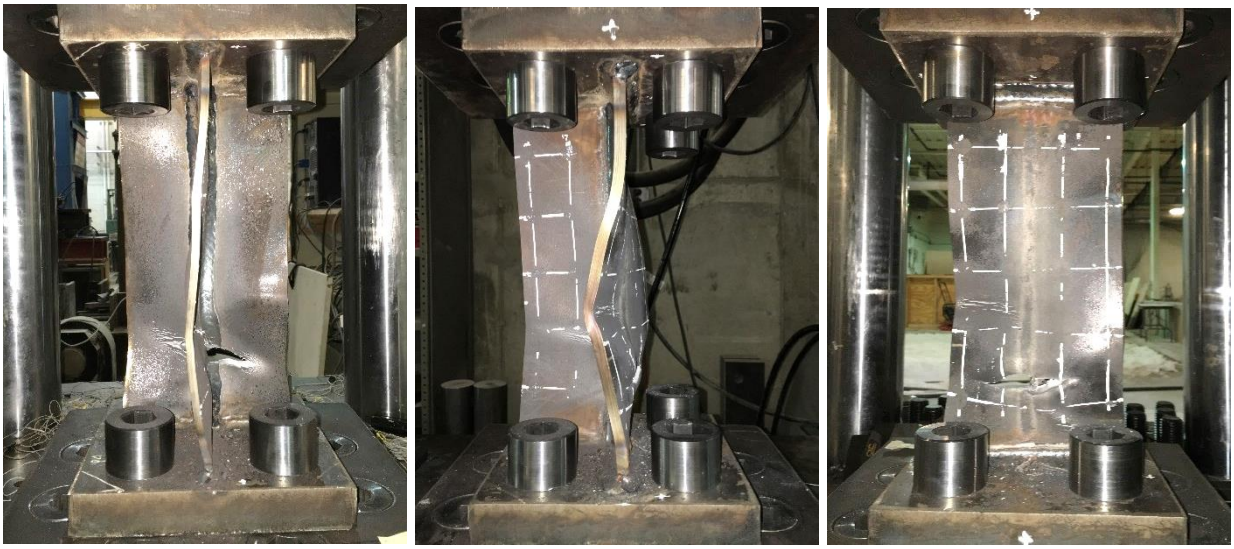

(a)

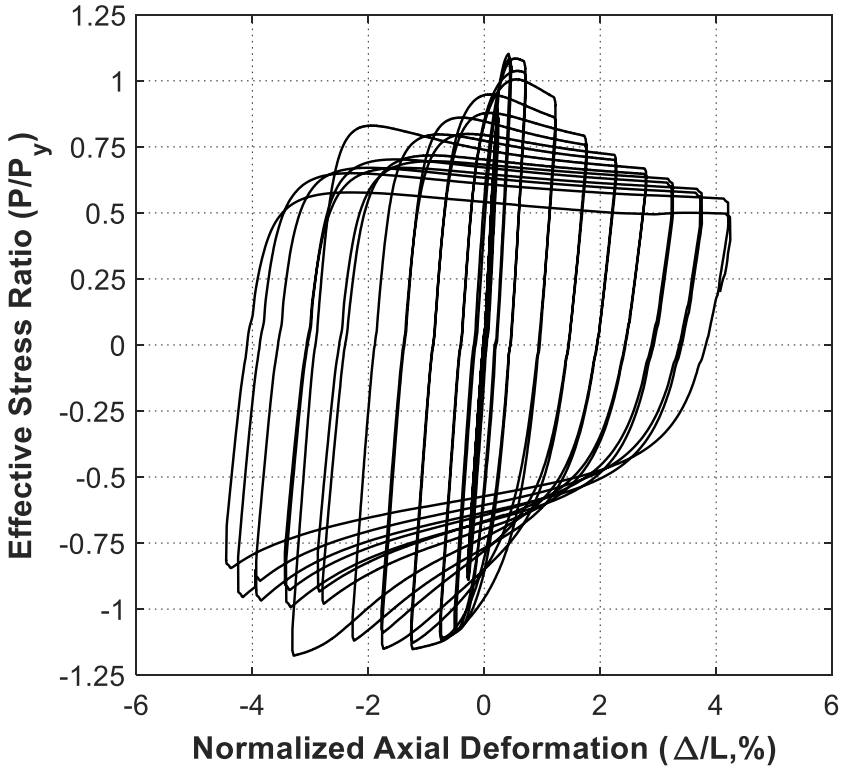

(b)

Figure A-13. Specimen F3W2-CB (a) ductile fracture (b) hysteresis responses

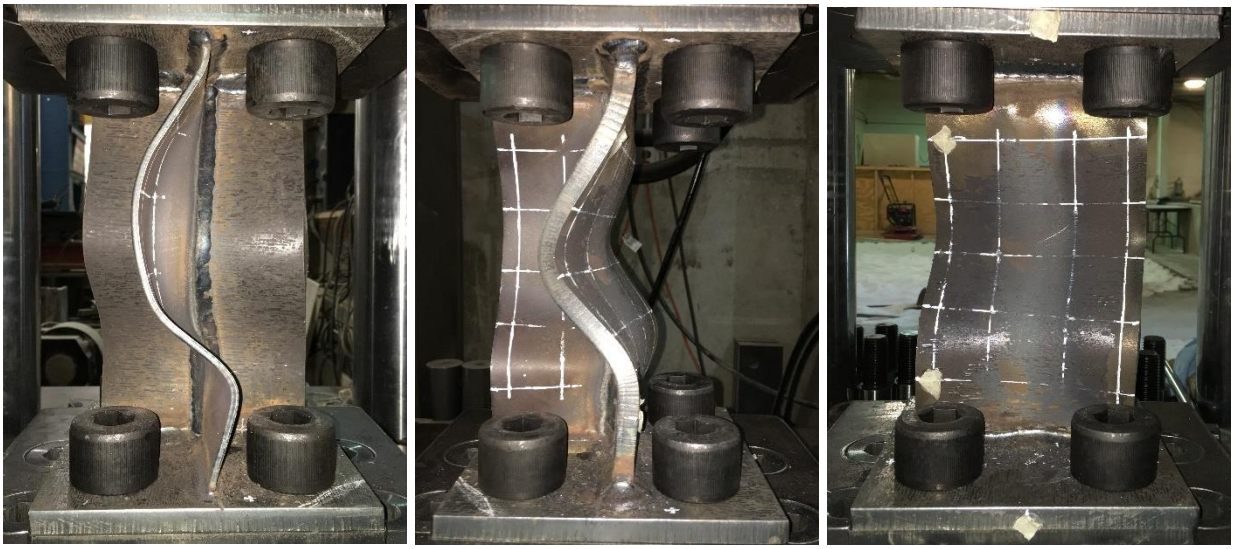

(a)

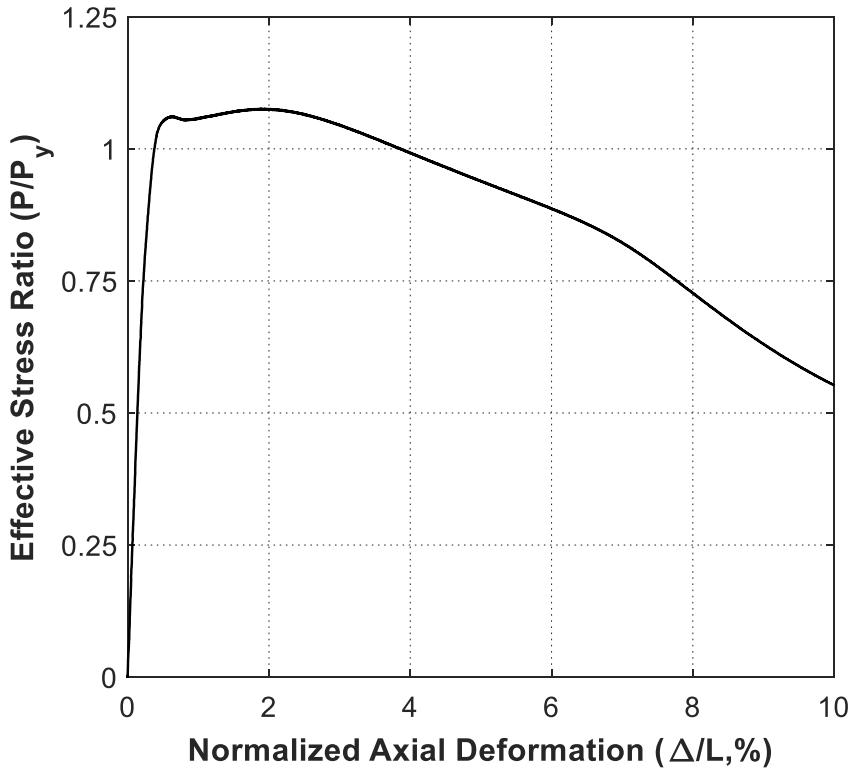

(b)

Figure A-14. Specimen F2W3-M (a) symmetric local buckling (b) hysteresis responses

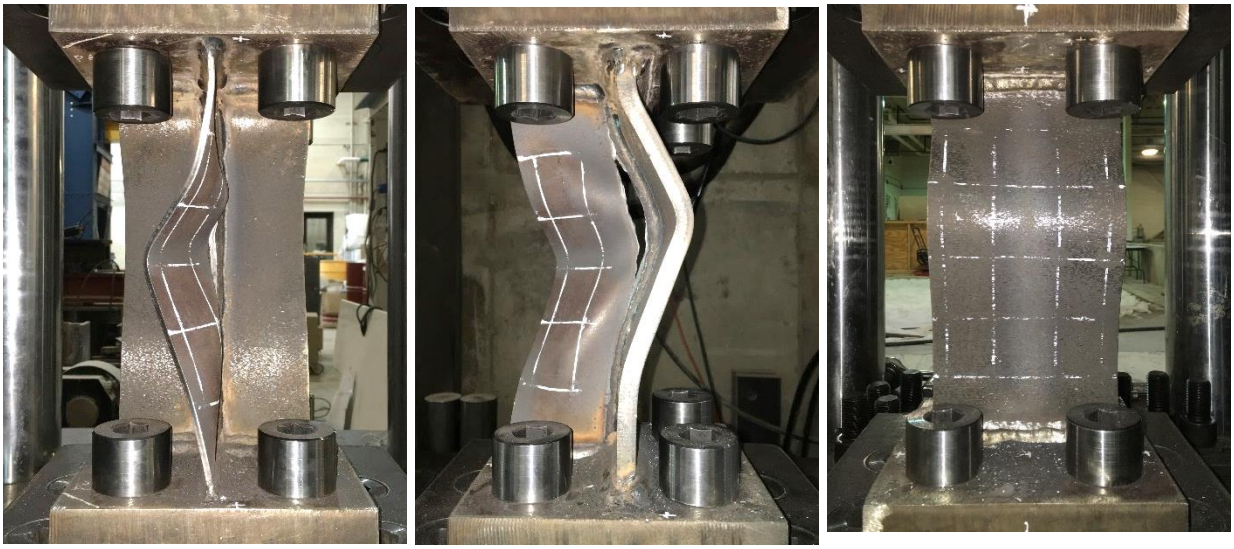

(a)

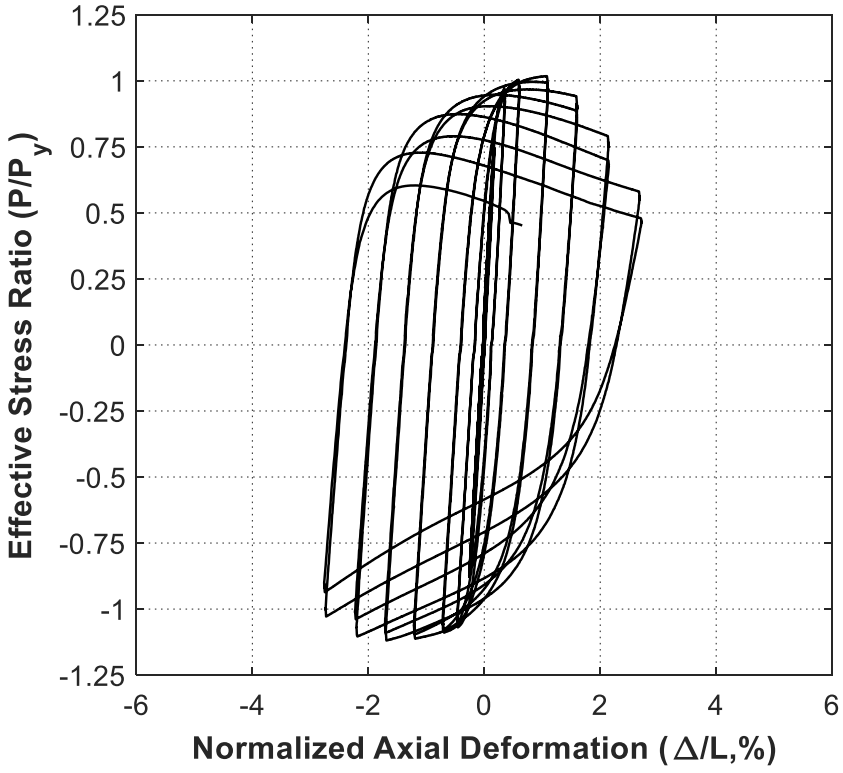

(b)

Figure A-15. Specimen F2W3-CB (a) ductile fracture (b) hysteresis responses

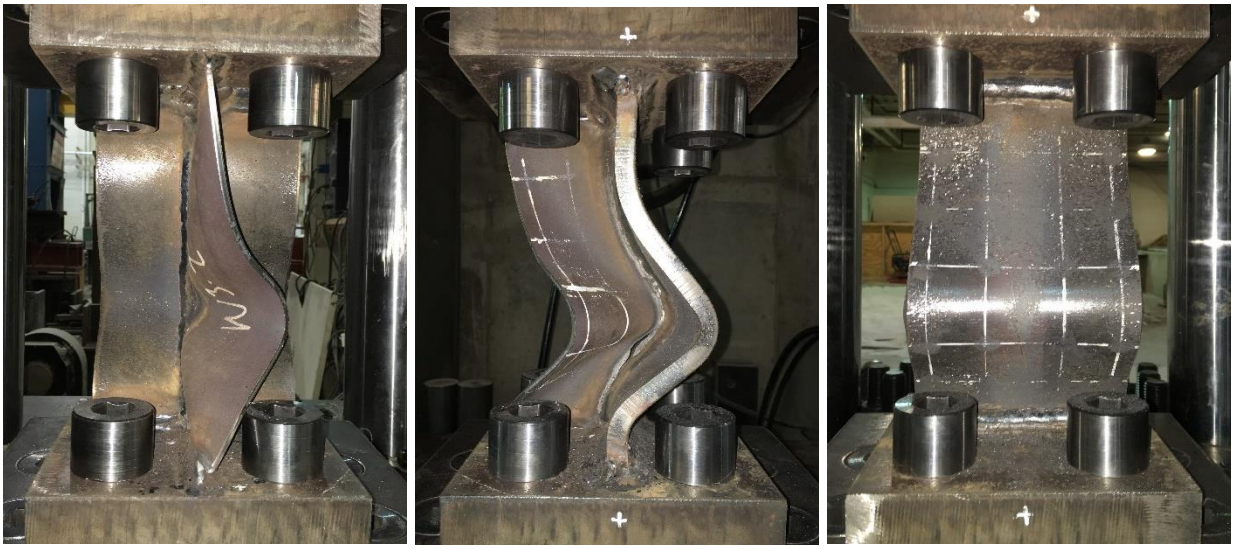

(a)

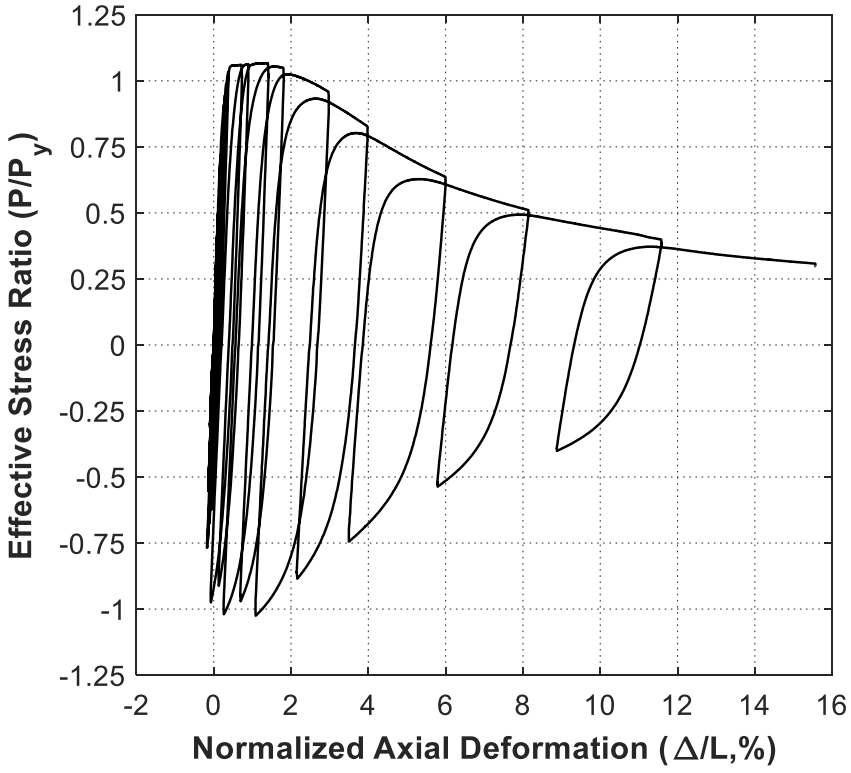

(b)

Figure A-16. Specimen F2W3-CC (a) symmetric local buckling (b) hysteresis responses

(a)

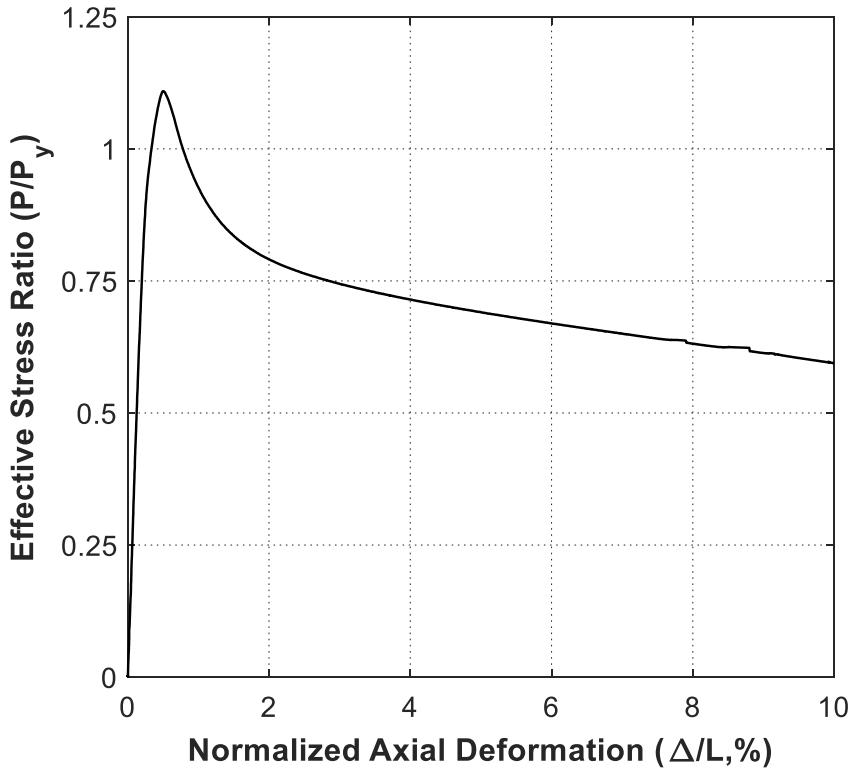

(b)

Figure A-17. Specimen F4W3-M (a) asymmetric local buckling (b) hysteresis responses

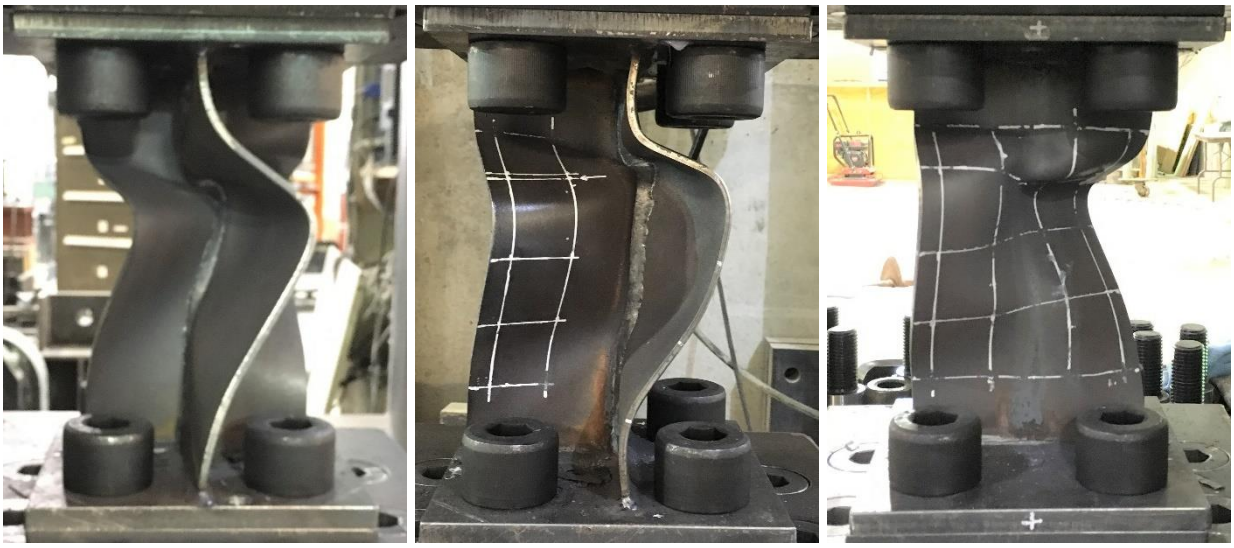

(a)

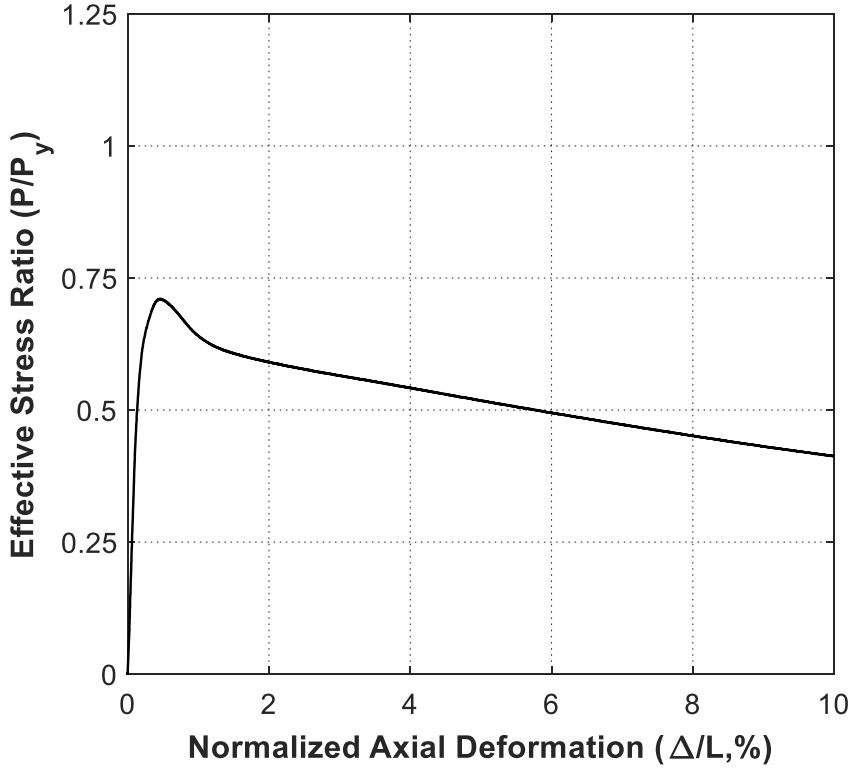

(b)

Figure A-18. Specimen F5W3-M (a) asymmetric local buckling (b) hysteresis responses

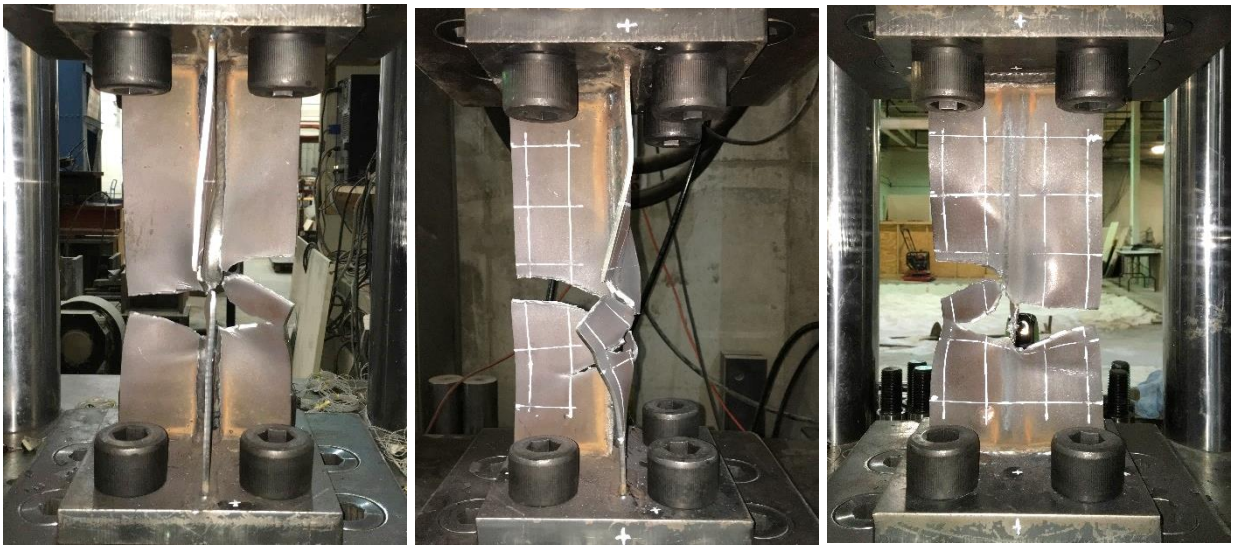

(a)

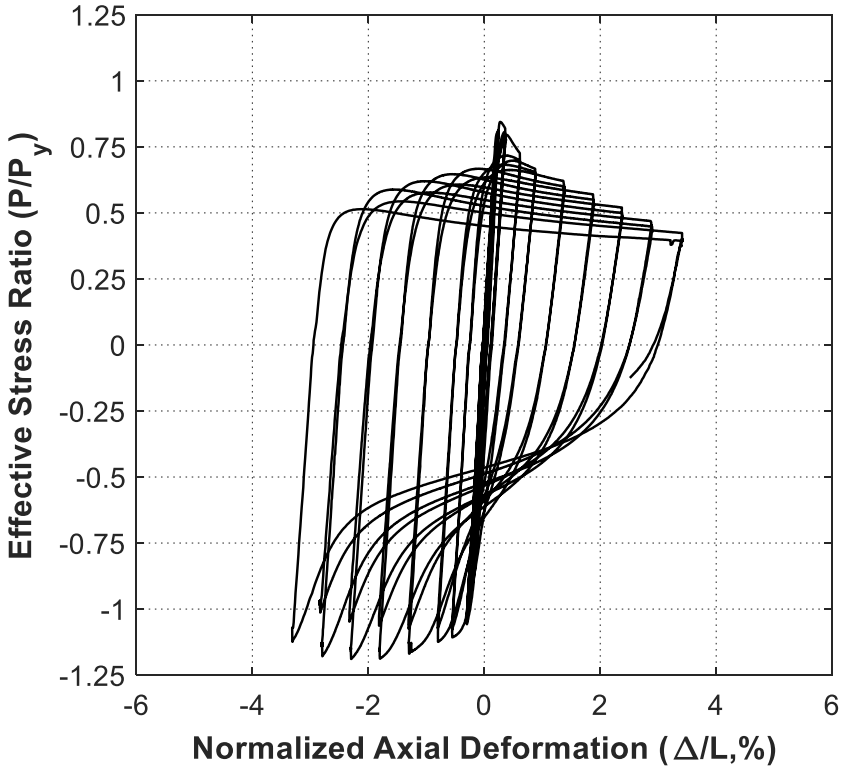

(b)

Figure A-19. Specimen F5W3-CB (a) ductile fracture (b) hysteresis responses

(a)

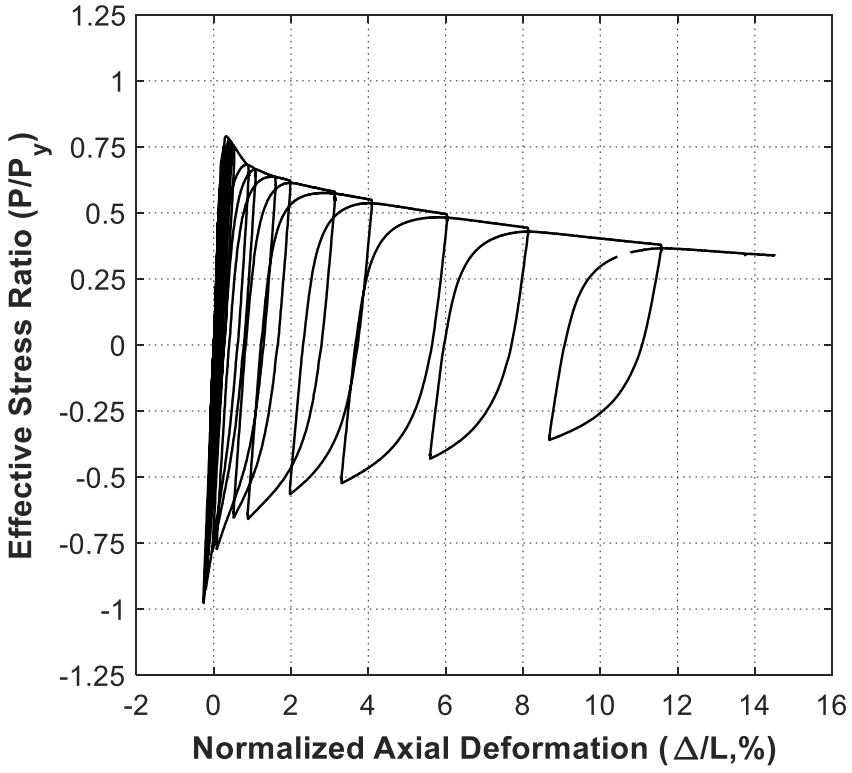

(b)

Figure A-20. Specimen F5W3-CC (a) asymmetric local buckling (b) hysteresis responses

REFERENCES

AISC. (1961). *Specification for the Design, Fabrication, and Erection of Structural Steel for Buildings*, American Institute of Steel Construction, New York, NY

AISC. (1969). *Specification for the Design, Fabrication, and Erection of Structural Steel for Buildings*, American Institute of Steel Construction, New York, NY

AISC. (1989). *Specification for Structural Steel Buildings, Allowable Stress Design and Plastic Design*, American Institute of Steel Construction, Chicago, IL

AISC. (1990). *Seismic Provisions for Structural Steel Buildings*, American Institute of Steel Construction, Chicago, IL

AISC. (1997). *Seismic Provisions for Structural Steel Buildings*, American Institute of Steel Construction, Chicago, IL

AISC. (2002). *Seismic Provisions for Structural Steel Buildings, ANSI/AISC 341-02*, American Institute of Steel Construction, Chicago, IL

AISC. (2005a). *Prequalified Connections for Special and Intermediate Steel Moment Frames for Seismic Applications, ANSI/AISC 358-05*, American Institute for Steel Construction, Chicago, IL

AISC. (2005b). *Seismic Provisions for Structural Steel Buildings*, *ANSI/AISC 341-05*, American Institute of Steel Construction, Chicago, IL

AISC. (2005c). *Specification for Structural Steel Buildings*, *ANSI/AISC 360-05*, American Institute for Steel Construction, Chicago, IL

AISC. (2010). *Seismic Provisions for Structural Steel Buildings, ANSI/AISC 341-10*, American Institute of Steel Construction, Chicago, IL

AISC. (2016a). *Prequalified Connections for Special and Intermediate Steel Moment Frames for Seismic Applications, ANSI/AISC 358-16* American Institute for Steel Construction, Chicago, IL

AISC. (2016b). *Seismic Provisions for Structural Steel Buildings*, *ANSI/AISC 341-16*, American Institute for Steel Construction, Chicago, IL

AISC. (2016c). *Specification for Structural Steel Buildings*, *ANSI/AISC 360-16*, American Institute for Steel Construction, Chicago, IL

Arasaratnam, P., Sivakumaran, K. S., and Tait, M. J. (2011). "True stress-true strain models for structural steel elements." *ISRN Civil Eng.*, 2011, 1–11

Arias, A. (1970). "A measure of earthquake intensity." In: Hansen RJ, editor. *Seismic Design for Nuclear Power Plants*, pp. 438-483. Cambridge, Massachusetts: MIT Press. 23.

ASCE. (1998). *Minimum Design Loads for Buildings and Other Structures. ASCE/SEI 7-98*, American Society of Civil Engineers, Reston, VA.

ASCE. (2005). *Minimum Design Loads for Buildings and Other Structures*. *ASCE/SEI 7-05*, American Society of Civil Engineers, Reston, VA

ASCE. (2006). *Seismic Rehabilitation of Existing Buildings. ASCE/SEI 41-06*, American Society of Civil Engineers, Reston, VA

ASCE. (2010). *Minimum Design Loads for Buildings and Other Structures*. *ASCE/SEI 7-10*, American Society of Civil Engineers, Reston, VA

ASCE. (2016). *Minimum Design Loads for Buildings and Other Structures, ASCE/SEI 7-16*, American Society of Civil Engineers, Reston, VA

Bansal, J.P. (1971). "The Lateral Instability of Continuous Steel Beams." CESRL Dissertation No. 71-1, University of Texas, Austin, TX.

Cheng, X., Chen, Y., & Nethercot, D. A. (2013). "Experimental study on H-shaped steel beam-columns with large width-thickness ratios under cyclic bending about weak-axis." *Engineering Structures*, 49, 264-274.

Chi, B., and Uang, C. (2002). "Cyclic response and design recommendations of reduced beam section moment connections with deep columns." *J. Struct. Eng.,* 10.1061/(ASCE)0733-9445(2002)128:4(464), 464–473.

Coons, R.G. (1999). *Seismic Design and Database of End-Plate and T-Stub Connections*, a thesis submitted in partial fulfillment of the Master of Science in Civil Engineering Degree, University of Washington, Seattle, WA

CSA (Canadian Standards Association). (2014). "Design of steel structures." *CAN/CSA S16-09*, Mississauga, Canada.

Dobry, R., Borcherdt, R. D., Crouse, C. B., Idriss, I. M., Joyner, W. B., Martin, G. R., Power, M.S., Rinne, E. E., and Seed, R. B. (2000). "New site coefficients and site classification system used in recent building seismic code provisions." *Earthquake Spectra*, *16*(1), 41-67.

Eads, L., Miranda, E., Krawinkler, H. and Lignos, D. G. (2013). "An efficient method for estimating the collapse risk of structures in seismic regions." *Earthquake Eng. Struct. Dyn.*, 42, 25–41. doi:10.1002/eqe.2191

Elkady A. and Lignos D. G. (2014). "Modeling of the composite action in fully restrained beam-to-column connections: implications in the seismic design and collapse capacity of steel special moment frames." *Earthquake Eng. Struct. Dyn.*, 43, 1935–1954, doi: 10.1002/eqe.2430

Elkady, A., and Lignos, D.G. (2015a). "Analytical investigation of the cyclic behavior and plastic hinge formation in deep wide-flange steel beam-columns." *Bull Earthquake Eng.*, 13, 1097-1118.

Elkady, A., and Lignos, D. G. (2015b). "Effect of gravity framing on the overstrength and collapse capacity of steel frame buildings with perimeter special moment frames." *Earthquake Eng. Struct. Dyn.*, 44, 1289–1307. doi: 10.1002/eqe.2519.

Elkady, A., and Lignos, D.G. (2017). "Full-Scale Testing of Deep Wide-Flange Steel Columns under Multiaxis Cyclic Loading: Loading Sequence, Boundary Effects, and Lateral Stability Bracing Force Demands." *J. Struct. Eng.*, 10.1061/(ASCE)ST.1943-541X.0001937.

Engelhardt, M. D., and Husain, A. S. (1992). "Cyclic tests on large scale steel moment connections." *Rep. No. PMFSEL 92-2*, Phil M. Ferguson Strnct. Engrg. Lab., University of Texas, Austin, TX.

Engelmann, B. E., Whirley, R. G., and Goudreau, G. L. (1989). "A simple shell element formulation for large-scale elastoplastic analysis." *Analytical and computational models of shells*, Noor AK, Belytschko T, and Simo JC, ASME, New York, NY

FEMA. (2000). "Recommended Seismic Design Criteria for New Steel Moment Frame Buildings." *Report No. FEMA-350*, Federal Emergency Management Agency, Washington, D.C.

FEMA. (2009). "Quantification of building seismic performance factors." *Report No. FEMA-P695*, Federal Emergency Management Agency, Washington, D.C.

FEMA. (2010). "Multi-hazard Loss Estimation Methodology, Earthquake Model, HAZUS-MH MR5, technical manual." Department of Homeland Security, Federal Emergency Management Agency, Mitigation Division. Washington, D.C.

FEMA. (2012). "Seismic Performance Assessment of Buildings." *Report No. FEMA-P-58*, Federal Emergency Management Agency, Washington, D.C.

Fogarty, J., and El-Tawil, S. (2015). "Collapse resistance of steel columns under combined axial and lateral loading." *J. Struct. Eng.*, 10.1061/(ASCE)ST.1943-541X.0001350, 04015091.

Fogarty, J., Wu, T.-Y., and El-Tawil, S. (2017). "Collapse Response and Design of Deep Steel Columns Subjected to Lateral Displacement." *J. Struct. Eng.*, 10.1061/(ASCE)ST.1943-541X.0001848, 04017130.

Hamidia, M., Filiatrault, A. and Aref, A. (2014). "Simplified seismic sidesway collapse analysis of frame buildings." *Earthquake Eng. Struct. Dyn.*, 43: 429–448. doi:10.1002/eqe.2353

Haselton Baker Risk Group. (2019). "Seismic performance prediction program." Accessed date January 31, 2019. https://www.hbrisk.com/.

Huang, Y., and Mahin, S. A. (2010). "Simulating the inelastic seismic behavior of steel braced frames including the effects of low-cycle fatigue." *Rep. No. PEER 2010/104*, Pacific Earthquake Engineering Research Center, Univ. of California at Berkeley, CA

Hutt, C. M., Deierlein, G., Almufti, I., and Willford, M. (2015). "Risk-Based Seismic Performance Assessment of Existing Tall Steel-Framed Buildings In San Francisco." *SECED 2015 Conference: Earthquake Risk and Engineering towards a Resilient World*, Society for Earthquake and Civil Engineering Dynamics, Cambridge, UK

HyperMesh Version 12.0 (2013). Altair Engineering Inc., Troy, MI.

Ibarra, L. F., Krawinkler, H. (2005). "Global collapse of frame structures under seismic excitations." *Technical Rep. 152*, John A. Blume Earthquake Engineering Center, Stanford Univ., Stanford, CA.

ICBO (International Conference of Building Officials). (1961). "Uniform building code." Whittier, CA.

ICBO (International Conference of Building Officials). (1967). "Uniform building code." Whittier, CA.

ICBO (International Conference of Building Officials). (1970). "Uniform building code." Whittier, CA.

ICBO (International Conference of Building Officials). (1973). "Uniform building code." Whittier, CA.

ICBO (International Conference of Building Officials). (1976). "Uniform building code." Whittier, CA.

ICBO (International Conference of Building Officials). (1988). "Uniform building code." Whittier, CA.

ICBO (International Conference of Building Officials). (1991). "Uniform building code." Whittier, CA.

ICBO (International Conference of Building Officials). (1997). "Uniform building code." Whittier, CA.

ICC (International Code Council). (2000). "International building code." Whittier, CA.

Kemp, A.R. (1986). "Factors Affecting the Rotation Capacity of Plastically Designed Members." *The Structural Engineer*, Vol. 64B, No. 2, June.

Kim, J. H. (2015). *Quantitative analysis of factors influencing post-earthquake decisions on concrete buildings in Christchurch*, a thesis submitted in partial fulfillment of the Master of Applied Science in Civil Engineering Degree, University of British Columbia, Vancouver, Canada

Krawinkler, H., Popov, E. P., and Bertero, V. V. (1975). “Shear behavior of steel frame joints.” *J. Struct. Div.*, 101(11), 2317-2336.

Krawinkler, H. (2009). “Loading histories for cyclic tests in support of performance assessment of structural components.” *Proc., 3rd Int. Conf. Adv. Exp. Struct. Eng.*, Pacific Earthquake Engineering Research Center (PEER), Berkeley, CA.

Lay, M.G. (1965). “Some Studies of Flange Local Buckling in Wide-Flange Shapes.” *Journal of the Structural Division*, ASCE, Vol. 91, No. 6, pp. 94–116.

Liu, J., Astaneh-Asl, A. (2000) “Experimental and analytical studies of the cyclic behavior of simple connections in steel frame buildings.” *Report No. UCB/CEE-STEEL-2000/01*, Dept. of Civil and Env. Engrg., Univ. of California, Berkeley, CA

LS-DYNA (2013). Livermore Software Technology Corp., Livermore, CA

MacRae, G. A., Carr, A. J., and Walpole, W. R. (1990). “The seismic response of steel frames.” *Research Rep. No. 90-6*, Dept. of Civil Engineering, Univ. of Canterbury, New Zealand.

Newell, J. D., and Uang, C.-M. (2008). “Cyclic behavior of steel wide-flange columns subjected to large drift.” *J. Struct. Eng.*, 10.1061/(ASCE)0733-9445(2008)134:8(1334), 1334–1342.

NIST. (2010). “Evaluation of the FEMA P695 methodology for quantification of building seismic performance factors.” *NIST GCR 10-917-8*, NEHRP consultants Joint Venture.

NIST. (2011). “Research plan for the study of seismic behavior and design of deep, slender wide flange structural steel beam-column members.” *NIST GCR 11–917-13*, NEHRP consultants Joint Venture.

Ozkula, G., Harris, J., and Uang, C.-M. (2017a). “Classifying Cyclic Buckling Modes of Steel Wide-Flange Columns under Cyclic Loading,” *Structures Congress*, pp. 155–167, ASCE/SEI, Denver, Colorado.

Ozkula, G., Harris, J., and Uang, C.-M. (2017b). “Observations from cyclic tests on deep, wide-beam-column columns.” *AISC Eng. J.*, 54(1), 45–61.

PEER/ATC. (2010). “Modeling and acceptance criteria for seismic design and analysis of tall buildings.” *PEER/ATC-72-1*, Applied Technology Council in cooperation with the Pacific Earthquake Engineering Research Center, Redwood City, CA.

Reyes-Salazar, A., Soto-Lopez, M. E., Gaxiola-Camacho, J. R., Bojorquez, E., and Lopez-Barraza, A. (2014). “Seismic response estimation of steel buildings with deep columns and PMRF”. *Steel and Composite Structures*, 17(4), 471-495.

Richards, P. W., and Uang, C.-M. (2005). “Effect of flange width-thickness ratio on eccentrically braced frames link cyclic rotation capacity.” *J. Struct. Eng.*, 10.1061/(ASCE)0733-9445(2005)131:10(1546), 1546–1552.

Roeder, C. W. (2000). “State of the Art Report on Connection Performance.”, *FEMA Rep. No. 355D*, Federal Emergency Management Agency, Washington, DC.

Sawyer, H.A. (1961). “Post-Elastic Behavior of Wide-Flange Steel Beams.” *Journal of the Structural Division*, ASCE, Vol. 87, No. ST8, pp. 43–71.

SEAOC Seismology Committee (2006). “Preface to the Online Edition,” February 2007, *The SEAOC Blue Book: Seismic Design Recommendations*, Structural Engineers Association of California, Sacramento, CA. Accessible via the World Wide Web at: http://www.seaoc.org/bluebook/index.html

Shen, J.-H. J., Astaneh-Asl, A., and McCallen, D. B. (2002). “Use of deep columns in special steel moment frames.” *Steel Tip Rep. No. 24*, Structural Steel Educational Council, Moraga, CA.

Uang, C. M., and Bruneau, M. (2018). “State-of-the-art review on seismic design of steel structures.” *J. Struct. Eng.*, 10.1061/(ASCE)ST. 1943-541X.0001973.

USGS. (2018). “Unified hazard tool.” Accessed January 31, 2019. https://earthquake.usgs.gov /hazards/interactive/.

Vamvatsikos, D., and Cornell, C.A. (2002). “Incremental dynamic analysis.” *Earthquake Eng. Struct. Dyn.*, 31(3), 491–514.

Wu, T.-Y, El-Tawil, S., and McCormick, J. (2017). “Behavior of steel moment frames with deep column sections under seismic loading.” *Proc., 16th. World Conference on Earthquake Engineering*, International Association of Earthquake Engineering, Tokyo.

Wu, T.-Y, El-Tawil, S., and McCormick, J. (2018a). “Highly ductile limits for deep steel columns.” *J. Struct. Eng.*, 10.1061/(ASCE)ST.1943-541X.0002002.

Wu, T.-Y, El-Tawil, S., and McCormick, J. (2018b). “Seismic Collapse Response of Steel Moment Frames with Deep Columns.” *J. Struct. Eng.*, 10.1061/(ASCE)ST.1943-541X.0002150.

Xiaoming, C., Jin, D., and Yungui, L. (2015). “Mass proportional damping in nonlinear time-history analysis.” *Proc., 3rd international conference on material, mechanical and manufacturing engineering, IC3ME2015*, Atlantis Press.

Youssef, N., Bonowitz, D., and Gross, J. (1995). ‘‘A survey of steel moment resisting frame buildings affected by the 1994 Northridge Earthquake.’’ *Rep. No. NISTIR 5625*, National Institute of Standards and Technology, Gaithersburg, MD.

Zareian, F., Krawinkler, H., Ibarra, L. and Lignos, D. (2010). “Basic concepts and performance measures in prediction of collapse of buildings under earthquake ground motions.” Struct. Design Tall Spec. Build., 19: 167–181. doi:10.1002/tal.546

Zhang, X., and Ricles, J.M. (2006). “Experimental Evaluation of Reduced Beam Section Connections to Deep Columns.” *J. Struct. Eng.*, 10.1061/(ASCE)0733-9445(2006)132:3(346).